Development of Dielectric Elastomer Actuators for MRI Devices

by

John D. Vogan

BS Mechanical Engineering
Case Western Reserve University, 2002

Submitted to the Department of Mechanical Engineering
in Partial Fulfillment of the Requirements for the Degree of
Master of Science in Mechanical Engineering

at the

Massachusetts Institute of Technology

June 2004

Signature of Author . . . .
Department of Mechanical Engineering
May 7, 2004

Certified by . . . .
Steven Dubowsky
Professor of Mechanical Engineering
Thesis Supervisor

Accepted by . . . .
Ain A. Sonin
Chairman, Department Committee on Graduate Students

Development of Dielectric Elastomer Actuators for MRI Applications

by
John D. Vogan

Submitted to the Department of Mechanical Engineering
on May 7, 2004 in Partial Fulfillment of the
Requirements for the Degree of
Master of Science in Mechanical Engineering

ABSTRACT

Dielectric elastomer (DE) actuators are an emerging class of polymer actuation devices. They exhibit large strains and have high force and energy densities. They can be designed in a variety of geometries and are inexpensive to manufacture. Currently, the use of DE Actuation is limited because quantitative design information is incomplete and the complex phenomena governing their performance have not been fully characterized. In this study, several such issues are investigated both experimentally and analytically.

The actuators designed for this research function as binary actuators, that is, they operate between two set states, OFF and ON. Performance of the actuators is predicted based on theoretical analysis and the results are compared to experimental results. Improvement of fabrication methods and determination of optimum design parameters have been experimentally determined.

Since DE actuators can be constructed out of polymers and without any ferromagnetic materials, they can potentially be used in a Magnetic Resonance Imaging (MRI) machine, which has strict compatibility requirements that limit the use of certain materials. MRI is a powerful and effective medical diagnostic tool, but treatment is limited because of the confined space and compatibility issues. It has been well recognized that its value would be increased if it were possible to physically manipulate objects within the MRI machine during imaging, but conventional manipulation systems cannot operate within an MRI due to the incompatibility of ferromagnetic materials.

Binary DE actuators eliminate the need for conventional electromagnetic actuators and their associated controlling electronics. This inherent compatibility suggests that a new class of MRI treatment devices is possible. Potential applications for use in the MRI environment are introduced, and prototypes for illustrating these applications are fabricated. One such application, a reconfigurable RF coil for flexible imaging capabilities, proves that not only are DE actuators and MRI compatible, but that they can significantly enhance imaging capabilities.

Thesis Supervisor: Steven Dubowsky
Title: Professor of Mechanical Engineering

Acknowledgements

This research was performed at the Field and Space Robotics Laboratory (FSRL) at MIT under the sponsorship of the Center for Integration of Medicine and Innovative Technology (CIMIT) and Cambridge MIT Institute (CMI).

I would like to thank my advisor Professor Steven Dubowsky for his guidance and the opportunity to work at the FSRL. Thanks to Vivek Sujan, Karl Iagnemma, and Sauro Liberatore for their valuable supervision and advice. Thanks to all members of the FSRL, especially Jean-Sebastien Plante for his valuable help in developing many of the ideas and devices presented in this work. His experience and involvement was invaluable. Thanks to Dan Kacher at Brigham and Women's Hospital for his collaboration with the MRI experiments and applications.

I would also like to thank my family and especially my wife, Brianne, for their support over the past two years.

Table of Contents

Figures and Tables

1 Introduction

This thesis reports on the development of dielectric elastomer (DE) actuators for use as an actuation technology within Magnetic Resonance Imaging (MRI) environments. Dielectric elastomers are a type of electroactive polymer that has shown significant potential as an emerging actuation technology. Extensive research on polymer materials for actuation has been done during the past ten years. These materials offer many advantages, such as large strain capabilities, high energy densities, and fast responses. If successfully implemented, these materials could be used to produce inexpensive and lightweight actuators for a variety of commercial and scientific applications. However, polymer based actuation technologies are not often used in practice due to a lack of fundamental design knowledge and sound fabrication methods. For this study, important progress has been made in developing practical and efficient linear DE actuators.

Electroactive polymers (EAP) exhibit muscle like behavior by changing their geometry when an electric signal is applied. Because of their simple operating requirements and material composition, they show promise for the development of alternative actuator concepts for applications where severe environments place restrictions on what type of devices can be used. One such environment is found within an MRI machine, and there are strict limitations on what type of materials and devices can be placed within them.

This research focuses on developing polymer based actuators for powering useful devices, specifically for potential MRI based applications. The fundamental operating principles and performance behavior of this technology are presented in detail. The design and methods for developing a specific actuator for use in many applications is also presented. Several prototype devices illustrating potential applications are also presented.

1.1 Motivation

Magnetic Resonance Imaging has become an indispensable diagnostic tool in the medical community. It has the ability to safely image any plane within the body, whereas other imaging technologies are more limited. For example, CT scans are limited to the axial plane, whereas an MRI system can create images in any plane without the patient moving [1]. MRI technology allows doctors and technicians to choose exactly where and what orientation in the body to acquire an image. It is ideal for diagnosing many medical problems [1,2], such as:

- Bone tumors or abnormalities
- Multiple sclerosis (MS)
- Tumors or infections in the brain, spine or joints
- Ligament and tendon damage
- Masses in the soft tissues of the body

In recent years, the medical community has been taking steps to incorporate MRI into treatment procedures as well as diagnostics. It has been well recognized that its value would be greatly increased if it were possible to physically manipulate objects within the MRI machine during imaging, and there are many motivations for MRI compatible surgical robots and manipulators [3,4,5,6]. Examples would be performing endoscopic surgical procedures or biopsy needle insertion while observing the procedure inside the patient in real time using MRI. Due to their high precision, robots could potentially be used for such manipulation tasks. However, because of the extremely strong magnetic fields (more than 1 Tesla) used for MRI, conventional robotic components such as electromagnetic actuators and sensors are unusable.

Due to its all-plastic construction, it is shown here that a DE powered robot can be placed very close to the region of interest and perform high precision tasks without distorting the images. DE's have numerous advantages that make them ideal for actuation within an MRI environment. These include:

- Zero degradation of the MRI image
- Inexpenisve (potentially disposable)
- Large strain (more than 100%)
- Constructed mostly of polymer – lightweight

The purpose of this thesis is to lay the groundwork for developing practically useful DE powered devices for enhancing MRI treatment. Such development does not fall within the domain of traditional robot or machine design. DE actuators are not commercially available, and currently there are no detailed design data or guidelines for designing or building them. This work is meant to address the need for both qualitative and quantitative design guidelines to bring such actuators to practical use.

1.2 Background and Literature

1.2.1 Dielectric Elastomer Actuation and alternative Technologies

Dielectric elastomers are a class of electroactive polymers used for actuation devices. Previously, these devices have been referred to as Electrostrictive Polymer Artificial Muscles (EPAM). In this terminology, "electrostrictive polymer" refers to any material that exhibits a mechanical response to electric stimulation. However, there is a separate class of material called electrostrictive polymers [7]. In these materials, the deformation is dependent on the polarization at the molecular level, which generates a compressive force in the direction of polarization.

Polarization is not necessary for the mechanical response of DE actuators. DE actuators are simply dielectric materials placed between two compliant electrodes. The operating principle is simple and shown in Figure 1. A soft polymer film is coated on both sides with compliant electrodes. As a voltage is applied to the electrodes, electrostatic (Maxwell) stresses cause the soft polymer to compress in thickness and expand in area. The resulting mechanical motion is a means for actuation.

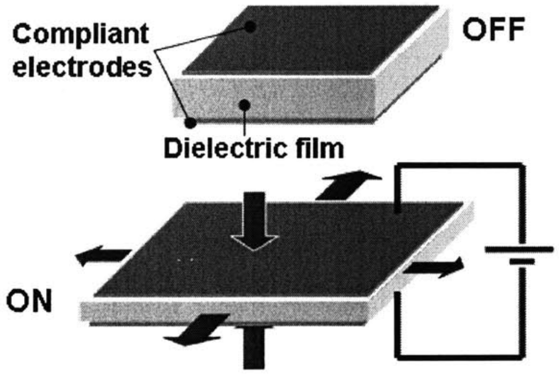

Figure 1: Operating principle of dielectric elastomer [55].

Preliminary development of DE actuators was underway in the early 1990's [8,9]. Since that time, fundamental characteristics and potential applications of this technology have been studied [10,11,12,13]. Currently there are several institutions performing research in several aspects of DE actuation [14,15,16]. The development of DE actuators in the Field and Space Robotics Laboratory (FSRL) at MIT began in 2000 during research in the field of binary robotics, which is a design and control paradigm that proposes the use of numerous binary actuators embedded within a mechanical structure [17,18]. It was found in this research that DE show potential as actuators for binary robotics [19,20].

Dielectric elastomers have interesting characteristics that make them potentially superior to other actuator technologies for a variety of applications. Examples of other actuation technologies, as well as their major performance properties, are listed in Table 1 [21]. These include other "smart material" technologies, such as shape memory alloy, piezoelectric materials, and other types of electroactive polymers.

Table 1: Smart Material Actuator Comparison [21]

Actuator Type	**Maximum Strain (%)**	**Maximum Pressure (Mpa)**	**Specific Energy (J/g)**	**Maximum Efficiency (%)**	**Speed for one cycle**
Dielectric Elastomer Actuator	200	7	3.4	80	Medium-Fast
Electromagnets	50	0.1	0.003	90	Fast
Piezoelectric Ceramic	0	110	0.013	90	Fast
Shape Memory Alloy (TiNi)	0.2	200	15	10	Slow
Conducting Polymer	10	450	23	1	Slow
Conducting Gel	40	0.3	0.06	30	Slow

Shape memory alloys are metals that exhibit a property called martensitic transformation, which is a solid state phase transformation that allows the material to change shape in response to temperature changes [22]. SMA's achieve pressures up to 200 MPa and material strains of over 5%. However, due to power dissipation through heating, maximum efficiency is less than 10%.

Piezoelectric actuators are ceramic based materials that change their shape in response to an electric field. They have fast response rates and achieve pressures over 100MPa, but they also display relatively small strains, generally less than 1% [23]. Compliant mechanisms have been designed to amplify their motion[24].

Other electroactive polymers (EAPs) have been explored for use as smart material technologies. Conducting polymers display large dimensional changes due to electrochemical doping of the polymer that occurs in response to an applied voltage [25]. They typically can achieve strains up to 10% and pressures up to 450 MPa [21], but the polymer has to be immersed in a liquid based electrolyte[25]. This limits practical implementation. Another example of EAP is Polymer gel, which also swells as a result of an applied voltage [7]. The actuation pressures generated here are generally insufficient for practical applications.

DE actuators have relatively strong performance numbers in each of the categories listed in Table 1. Consequently, research in DE actuators has increased in the past several years, and several experimental concepts have been studied. DE have been proposed for use in linear actuators, loudspeakers, solid state optical devices, and generators [26,23]. A variety of geometric embodiments have been proposed. Planar and cylindrical geometries have been proposed to power a snake-like manipulator and an insect-inspired hexapedal walker [27,23]. Cone shaped and diaphragm actuators, in which the motion is normal to the film plane, have been developed[12,28]. Such a device has been proposed to power an inchworm robot with small displacements [12]. Concepts have been proposed for incorporating DE actuators in shape control of large space mirrors [29]. Haptic applications using DE actuators have also been proposed [30].

The use of DE actuators in feedback control systems, an alternative approach to the system concepts studied for this work, has also been studied. Position feedback provided by a laser displacement sensor has been used to control a dielectric elastomer actuator [13]. A multidirectional prototype has been designed for continuous positional control with multiple actuators [31]. Methods of controlling the actuator without sensors have also been investigated [32].

Despite the scope of the overall research in this area and the depth in which it has been pursued in various specific situations, most of the published research on dielectric elastomers over the last several years has been exploratory. Therefore, very few design models are available.

1.2.2 Actuation within MRI Machines

MRI compatibility is a well know problem among those who have attempted to develop devices for enhancing MRI capabilities. The safety and compatibility of potential devices and materials have been has been thoroughly characterized [33,34]. A general primer describing the potential interactions of mechatronic devices and MRI machines has been published by the Food and Drug Administration [35]. The *MR compatibility* of a device is defined as: [36]:

- It is MRI safe (does not add risk to human or equipment)
- Its use in MRI environment does not affect imaging
- It operates as designed in the MRI environment.

Many objects may operate safely within the environment but can affect imaging, or other objects might not affect imaging but may not operate as intended due to influences of the large and changing magnetic fields. While the complete compatibility guidelines are quite complex and depend on the location of the device and the location being imaged, it can generally be assumed that non-ferrous materials and devices that do not create electromagnetic disturbances are compatible.

Ferromagnetic materials are dangerous when placed in close proximity to an MRI machine because of the high magnetic fields. Electronically driven motors and sensors can cause electromagnetic interference, thus disturbing the image. Typically, controlling electronics are placed outside of the MRI room.

The incompatibility of conventional actuator systems have led to development of MR devices that implement alternative actuation technologies. For example, an MR Compatible Surgical Assist Robot that uses ultrasonic motors has been developed [37]. Masamune has developed an ultrasonic motor based manipulator for needle insertion [38]. An MR guided, ultrasonic actuated focused ultrasound surgery system was developed by Hynynen [39]. Previous versions of this system used hydraulic actuators.

While piezoelectric and pneumatic (as well as hydraulic) actuators are both compatible actuation technologies, they both have drawbacks. For example, piezoelectric motors and their accompanying transmission are very complicated and expensive to produce, and generally must be kept isolated from the imaged region. Pneumatic and hydraulic actuators require pressure supplies that may not be conducive to the limited workspace available in and around an MRI machine.

1.3 Research Overview

The first objective of this research is to develop actuators that take advantage of the high strain and energy capabilities of DE technology. The design and performance of dielectric elastomer actuators is studied from both an experimental and theoretical point of view. The second objective of the research is to show the potential of DEA to increase the usefulness of MRI treatment.

Chapter 2 describes several fundamental characteristics of dielectric elastomer actuators that have been studied as part of this research. The governing principles and considerations are briefly discussed. Several important issues, such as breakdown modes, are explored.

Chapter 3 discusses the design and fabrication of DE actuator modules with desired force and displacement characteristics. Previous implementations of DE show performance that is less than what can be achieved under ideal conditions [40]. In this work, the geometries and construction of the actuator has been optimized to allow for increased energy output and stroke. The result is a single actuator that can be modified and implemented in a variety of applications

Chapter 4 describes the development of simple devices that illustrate the usefulness of DE devices, particularly for MRI treatment. The first such device is a reconfigurable surface coil for MRI imaging which illustrates DE actuation of a practical MRI device. Experimental data proves compatibility of DE actuators with MRI environments under strict requirements. The results show the potential of DE actuation to enhance imaging capabilities of MRI.

Two simple manipulation devices that are MRI compatible are also described. One is a simple translating device which may potentially be developed for use in various non-invasive surgical procedures. The other concept is a spatial manipulator based on the concept of binary robotics. This device exploits improved actuator performance to further illustrate the capabilities of DE powered manipulation systems. Devices designed using this concept could be used for non-invasive, MRI guided surgical procedures, such as biopsy needle placement and insertion.

2 Fundamental properties of Dielectric Elastomers

In this chapter, several fundamental issues governing the behavior of dielectric elastomers will be discussed. These issues will be investigated in the context of actuator design and performance. Several key issues, such as elastomer selection and failure modes, will be discussed.

2.1 Operating Principle

The fundamental mechanism governing the motion of DE actuators consists of two stresses, a shear stress and a compressive stress, that are applied to an elastomeric film when the compliant electrodes are charged, as shown in Figure 1 [41,42]. The unlike charges on the opposing electrodes attract each other and generate a compressive stress in the z-direction on the film. The repulsion of like charges on the same electrodes generates shear stress in the planar (*x* and *y*) directions of the film. The principle is illustrated in Figure 2.

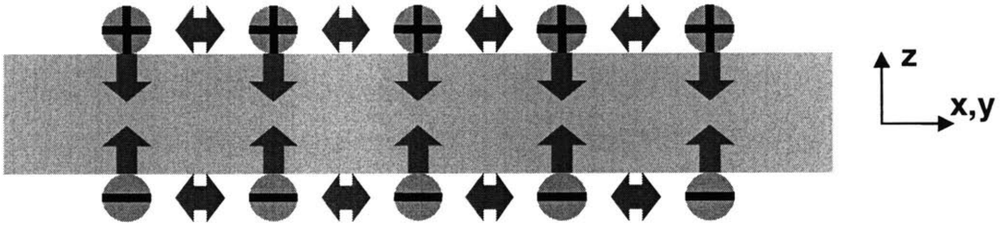

Figure 2: Maxwell pressures acting on elastomer.

The contributions by the compressive and shear stresses can be lumped into a single effective pressure, *P*, which is given by:

$$P = \varepsilon\varepsilon_0\left(\frac{V}{t}\right)^2 = \varepsilon\varepsilon_0 E^2 \tag{1}$$

Where ε is the dielectric constant, ε_0 is the permittivity of free space ($\varepsilon_0 = 8.85x10^{-12}$ *F/m*), and *E* is the applied electric field, which is the ratio of the applied voltage, V, to the film thickness, *z*. This effective pressure is derived using an electrostatic model of the work done by the electric field as the system is allowed to deform [42]. For this model, it is assumed that the charge densities on the electrodes and the electric field are uniform.

The stresses cause the film, which is ideally a very soft polymer, to decrease in thickness. The film laterally expands in area due to the constant volume property of polymers. The strain values that result can exceed 200%. The dielectric film must be under some initial planar tension in the OFF state to prevent buckling in the ON state. When compressive stress is applied to a film already in planar tension, there will be an effective reduction in the tension of the film. This change in tension provides the force necessary to achieve movement. The external tension can be applied by constraining the film to rigid or flexible structures.

2.2 Actuator Components

A DE actuator can be fabricated in a variety of geometries. In general, a very high electric field, E, is required to generate significant pressures across the polymer. To develop such high electric fields, the thickness of the polymer should be quite small. Therefore, the polymer is generally in the form of a thin film.

Several types of film have been investigated to determine if they are suitable for actuators. There are several factors to consider when choosing a polymer for DE and the fundamental expression shown in equation (1) reveals the important ones. The pressure that can be generated is directly proportional to dielectric constant and the square of electric field, so ideally the material will have a high dielectric breakdown value. Furthermore, since the amount of deflection is inversely proportional to the stiffness of the material, it is desirable that the material have a low stiffness. For high speed applications, a material should have low viscosity.

The two major elastomers investigated for this research were acrylic and silicone films. VHB 4905/4910 acrylic is a commercially available structural adhesive (3M® Adhesives, Saint Paul, Minnesota). It is supplied as an adhesive tape, conveniently in a relatively thin film (0.5 or 1.0 mm thick). Several silicone films, including HSIII and RTV (Dow Corning®), were also investigated. The silicone films were fabricated by hand and were therefore subject to several factors, such as catalyst fraction, mixing, degassing, and casting techniques, that could drastically affect material properties.

Several different materials can be used for compliant electrodes. The most commonly used are: silver grease, carbon grease, carbon black, and carbon based elastomers. Silver and carbon greases are composed of conducting silver or carbon particles suspended in a viscous oil. A carbon grease produced by MG Chemicals™ is used for actuators developed for this study. This grease has a resistivity of approximately 1000 Ohm-cm.

An elastomer based conductor, composed of carbon particles suspended in a silicone rubber then sprayed onto a surface before it cures, has been developed [43]. Such a method, which yields a thin conductive elastomer film with minimal stiffness, improves the aesthetic and tactile properties of the actuator because the grease cannot smear into undesired locations. However, for illustrative and disposable prototypes, grease is sufficient.

DE actuators require a structure for maintaining tension in the film so that it will not buckle under an added compressive stress. There are three major classes: fixed frame, flexible frame, and cylindrical. Fixed frames provides rigid geometric constraints to the film boundary in all directions which. The region of the film that is coated with electrodes experiences deformation, as shown Figure 3(a). Flexible frames constrain the film in all directions but can change shape based on the tension in the film. Such frames deform when the film is actuated, as shown in Figure 3(b). Cylindrical actuators use a film that is wrapped in a cylinder shape, so that the diameter and length of the cylinder change under actuation, as shown in Figure 3(c).

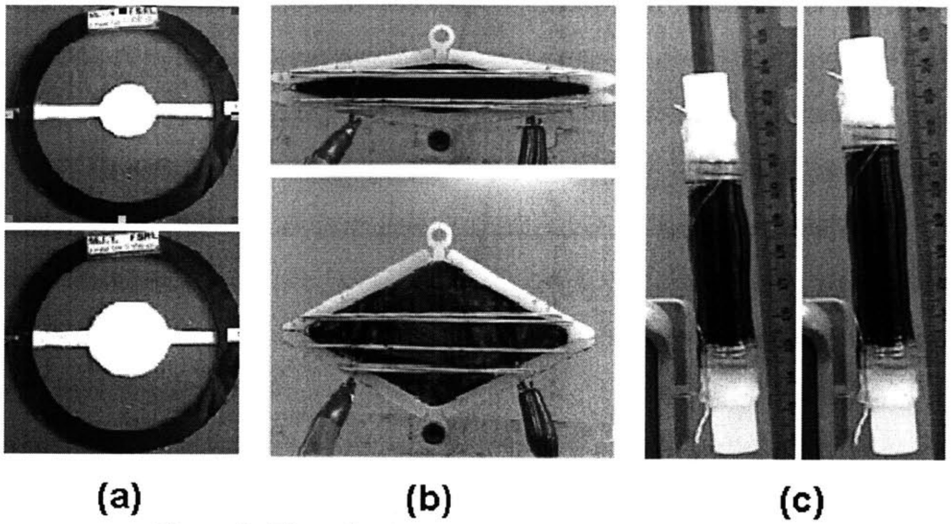

Figure 3: Three basic arrangements for DE actuators.

To characterize the basic performance of an actuator, the interaction of its various components can be represented with the simplified model shown in Figure 4. The elastomeric film and electrodes collectively behave like a tension spring with variable stiffness. When actuated, the electrostatic pressure across the film causes the stiffness profile of the film to shift downwards. The pre-load element provides a force in the opposite direction of the film and maintains tension in the film.

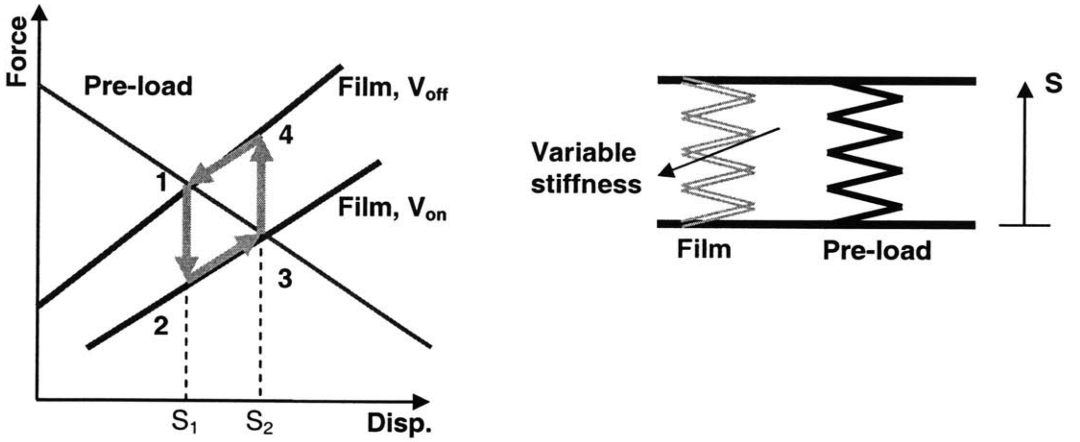

Figure 4: Lumped sum model of actuator system. The pre-load curve is actually a negative force (it is compressive, whereas the film is tension), but is shown as positive to better illustrate the intersection points of the curves.

When the force-displacement curves intersect and the opposing forces are equal but opposite, the sum of the forces within the system is zero and the system is in equilibrium. Therefore, S_1 indicates the position when the actuation is OFF (film spring is stiff). Upon actuation, the curve shifts downwards, and the forces are no longer at equilibrium at position S_1. The force difference causes the output of the system to move toward equilibrium. At S_2, the force curves intersect and the system is again in equilibrium, representing the position when the actuator is ON. If the actuator is then turned off, the curve shifts upwards, and the resulting force difference (in the opposite direction) occurs drives the system back to its initial position (S_1). The area enclosed by the arrows represents the energy obtained from the system. Typically, to optimize the performance of a single actuator, the difference between the two equilibrium points should be maximized, thus maximizing the stroke and energy output of the actuator.

The design of the actuator is carried out using the lumped-sum model. The model shows what forces and displacements should be available from an actuator based on the properties of its individual components. For the purposes of this study, the displacement of the actuator (strain of the film) was considered the most important performance characteristic. The force available from an actuator is directly proportional to the amount of active polymer layers. Therefore, if a single actuator with a planar geometry and large displacement is stacked in parallel with several other similar actuators, the force will be multiplied by the number of actuators but the strain will not be affected.

2.3 Elastomer Characterization and Selection

Several promising materials have been identified for DE [21]. VHB 4905 is one of the best known materials for DE because it has a very high dielectric strength (up to 250 MV/m), moderately high dielectric constant (4.5), and a relatively low modulus (100-300 kPa). The material is relatively inexpensive and requires no extensive processing.

Other materials have demonstrated performance that exceeds that of the VHB in certain categories. For example, silicone based materials have shown properties appropriate for high frequency applications. Loudspeakers operating at frequencies up to 20 kHz have been developed using silicone films [23]. The speed of response of VHB based actuators is limited by its viscoelastic properties.

The development and identification of a material with optimum properties is a difficult problem. First, there are no explicit definitions of a polymer's mechanical and dielectric properties based on its molecular structure. Second, there are fundamental trade-offs preventing optimization of all material properties. For example, the bulk resistivity of a polymer decreases exponentially with increasing values of permittivity [44]. Ideal dielectric films will have very high resistances and dielectric strengths, but these values are likely to decrease with increasing dielectric constant. This characteristic will fundamentally oppose optimization of all material properties.

The key dielectric properties for several candidate DE materials have been measured[21]. A map of the dielectric properties of these materials is shown in Figure 5.

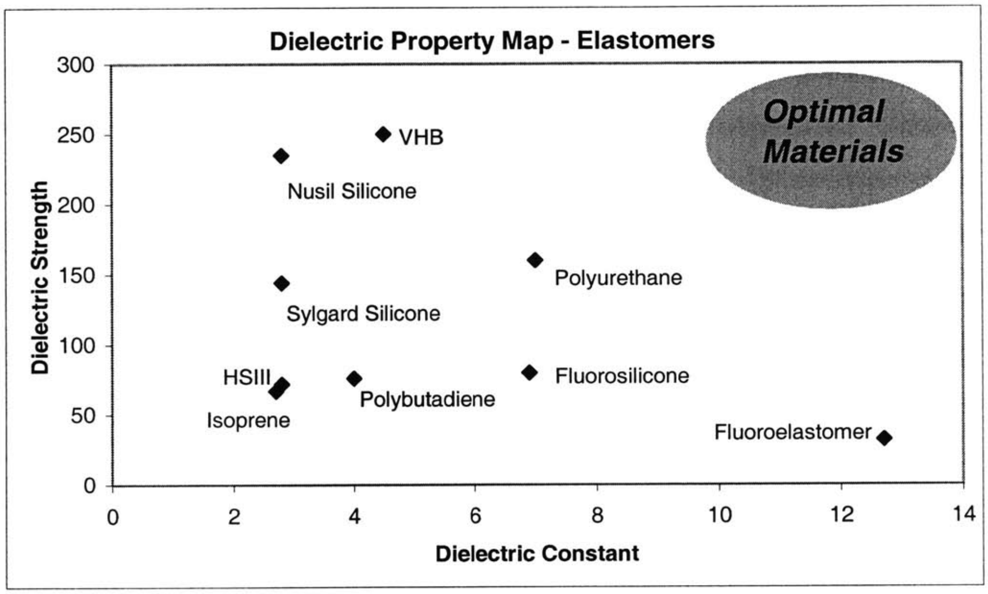

Figure 5: Dielectric properties of candidate DE materials (values obtained from [21]).

The best materials from a dielectric point of view are those with high dielectric constants and strengths. Since the maximum pressure that can be generated is proportional to the square of the dielectric strength, then this value is of particular importance.

Based on the properties described above, equation (1) can be used to estimate the potential that each material has for implementation as a DE actuator. Assuming the material has constant dielectric properties, the maximum Maxwell pressure can be calculated for each material, as shown in Figure 6. It should be noted that the dielectric properties of a material can vary significantly with environmental and loading conditions [45], so the numbers presented here are only estimates.

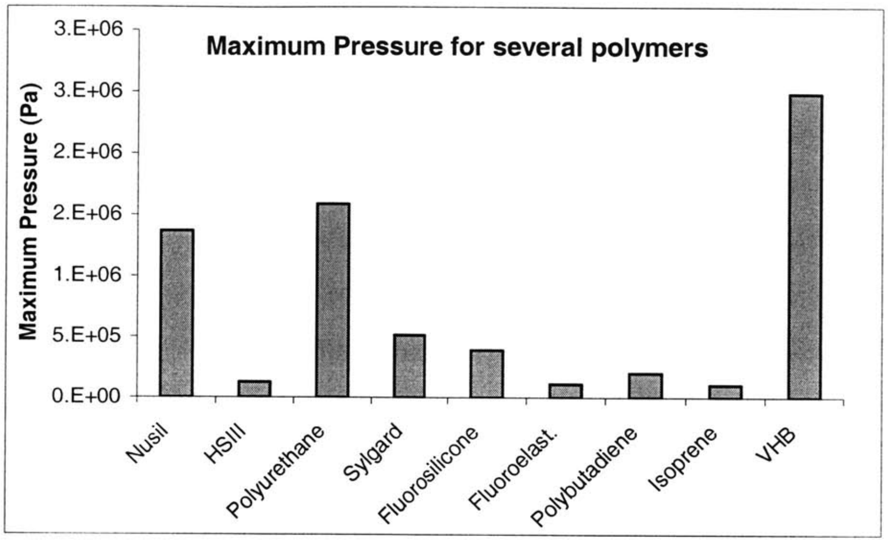

Figure 6: Maximum pressure for potential dielectric materials.

Another important property that can be evaluated is the polymer's capacity for deformation. High pressures are not interesting if the material is very rigid. The ability of a material to deform is proportional to the maximum pressure that can be generated through it and inversely proportional to its stiffness. Despite the non-linearity of elastomers, the modulus for each of these materials has been approximated [21]. Using these values and the maximum pressures calculated above, estimates for the strain capacity of the each material was calculated. The results are shown in Figure 7.

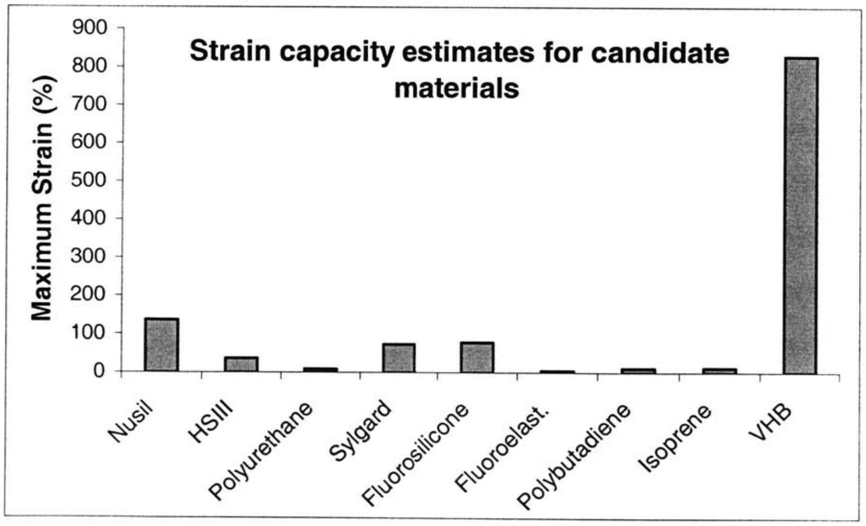

Figure 7: Maximum potential strain for candidate elastomers

These values are considered a strain capacity rather than actual achievable strain values. Strains cannot reach values such as 800% (as shown in the graph) because of non-linearities in the stiffness and breakdown modes that are not captured with these simple calculations. However, this value is an important metric for combining several key parameters of a polymer into one important indicator of its potential as a DE actuator. Consequently, this figure illustrates why VHB is the primary material used for DE actuation throughout both the scientific community and in this study.

VHB also has significant drawbacks, such as high visco-eleastic losses and stress relaxation properties that are difficult to quantify. If the most important performance characteristic was high speed or efficiency, then other materials might be used. However, for the concepts and devices developed in this research, high displacement actuators were desired, so VHB was the main material used.

2.4 Film Failure

The limits to actuator performance are determined by failures. In general, the failure of DE actuators is attributed to dielectric failure (when the electric field defined by the potential difference of the electrodes and the thickness of the film becomes too large). However, there are several factors that affect how and when this limit will be reached. This section discusses several issues that should be considered when analyzing film failure.

2.4.1 Failure modes

The performance of DE actuators cannot simply be predicted by knowing the mechanical strength of a polymer and its dielectric properties. The film can fail in several ways and due to different factors. These modes can be classified into three major categories [48], as shown in Figure 8.

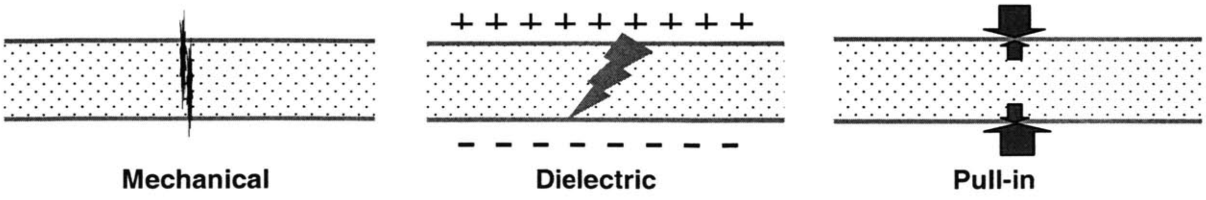

Figure 8: Various failure modes [48].

Mechanical failure simply refers to material failure that occurs when the ultimate strength of the material is exceeded.

Dielectric failure occurs when the electric field in a material becomes greater than its dielectric strength and the insulative property of the material suddenly breaks down [44]. The phenomenon manifests itself as a spark through the material. After dielectric failure, there is a permanent "defect" in the material and it can no longer be used as an actuator.

Pull-in failure occurs for conditions the electrostatic pressure is always greater than the compressive elastic stresses in the elastomer. When the elastomer is subjected to an electrostatic pressure, it decreases in thickness. As it decreases in thickness, the electric field increases if the voltage difference is kept constant. As a result, the electrostatic pressure actually increases as the material is compressed. If the material is not stiff enough to equalize this pressure, then there is unrestricted compression of the material which leads to either a dielectric or a mechanical failure. This phenomenon, also referred to as electromechanical failure, was identified as a means of dielectric failure in insulators in 1950 [46]. A one dimensional model of a linear material subjected to a pressure field defined by equation (1) shows that regardless of the material stiffness, failure occurs at an engineering strain of 33% in thickness [11]. However, these predictions do not match experimental data, which indicate that thickness strains up to 70% are possible [47,48]. This discrepancy suggests that pull-in is a much more complex failure mechanism than originally predicted. The pull-in limit is affected by non-linear elastic behavior, significant viscoelasticity, large material deformations, and a varying dielectric strength [49].

2.4.2 Dielectric Strength Measurements

Dielectric breakdown is a complex phenomenon that can be caused by many different means. Currently, there is no analytical method for determining the dielectric strength of a material from its structural composition or other electric properties [44].

Not only are theoretical predictions of dielectric strength difficult to formulate, experimental measurements of dielectric strength rarely yield the same results as those in practical situations [44,45,46]. Environmental issues such as humidity and temperature are just a few examples of factors that can alter dielectric strength [44,45]. Also, small variations in film and electrode shape have a significant effect on dielectric strength.

Another major factor affecting dielectric strength measurements, particularly for this application, is the influence of material deformation. Experiments show that dielectric strength of the material actually increases with strain from about 40 MV/m (unstrained) 240 MV/m (area expansion over 6x) [10,47,48]. The exact cause of this phenomenon is not fully characterized, but it is hypothesized that as polymer chains align in the direction perpendicular to the electric field, the electron mobility is decreased [10].

In this study, several simple experiments are done for characterizing the dielectric strength of the material under various situations. For these tests, the maximum voltage is measured by slowly increasing the voltage until failure. The failure level is highly dependent on the rate of voltage application, so any variations in the speed could cause errors in measurements [49]. In practical situations, the voltage might be applied at faster or slower rates, or even in discrete steps. Therefore, the results obtained form these experiments have a certain amount of scatter, and do not represent exact values. The measurements for a single experiment, therefore, do not necessarily measure the fundamental dielectric strength of the material (in reality, there is no such distinct value), or even the strength for any single application. Instead, these types of experiments isolate and identify how various factors, such as imperfections in the material, affect the reliability of the film.

2.4.3 Film Quality

Experimental observations of early actuator prototypes revealed an inherent inconsistency in the performance of the material. An analytical and experimental investigation was done to understand the mechanisms leading to breakdown and to determine the cause of any inconsistency in the breakdown point.

Premature failure points to inconsistent materials or manufacturing methods of the actuators. Early observations revealed that around 30% of the actuators produced resulted in failure at voltages significantly lower than the expected maximum voltage. It was conjectured that there might be impurities in the film which could cause such failures. Such an imperfection could clearly have several effects:

- A defect, such as a void or inclusion, would create a local decrease in thickness of the dielectric, leading to higher electric fields (defined as the voltage difference divided by the separation) or higher mechanical stresses.
- The impurity could be a conductive particle that would provide a conductive path through the material.

The dielectric failures described above would be classified as surface discharges, or extrinsic failure. In this case, the high electric field suddenly causes bound electrons to be freed and they cascade through the material [45]. Even if the failure is localized, the film can no longer support a potential difference between the electrodes (short circuit). Simple analysis can also show that internal defects, specifically internal bubbles filled with gas, will lead to another means of failure, which begins as discharging within the material. A dielectric film with a void in it can be modeled as a simple arrangement of capacitors in series and parallel, as shown in Figure 9 [45]. The void is assumed to be disk shaped for this example, though the results are typical for any shaped void. The capacitance of the void is expressed as C_v, the capacitance of the dielectric between the void and the other electrode is C_d, and the capacitance of the rest of the dielectric (not directly above or below the void) is C_b.

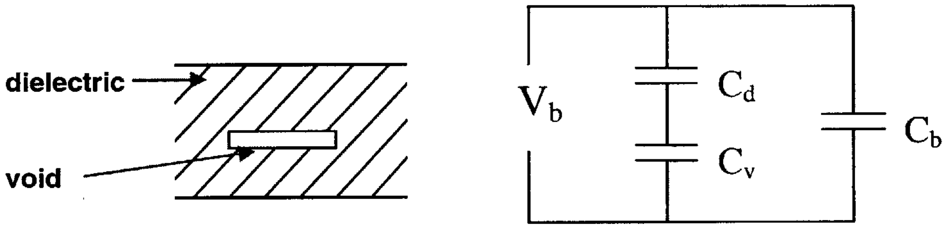

(a) Sectional view of dielectric

(b) Circuit schematic of dielectric with void

Figure 9: Simple model of a void within a dielectric [45].

When the dielectric is subjected to an electric field, the bubble will reduce in size due to the low compressibility of air (7.65x10-6 Pa^{-1}), but it cannot be completely eliminated. Using circuit analysis of capacitors in series and parallel, and the schematic in Figure 9(b), the electric field within the void is given by [45]:

$$E_v = \frac{V_b}{D} * \frac{\varepsilon_d}{\varepsilon_v + \varepsilon_d \frac{d}{D}} \qquad (2)$$

Where D is the thickness of the film, d is thickness of the void, ε_v is the permittivity of the void, and ε_a is the permittivity of the dielectric. If the thickness of the void is much smaller than the thickness of the film, as is likely to be the case if the gaseous void is compressed by the electrostatic pressure, then the expression reduces to:

$$E_v = \frac{\varepsilon_d E_b}{\varepsilon_v} \qquad (3)$$

Where E_b is the nominal electric field through the dielectric. Given the dielectric constant of the material as about 4.5 [10] and approximating the dielectric constant of the gas within the void as approximately 1, the electric field can be approximated to be about 4.5 times that of the field within the dielectric. Furthermore, the dielectric strength of air is significantly less than that of the acrylic (3 MV/m vs 200 MV/m). Therefore, there will be localized ionization within the void. This will manifest itself as arcing as electrons ionize across the surface of the void. As the electrons arc across the void, the internal surface of the film within the void will begin to pit and the gas will heat up. As the pressure increases and the walls break down, localized failures and resulting cracks can propagate, leading to bulk failure within the material.

The presence of such imperfections in the VHB material has not been characterized previously. In order to characterize these imperfections, the material was pre-strained to its working conditions and then examined for such impurities. Visual inspection with the naked eye alone reveals many potential defects. These features are not visually apparent before pre-strain, but as the film is stretched, they "appear." One such feature is shown, magnified 100x, in Figure 10(a). Figure 10(b) shows a view magnified 400x. The exact nature of the imperfection is not obvious, but in the magnified view a small bubble is obvious. It is suspected that the non-distinct, darkened regions are small pitted regions. The occurrence of these is totally random. For several samples, they appear on average at a frequency of about 1/20 cm^2.

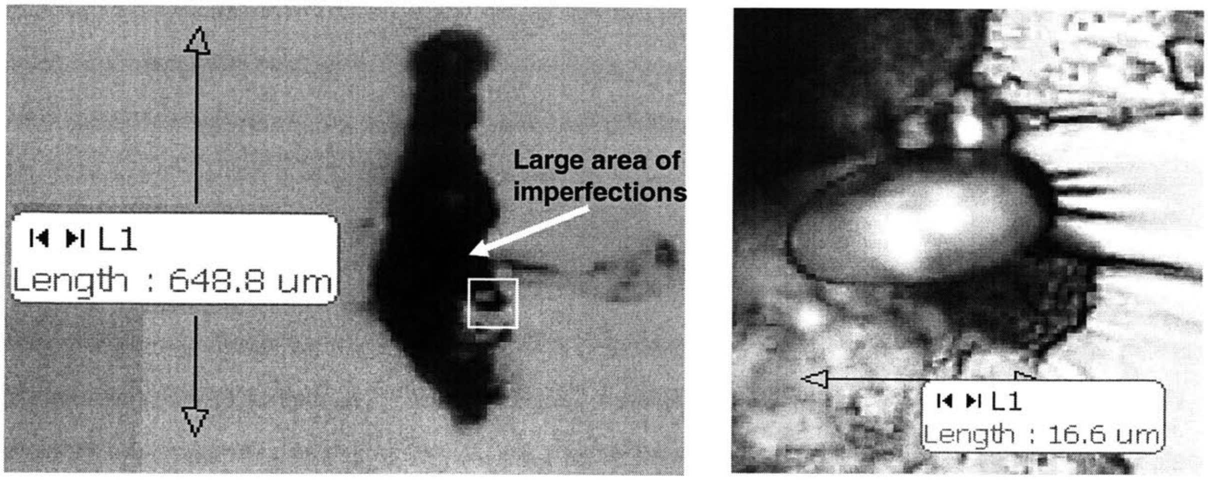

(a) **(b)**

Figure 10: A single imperfection in a piece of VHB film, magnified at 100 and 400x.

The nature of these imperfections is not completely known. Typically, when a dielectric is manufactured, extreme care is taken to prevent the formation of voids. For example, a rigorous vacuum treatment is used to remove gaseous pockets from within the polymer in its liquid state. However, since VHB is actually manufactured for commercial use as a double-sided adhesive tape, the presence of gaseous pockets or foreign particles does not have a significant effect on its performance, and it is not necessary to eliminate them. A description of the exact process used to develop this material is protected information, and therefore the precise nature and cause of the foreign particles in not known.

In order to experimentally determine what effects, if any, these have on the strength of the film, the dielectric strength of a region containing such an imperfection was compared to that of an area not containing such an imperfection. This was done by applying a very small amount of compliant electrodes onto the film and then ramping up the voltage on these electrodes until failure. An illustration of the experiment is shown in Figure 11.

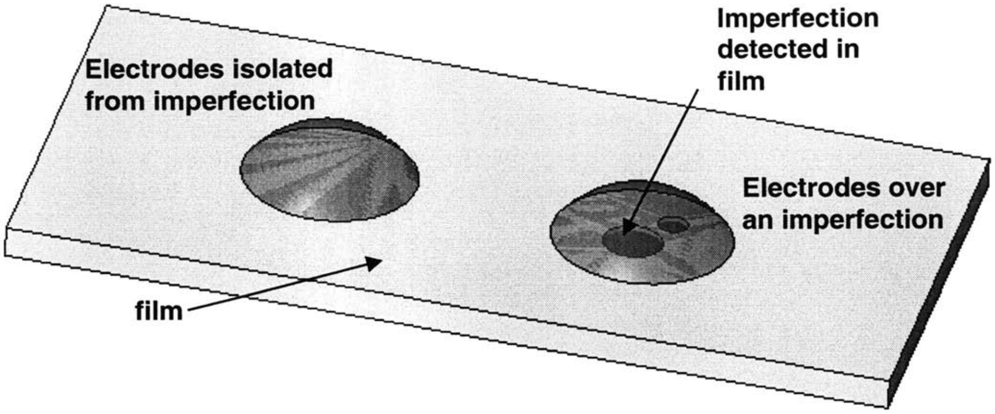

Figure 11: Breakdown testing for two different cases, both over and isolated from visually detected imperfections.

A sample of the raw data is shown in Figure 12. It can be seen that there is a significant decrease in average dielectric strength when large visual imperfections are observed. The scatter in the data is most likely due to the fact that each imperfection is unique, so it will have different stress (electric or mechanical) enhancing effects on the materials

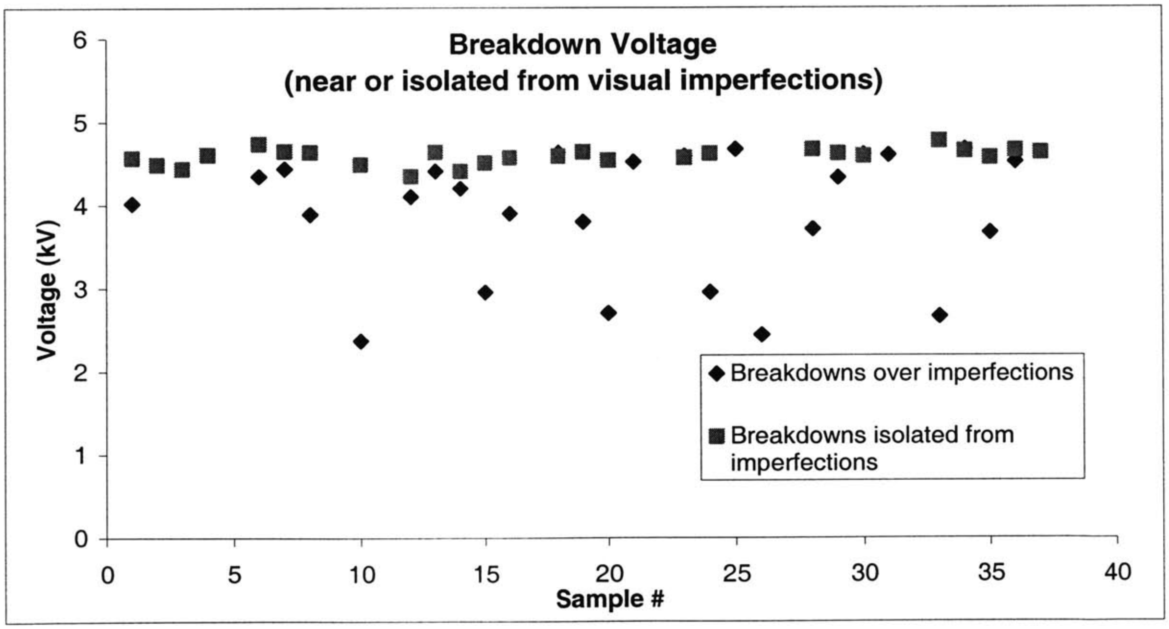

Figure 12: Failure voltage from electrodes both adjacent to and far from visual imperfections.

There is clearly a negative effect due to the visual imperfections. Though a few samples breakdown at the expected level (approximately 4.6 kV), most of them fail at significantly lower values. The average breakdown value for the two sets is 3.91 kV and

4.58 kV, a difference of about 17%. Also, the standard deviation for the "over imperfection" case is 0.75 kV, and only 0.10 kV for the "clean" case. This indicates that nature or size of the imperfections is irregular and their effects are inconsistent.

Other samples were then examined for the presence of smaller, or microscopic, imperfections or voids. A magnification of 400X was used to scan the film for such imperfections. Several candidate imperfections were found, such as the one shown in Figure 13. Identification of such imperfections is very difficult. These were determined to be inclusions within the material because they could only be brought into focus in planes between the surfaces of the film and because each occurrence appears to have a vertical aspect ratio, the same direction of the pre-strain. If there is a small inclusion or cluster of inclusions, pre-stretching the film primarily in one direction would cause an elongation of the cluster in that direction.

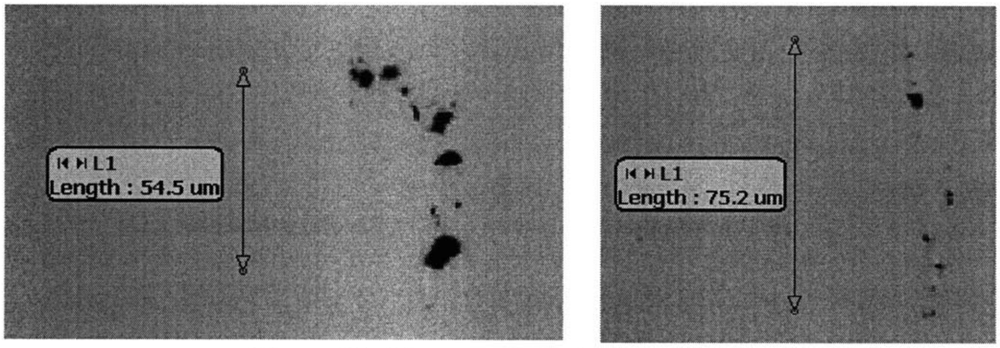

Figure 13: Microscopic inclusions or void.

The process of determining the potential effects of these clusters was investigated in the same way as the larger imperfections. The raw data from these experiments is shown in Figure 14.

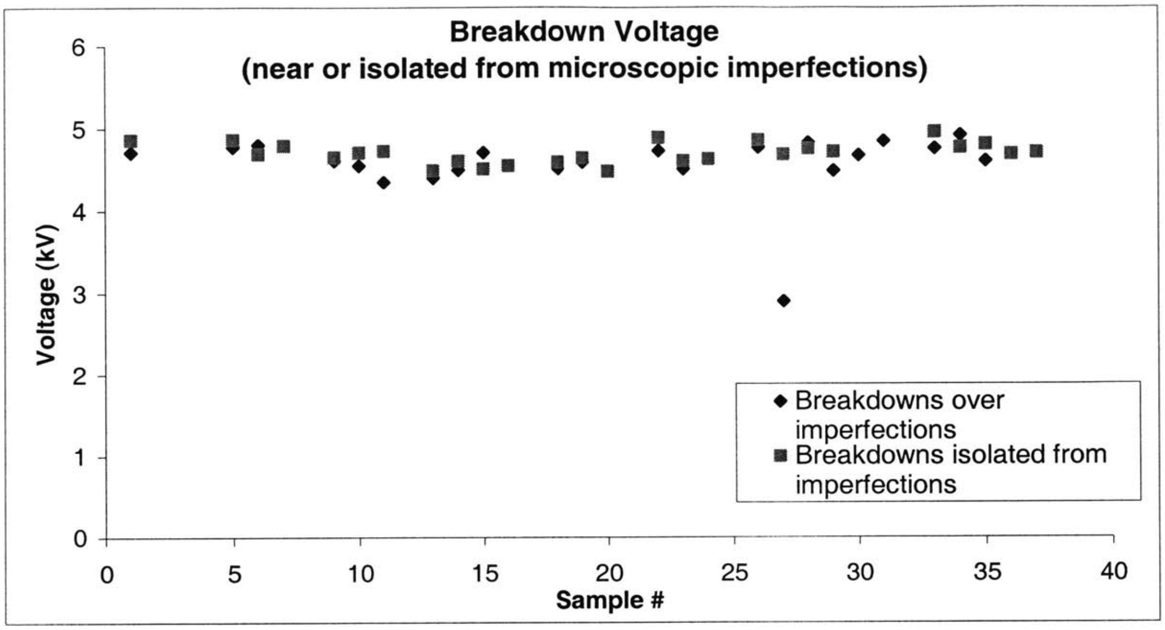

Figure 14: Failure voltage from electrodes both adjacent to and far from microscopic imperfections.

The majority of the points for both testing conditions have very similar breakdown values. However, one point (1 out of 25) lies significantly below the trend and indicates a premature failure. There are two possibilities to explain the single point that lies well outside the trend:

- It had nothing to do with the imperfection (possibly due to undetected human error during testing), and can be discarded.
- It was caused by the imperfection, and this imperfection had a much more significant effect on the dielectric strength than the other microscopic imperfections.

With the data available, it is impossible to determine the cause, and with the number of points available, the "outlier" cannot be discarded. To determine its effect, a statistical analysis of the data sets, considering both possibilities, is shown in Table 2.

Table 2: Statistical analysis of failure data (breakdown voltage)

		Average (kV)	Standard Deviation (kV)
Visual imperfections (macroscopic)	Directly over	3.91	0.75
	Isolated from	4.58	0.096
Microscopic imperections	Directly over	4.48	0.395
	Isolated from	4.61	0.124
Microscopic imperfections (bad point discarded)	Directly over	4.55	0.151
	Isolated from	4.61	0.124

By dropping the point, the difference between the averages is negligible (1%). Even with the point, the difference is only 3%.

If the imperfection that was detected did cause the failure, this data indicates that it was a different type of imperfection (for example, it may have been a conducing particle) than the other microscopic imperfections, which in general do not cause pre-mature failure. Most detectable imperfections are "harmless" (over 95% of those found). For future tests, more powerful examination tools should be used so that the specific nature of each imperfection can be determined. General guidelines for avoiding only hazardous imperfections, such as the one found in this experiment, cannot be put into effect if these cannot be separated from harmless defects. It may also be possible, once the nature of this single point is characterized, to use detection methods other than visual inspection. For example, if only metallic microscopic imperfections are hazardous, then these could simply be found and eliminated using a metal detector. For future investigation of microscopic imperfections, it is necessary that more dependable and efficient detection methods be developed so that larger and more reliable data sets can be achieved.

Though this experiment does not reveal any significant negative effects for most microscopic inclusions or voids, such effects *cannot* be ruled out. In section 2.4.4, an investigation of stress concentrations at the edges of electrodes will show that failures are most likely to occur at electrode edges, and therefore the effects of most microscopic imperfections might be negligible in comparison (while large defects definitely cause pre-mature failures) to the breakdown mechanism at the edge of the electrode. However, it stands to reason that if stress concentrations at the edge of the electrodes were to be eliminated by future design or fabrication methods, then small film defects might become a more significant factor. Furthermore, the mechanism of failure by internal discharging is a time dependent effect [45]. The pitting and heating within these voids might not cause failure within the time domain of these tests, but for large actuation times or cycles, the material strength at these locations will decrease, so that in time failure might occur.

The presence of gaseous voids within the film can also lead to non-negligible current flow through the material. In the ideal case, with a perfect dielectric between the electrodes, there would be zero current flow. However, no polymer is a perfect dielectric, and there is charge leakage through the film. A constant (though low) supply current is necessary to maintain a constant voltage across the film. In the normal case, with high quality film (two films laminated together with no visual air bubbles) approximately 200 microns thick and with an area of 10 cm^2, and a potential difference of approximately 3 kV, the current through the actuator is on the order of 1 μA. Another film with the same area and thickness was also laminated. However, during the assembly process, several air bubbles were purposely trapped between the two films. These bubbles covered about 10% of the actuator area. In this case, the current was on the order of 100 μA, approximately 100x greater than for the standard case. Premature failure was not induced because the electric field was maintained at a voltage significantly less than the breakdown value.

The effect of increased current leakage is significant from an efficiency point of view. The power dissipated by an element is equal to the product of the potential difference across and the current through the element. An increase of the current by a factor of k will effectively decrease the efficiency by a factor of k.

The major conclusion that can be obtained from these simple experiments is a qualitative design rule. The film should not contain any visible voids or defects that can be detected by the naked eye, as they significantly decrease the strength of the material. While *most* microscopic imperfections appear to have no effect on material strength, some may have detrimental effects. If the process for detecting and identifying these is very difficult and time consuming relative to the effort required to build the actuator (as is the case for current methods), and very few microscopic imperfections are likely to cause premature failure (less than 5%), then it would be more efficient to fabricate the entire actuator and then test it, and then discard the entire actuator if it fails at that time.

2.4.4 Electric Field Concentrations

Experimental data also revealed that dielectric failure consistently occurs at the edges of electrodes. Initially, these types of failures were observed at the edges of the electrode where it meets a supporting frame. Preliminary hypotheses identified the cause of these failures as either mechanical stress concentrations or electric field concentrations. Mechanical stress concentrations could be due to the change in boundary conditions where the film is constrained to frame.

Experiments were performed to determine if film was more likely to fail because it was adjacent to a constrained edge. First, electrodes were applied to the center of the film, away from external frames, and the potential difference between the electrodes was increased until failure. Visual inspection showed that failures still occurred on the perimeter of the electrode. A second experiment showed that maximum voltage levels do not change based on the proximity to constrained edges, as illustrated by the data in Figure 15. Breakdown voltages were measured for electrodes placed both next to and away from rigid frames. The difference in the averages for the two data sets was about 2%, showing no clear difference between maximum sustainable voltage between the two cases.

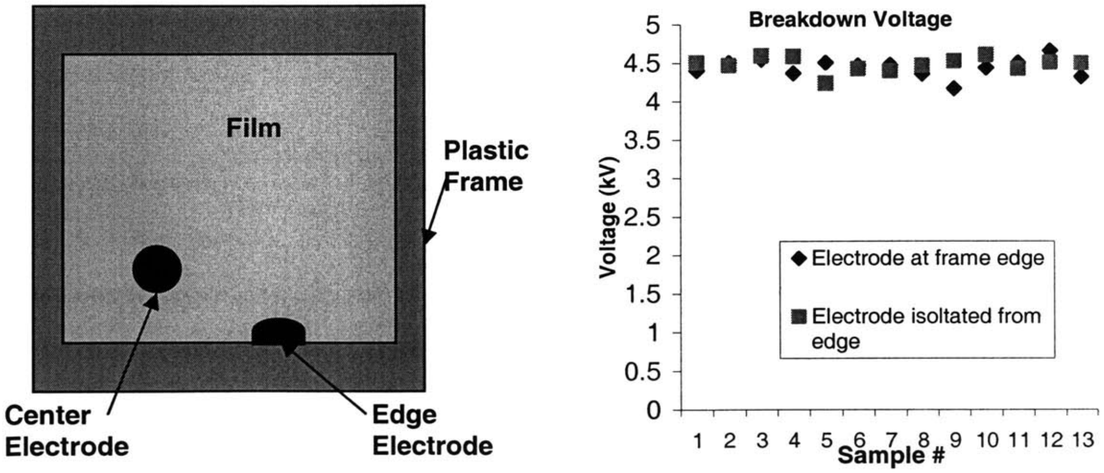

Figure 15: Experiment showing no correlation of breakdown strength to adjacency to frame.

The results of these experiments indicate that there is a tendency to fail at the edge of electrode, regardless of whether or not the film is in contact with an external structure. It was hypothesized that this is caused by an electrical phenomenon, leading to either a lower overall dielectric strength for the system or regions of increased mechanical stress.

2.4.4.1 Analytical Development

In order to verify this, the electric field inside the dielectric must be calculated. It is generally assumed that the electric field throughout the dielectric, between the electrodes, is given by [50]:

$$E = \frac{V}{t} \tag{4}$$

This is the exact value for two parallel infinite plates with a potential difference of V and uniform charge densities. However, for a conductor with finite dimensions (i.e. the electrode of a DE actuator), the charge density will not necessarily be constant across the entire surface, and for most geometries, it *cannot* be constant or else certain regions of the electrode would be at a higher potential (which is impossible for a conductor in a static condition). Equation (4) does not describe what is happening near the edge of the electrode for finite cases. A simple method for obtaining the electric field near the edges is to approximate it using an iterative calculation known as the *method of relaxation* [50], to solve the governing equations with the appropriate boundary conditions. The system is modeled as two parallel plates, offset by a dielectric of thickness t, in a 3-dimensional space, illustrated in Figure 16. The space is discretized into a high resolution grid. All points falling within the electrode's space are assigned a potential of either V_{max} or V_{min}. Points located on the boundary of the space, or the edge of the grid, are assumed grounded. The boundaries of the space are placed far enough away from the electrodes to not influence the edge effects that are being investigated.

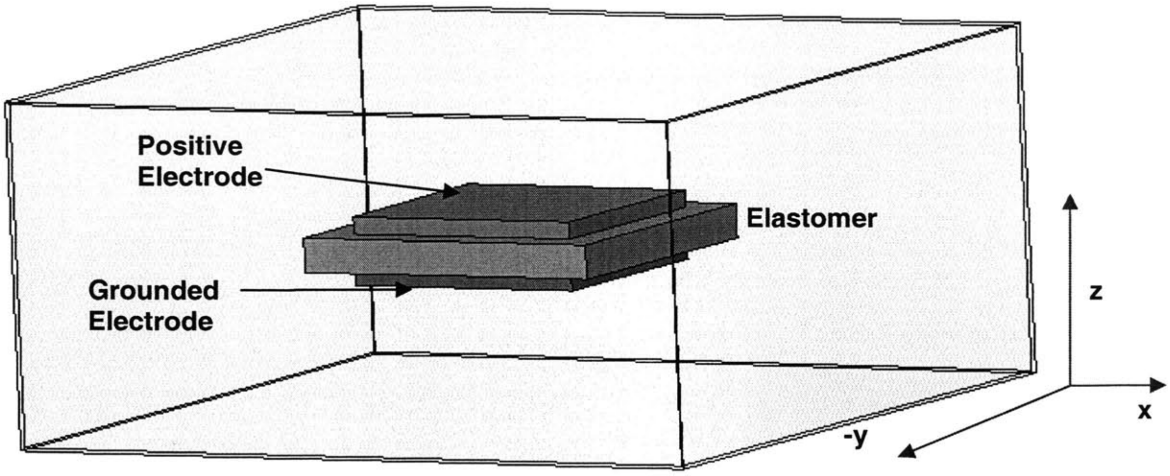

Figure 16: Schematic of 3-dimensional electrostatic model.

In order to simplify calculations, the depth (y-direction) of the three dimensional space can be considered infinite, since we are initially only interested in electrical effects at the edge of the electrodes (therefore effects at the corners of an electrode are not yet considered). If the depth is considered infinite, then the cross section of the space does not change. A representative view of the cross-sectional grid at any location is represented by Figure 17.

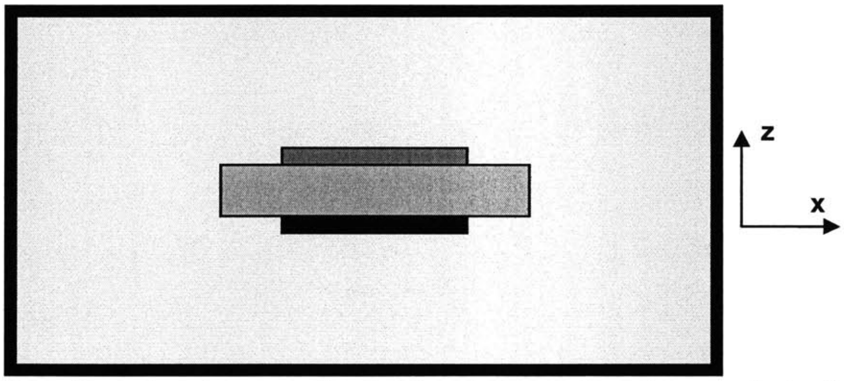

Figure 17: Two-dimensional space: all points located on a boundary or electrode are held at assigned potential values, and all points throughout the rest of the space are iteratively solved for.

All of the darkened points are assigned constant potential values that will not change. The points on the edges are considered grounded, one electrode is grounded, and the other electrode is assigned a constant, non-zero value. The boundaries are set far away from the electrodes so as to not affect the potential fields around the electrodes. All other points are initially set to a potential of zero but are not held to this value during the iterative solution process.

The potential field can be solved analytically using the appropriate boundary conditions and Laplace's equation [50], which is given by:

$$\nabla^2 V = -\frac{1}{\varepsilon_0}\rho \tag{5}$$

Where V is the electrical potential distribution and ρ is the spatial charge density. However, solutions to this equation in 2- and 3-dimensions are very difficult to obtain except for special situations that exploit symmetry in the system. The general solution to this equation, however, yields an important property common to any function that satisfies Laplace's equation:

$$V(P) = \frac{1}{4\pi R^2}\int_{sphere} V\,da \tag{6}$$

Which states that the potential at a point P is the average value of the potential over the surface of a sphere centered at point P [50].

Using this property, each point in a 3-dimensional grid should have a potential that is approximately equal to the average of the 6 points adjacent (and equidistant) to it. Beginning with the defined boundary conditions, each value in the grid is iteratively updated by averaging the values of the potential of the points closest to it. This is illustrated in Figure 18.

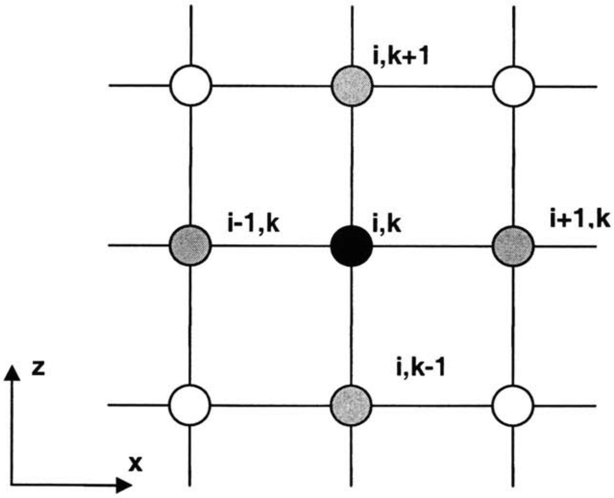

Figure 18: The charge at a single point (darkly shaded) can be computed by averaging the potentials at the points adjacent to it (lightly shaded). Two additional points are located in the adjacent planes (at position (i,k) offset in the y-direction, in planes j+1 and j-1).

Following each iteration, the boundary conditions (grounded boundaries and constant voltages on the electrodes), are reset. The iterations continue until they make insignificant changes to the potential field. The electric field and charge densities can easily be calculated using the gradient of the resulting potential.

The computations were performed in MATLAB. A two-dimensional matrix was created and the initial conditions set as described previously. This is iteration 1. For each subsequent iteration, a discrete representation of the integral in equation (6) is used to reassign each value in the matrix:

$$V_{i,k} = \frac{V_{i+1,k} + V_{i-1,k} + V_{i,k+1} + V_{i,k-1} + 2 * V_{i,k}}{6} \tag{7}$$

Where i and k denote spatial positions. The first four terms in the numerator refer to the potential at the adjacent points in the 2-dimensional grid. The last term refers to the value of the original point, which also represents the potential at the adjacent points in the neighboring planes (offset in the y-direction). This is valid since the case is considered infinite in one direction. This process continues for each iteration until the values reach a steady state. The resolution of the grid must be uniform to allow the property of equations (6) and (7) to be used and quite small in order to reach solutions that represent the true solution.

Obviously, computing the averages one point at a time with nested loops would be inefficient. Therefore, matrix multiplication was used to update the entire grid with a single expression. If $\underline{V}_n$ is an MxN matrix of potentials, then the updated matrix $\underline{V}_{n+1}$ is given by:

$$\underline{V}_{n+1} = \frac{1}{6}\left((\underline{U} + \underline{D}) * \underline{V}_n + \underline{V}_n * (\underline{L} + \underline{R}) + 2 * \underline{V}_n\right) \tag{8}$$

Where $\underline{U}$ and $\underline{D}$ are square matrices of dimension N that shift the values in the matrix $\underline{V}_n$ up or down by 1 row, and are given by:

$$\underline{U} = \begin{bmatrix} 0 & 0 & \cdots & & \\ 1 & 0 & 0 & & \\ 0 & 1 & 0 & 0 & \vdots \\ \vdots & 0 & 1 & 0 & 0 \\ & \cdots & 0 & 1 & 0 \end{bmatrix} \quad \underline{D} = \begin{bmatrix} 0 & 1 & 0 & \cdots & \\ 0 & 0 & 1 & 0 & \vdots \\ \vdots & 0 & 0 & 1 & 0 \\ & & 0 & 0 & 1 \\ & & \cdots & 0 & 0 \end{bmatrix} \tag{9}$$

$\underline{L}$ and $\underline{R}$ are matrices of dimension M that shift the values in the matrix $\underline{V}_n$ to the left or right by one column. These matrices look the exact same as $\underline{U}$ and $\underline{D}$, but are of a different dimension. This method can be implemented for a three dimensional matrix by slicing a three dimensional grid into two dimensional slices and doing the equivalent matrix multiplications in three dimensions.

The electric field is a vector function, having a component in each axis. It can be calculated as the gradient of the potential field, using:

$$\vec{E} = -\nabla V \tag{10}$$

After the potential function grid is generated, the electric field in each direction can be found by calculating the approximate gradient through the discrete grid. Mathematically, this is also done with matrix multiplications. For example, the electric field in the z-direction is given by:

$$\underline{E_Z} = \frac{1}{2}(\underline{U} - \underline{D}) * \underline{V} \tag{11}$$

2.4.4.2 Results

For a typical case, in which the planar dimension (x) is significantly larger than the thickness dimension (z), a view of the potential field, as you move from the bottom of the space, through the center of the electrodes, to the top of the space, is shown in Figure 19.

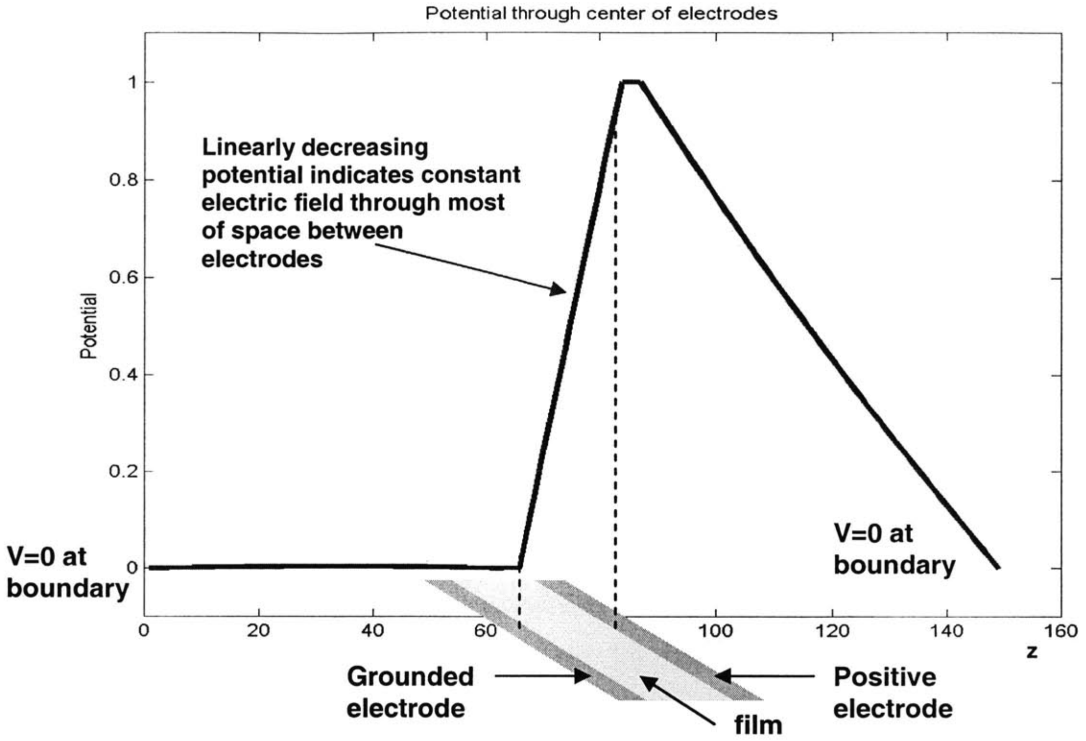

Figure 19: *Potential field: the peak represents the positively charges electrode, the negatively charged electrode is held at ground, equal to the boundary potential.*

The peak of the plot is the potential that the high voltage electrode is set at. From this value, the voltage drops off to zero at the grounded electrode and boundaries. The linearly decreasing potential field indicates a constant electric field (electric field is the gradient of potential). Since this plot is only looking through the center of the electrodes and not at what is happening near the edge, then this is the type of profile you would expect for the infinite, ideal case. An isometric view of a 3-dimensional plot, so that the potential over the entire *x-z* plane (not just at *x=200*, as in Figure 19), is shown in Figure 20. This view helps show what is happening near the edges of the electrodes.

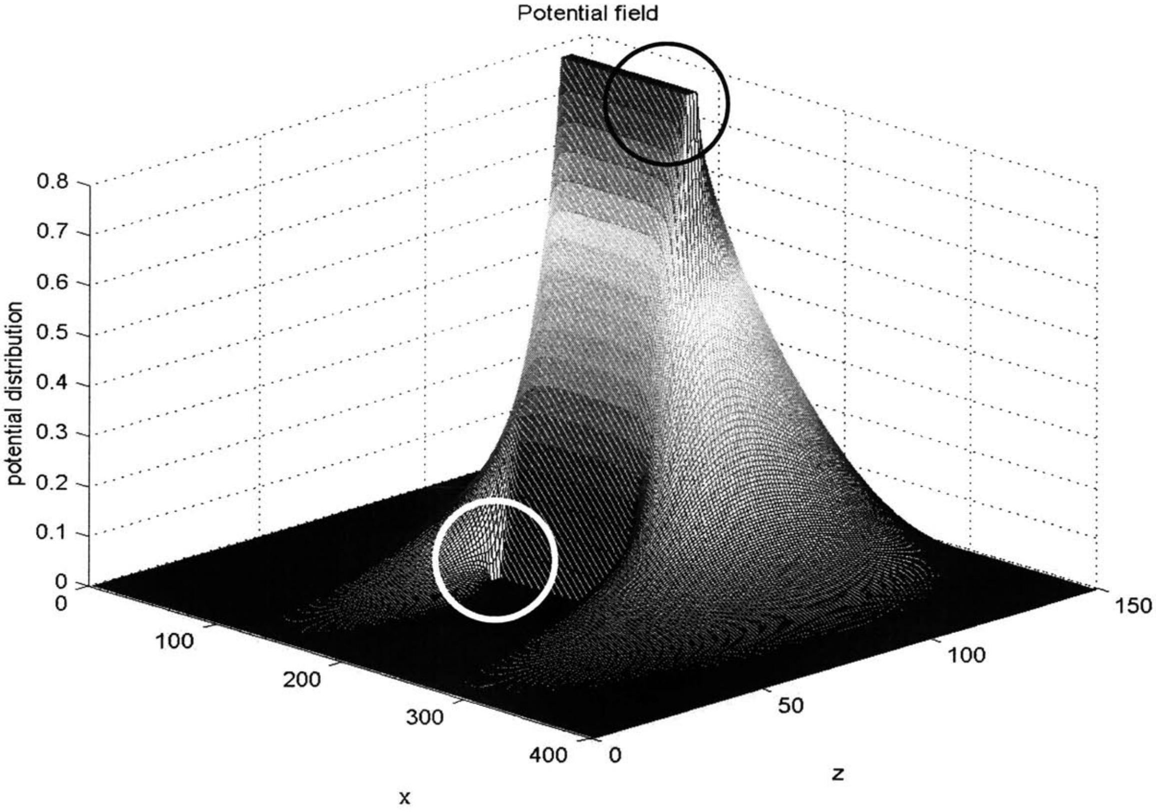

Figure 20: Potential field over the x-z plane. One edge of each electrode is highlighted.

Inside the highlighted areas, each of which indicates an electrode edge, of Figure 20, there are very steep changes in the potential field. The electric field resulting from this potential is calculated using equation (11). A plot of the electric field at several depths within the dielectric, as a function of x, is shown in Figure 21. The endpoints of the electrode are at 150 and 250. At zero depth, or just inside the electrode surface, there are concentrations in the electric field the electrode edge. As the distance into the deielectric increases, the spikes diminish. At about 30% of the depth, they are no longer present. In the center of this range, the electric field at any depth equals its nominal value, that given by equation (4). Outside of the electrode range, the electric fields drops steeply to zero.

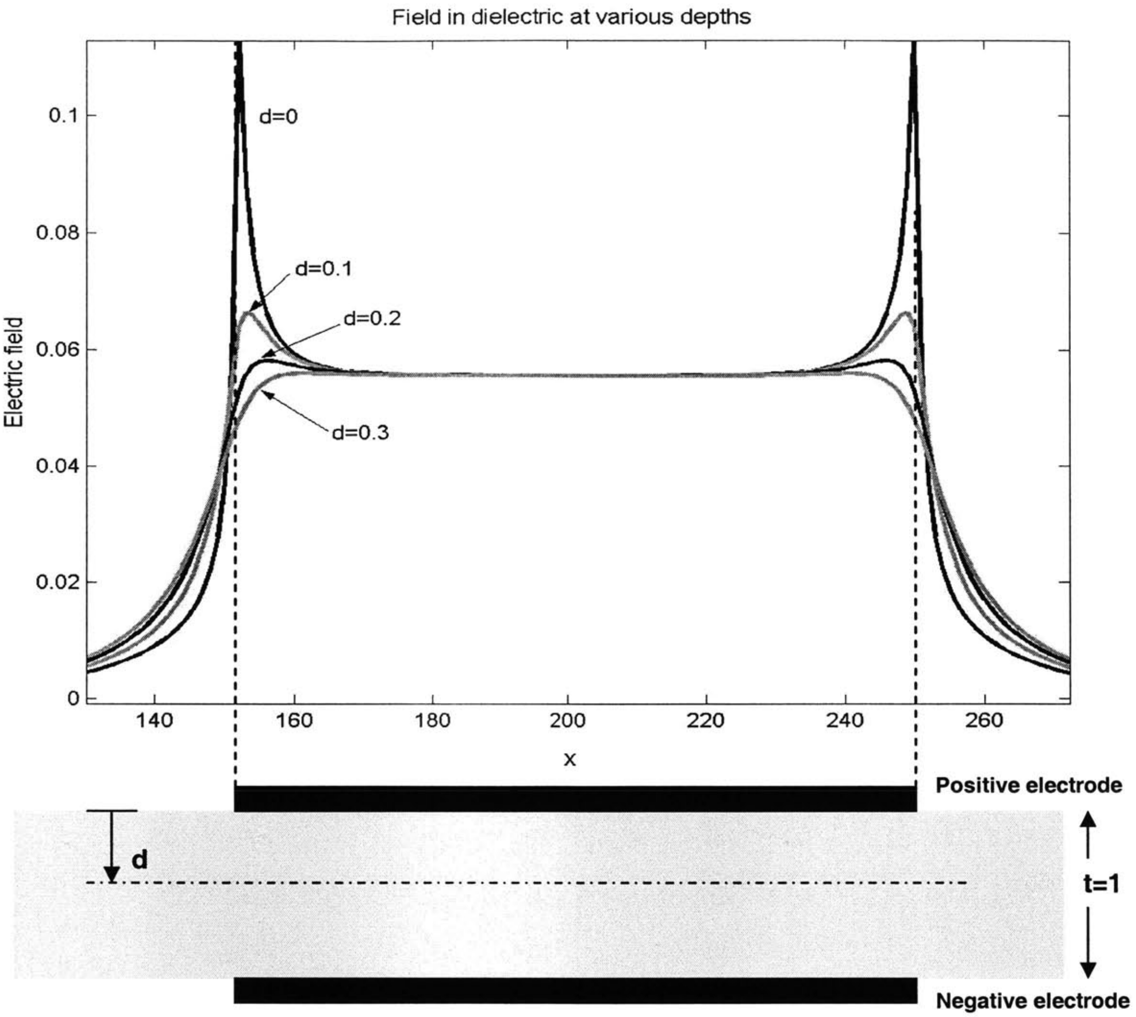

Figure 21: Plot of electric field at several depths within the dielectric, as a function of the lateral position, electrode edges are located at x=150 and x=250.

The spikes at the edge of the electrodes are significant. This concentration factor is highly dependent on the resolution of the grid. As the number of points is increased and the test grid approaches a continuous distribution, the height of the spikes become greater, approaching infinity. Theoretical solutions to Laplace's equation for axis-symmetric cases, which are highly dependent on symmetry and simple geometries, also show such infinite fields [51].

The most intuitive way to describe the occurrence of these field concentrations is by considering the charge density on the electrode. For the entire electrode to be held at a constant potential, the charge density will concentrate at the edge of the electrode. This is known from the fact that the potential at a point can be calculated using superposition [52]:

$$V_P = \frac{1}{4\pi\varepsilon_0}\sum_{i=1}^{n}\frac{q_i}{r_i} \tag{12}$$

The potential at any point on the electrode is affected by all of the charged particles on that electrode. If the charge was distributed uniformly across the electrode, then points toward the edge of the electrodes would have lower potentials because they are further away from the rest of the charges. Points in the center of the electrode would have very high potentials because they are near (relatively) all of the charges. Therefore, for the entire electrode to be held at a constant potential, the charge will concentrate at the edge of the electrode. The electric field immediately outside of a conductive plane is normal to the surface of the conductor and proportional to the charge density on the surface, and is given by [52]:

$$E = \frac{\sigma}{2\varepsilon_0} \tag{13}$$

The analysis described above was performed to calculate the potential over through a 3-dimensional space, and from that matrix the electric fields and charge densities can be obtained using equations (5) and (10). Similar matrix operations as those described to calculate the electric field were used to calculate the charge distribution. As shown in Figure 22(a), charge will tend to concentrate at the edges of the electrodes, particularly in the corners. Likewise, the electric field for the plane just inside of the electrode is shown in Figure 22(b). The shape of the field looks identical to the charge distribution. This is expected, since the electric field outside a conductor's surface will be proportional to the charge density (equation (13)).

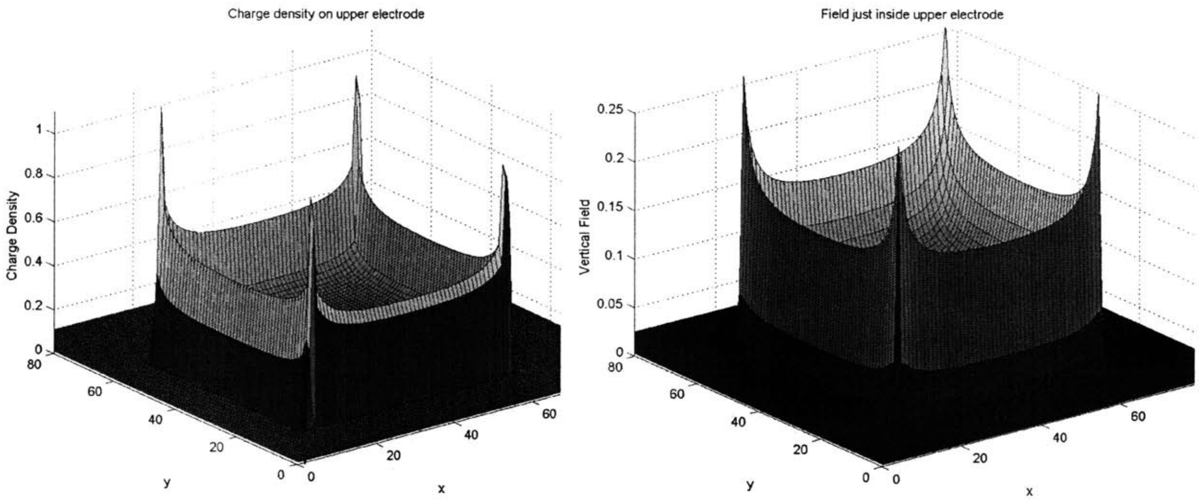

Figure 22: Charge distribution and electric field at the surface of a rectangular electrode: high density is apparent at edges and corners.

In addition to the edge effects for regular electrodes, the model can also be used to identify the effects of "irregularities" in the electrode. For example, while applying an electrode to the film, the border may not be smooth, as shown in Figure 23.

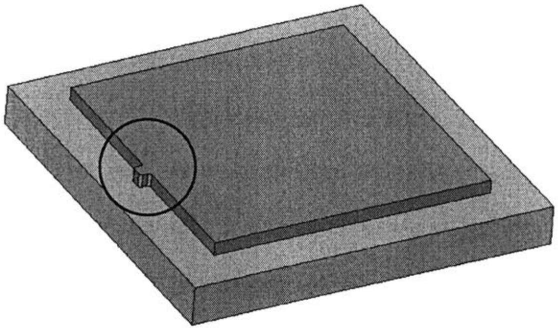

Figure 23: Example of an irregularity on the edge of an electrode.

The electric field over this electrode can be computed, and the results are shown in Figure 24. As predicted, the electric field is significantly higher at the edges and corners, but there is now also a spike over the area where there was irregularity in the electrode, similar to those seen at the corners. Calculating the exact influence of such irregularities in the electrode is difficult since it is highly dependent on the shape of the "irregularity," but the relative importance of achieving uniform edge conditions for the electrodes is demonstrated by the model.

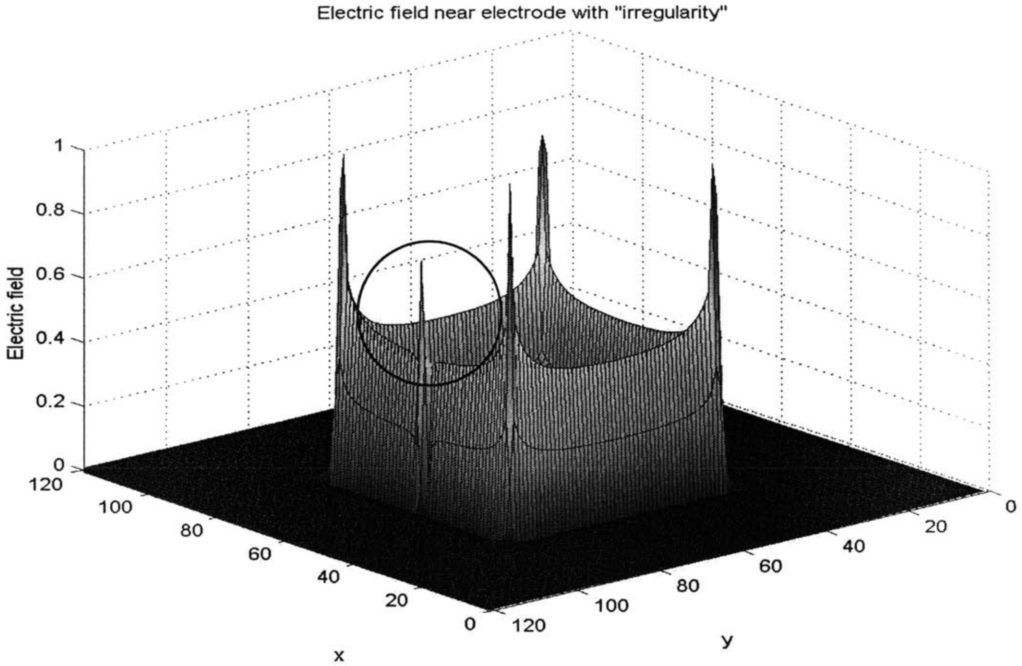

Figure 24: Electric field over a square electrode with an irregularity at its edge.

In order to observe the significance, if any, of these theoretical concentrations, an experiment was done to verify presence of increased electric field at the edge of the electrodes. The dielectric film was stretched over a large aluminum plate. The plate was grounded, forming the lower electrode. On the other side, an electrode with either sharp or rounded edges, also made of aluminum, was attached to the film. The smooth, rounded edge will theoretically reduce field concentrations due to sharp edges or irregulairties. The voltage between the opposite electrodes was slowly ramped up until failure. The test setup is shown in Figure 25.

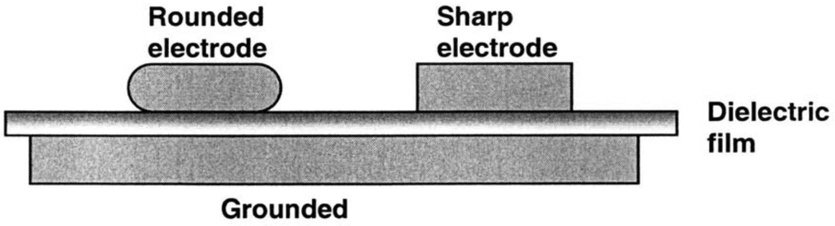

Figure 25: Experimental setup for determining quantitative value of edge effect.

Since the electrodes are rigid and form a strong bond (VHB material sticks very well to metals), and their lateral dimensions are much greater than the thickness of the film, it can assumed that the film beneath the electrodes is constrained, and there is no deformation. The results are shown in Figure 26. Despite the scatter in the data, which is likely due to variations in the speed of voltage increase, there was noticeable difference between the two cases. The average breakdown voltage for the situation with rounded electrodes is about 9% higher than that for sharp electrodes. Obviously, these numbers are much lower than the magnitudes predicted by the numerical model.

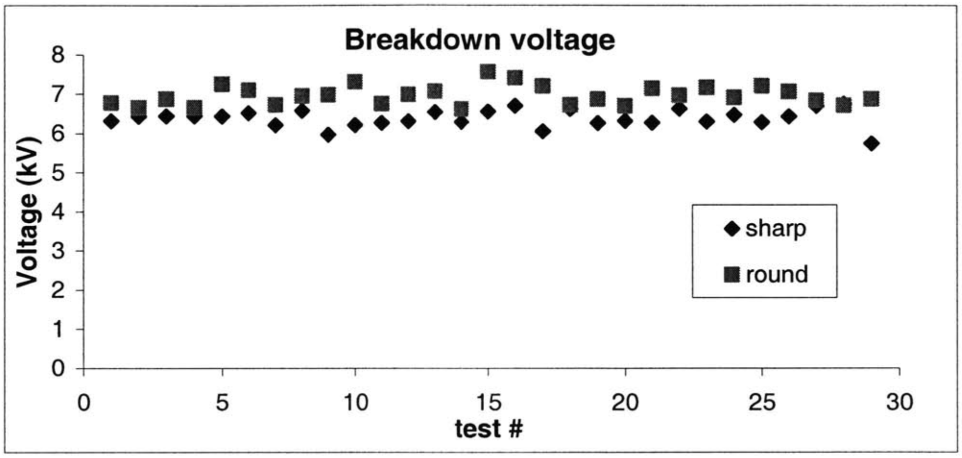

Figure 26: Comparison of breakdown strength for both sharp and round electrode cases.

2.4.4.3 Discussion

It is important to recognize the significance of the 9% increase in dielectric strength. If an actuator fails at 9% higher voltages when edge effects are reduced, then according to equation (1), the maximum pressure that could be generated without edge effects would be $1.09^2=1.18$ times the regular pressure. An 18% higher pressure could create significant increases in the actuator's performance. While this experiment does not exactly represent an actuator system since the electrodes are of different dimensions and materials, it does experimentally verify the presence of edge effects.

If a material has a finite dielectric strength, then the presence of infinite electric fields, which can theoretically be generated from even small voltages, would cause failure. Obviously, materials do not experience total failure at very small voltages, and for the experiment described above there was only a 9% difference in sustainable voltage between the case with and "without" edge effects. The explanation can be seen by inspecting the plot of the electric field between the electrodes, as previously shown in Figure 21. The very large electric fields are only present in limited region very close to the edge of the electrode, and they do not extend all the way through the material.

Therefore, dielectric failure will initially occur only in these small regions, not all the across from electrode to electrode, as illustrated in Figure 8. This is illustrated in Figure 27. The occurrence of this dielectric failure may not initially cause failure, since the material can still sustain a potential difference between the two electrodes, but as this voltage application is increased, the dielectric failure will cause a slow deterioration of the material, causing cracks to propagate and eventually leading to eventual bulk failure by electric or mechanical means.

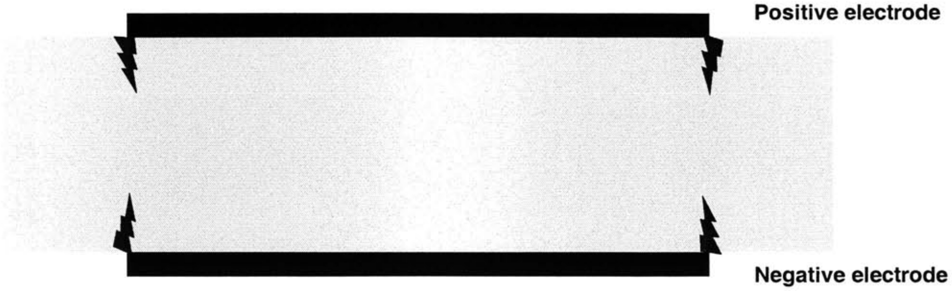

Figure 27: Dielectric failure limited to small regions.

Aside from the decrease in dielectric strength of the system, the increased electric field would also cause increased electrostatic pressures (equation (1)) in the regions near the edges, so that mechanical stress concentrations will also reduce the strength of the elastomer.

Though not previously reported in the DE actuator literature, the electrical edge effect has been seen experimentally in the field of dielectric and polymer science. During standard dielectric strength testing, polymers are often shaped in a "Rogowski" profile, as shown in Figure 28[49]. Theoretically, such geometries can eliminate electric field concentrations. This is analogous to creating rounded edges on an electrode, as described in the previous experiment.

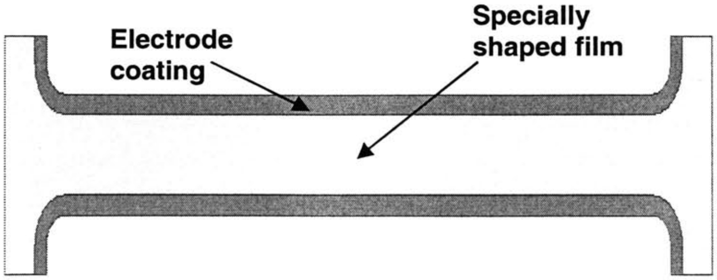

Figure 28: Film with special geometry for eliminating concentrations in the electric field.

If the dielectric films assembled into actuators can be shaped as shown in Figure 28, possibly by some type of casting or deposition process, it may be possible to eliminate or reduce edge effects. The analytical model described previously can be modified for varying geometries in order to approximate the electric field concentrations for a given geometry.

The exact correlation between electrical field concentrations and *unexpected* edge failure has not been completely characterized. However, an important mode of failure has been identified. Finding ways to eliminate or reduce this, possibly by shaping the edge of the film according to the "Rogowski" profile during fabrication, will improve the baseline performance of the actuator.

2.4.5 Electrical Fatigue

The previous sections describe several phenomena for initialting failure. Several of these failure modes are the result of concentrations in the electric field inside the dielectric. Initially, these concentrations might not yield failure because they remain below the ultimate limits of the system. However, continuous or repeated actuation can eventually lead to failure. This is analogous to mechanical fatigue and *progressive fracture* in mechanical systems. In these cases, small fractures begin with microscopic cracks at locations subjected to high localized mechanical stresses [53]. The presence of small areas subjected to high electric fields would lead to an analogous phenomenon referred to *electrical fatigue*. Analysis has shown that such location of high electric fields occur:

- Near film imperfections
- Inside gaseous voids
- At edges of electrodes
- At sharp corners or irregularities on the edge of an electrode

The presence of these do not necessarily cause immediate failures. The simple experiments presented in this section do identify immediate effects of these, as shown by pre-mature failures near edges and over film imperfections. However, these tests were performed for a single actuation times, and the most significant effect of these field concentrations may be for time dependent effects. For example, most of the experimental points over microscopic film imperfections did not reveal an inherently lower dielectric strength, but extended voltage application may have led to time noticeable time dependent deterioration, thus yielding different results.

Current leakage, which was also briefly described, can also cause electrical fatigue. This occurs due to electrochemical deterioration, and is dependent on the current density and chemical reactivity of the dielectric [46].

Further experiments are required to identify such failure modes and the conditions in which they occur. The prediction of rate of erosion chemical deterioration due to ionization is purely empirical, and depends on such parameters as molecular structure, environmental conditions, applied fields, and concentration factors [46,54]. Such calculations are outside the scope of this investigation, however, it is of great value at this point to simply identify these types of failures and recognize what can be done to prevent them. The *ideal* film would have zero defects. Electrodes should be applied as uniformly as possible, and without sharp corners, to eliminate irregularities in the electric field. Design and fabrication methods could be developed for locally increasing the thickness of the film near the electrodes to reduce the electric fields in those locations.

3 Linear Actuator Design

There are several physical components and parameters that must be determined for developing a linear actuator suitable for integration into any type of device. In this chapter, the major issues will be addressed from both an analytical and experimental point of view. Specifically, the process for designing and fabricating a planar actuator capable of large linear strains is outlined. Planar actuators have proven most effective for obtaining very large displacements, and the ability to increase available forces can be accomplished by efficiently stacking the actuators. Development of the key component for obtaining large strains, referred to here as the "negator," is also described.

3.1 Film Design for Actuators

One of the most significant design parameters affecting the strain capability of a dielectric film is the amount of pre-strain applied to it before assembly. Pre-strain refers to the step in which the polymer film is stretched prior to installation into the actuator structure. Some amount of pre-strain is necessary so that the film is always in tension, otherwise it will buckle upon actuation. The influence of the pre-strain on actuator strain results from both a change in dielectric strength and material stiffness. It has been recognized experimentally that highly asymmetric pre-strain provides for best linear expansion [9,55]. As the film is stretched extensively in one direction (referred to as the *passive* direction), the polymer chains extend to their maximum length, causing a phenomenon called strain hardening in which the film becomes relatively stiffer in that direction [44]. Therefore, the film will expand more in the perpendicular axis (*active* direction) upon actuation. This effect is used to "channel" the output of the actuator in the desired direction.

Although higher pre-strain will increase the dielectric strength of the material, excessive pre-strain may inhibit actuation strain capabilities due to excessive strain hardening. Recent research has shown that there exists an optimal amount of pre-strain for obtaining maximum strains [48]. Though the linear expansion in each direction is highly dependent on the relative pre-strain between the two directions, the amount that the materials area will expand, referred to as the *actuation area expansion ratio*, depends primarily on the combined pre-strain from both axes (*pre-strain area expansion ratio*) [48]. The relevant results from this study are shown in Figure 29.

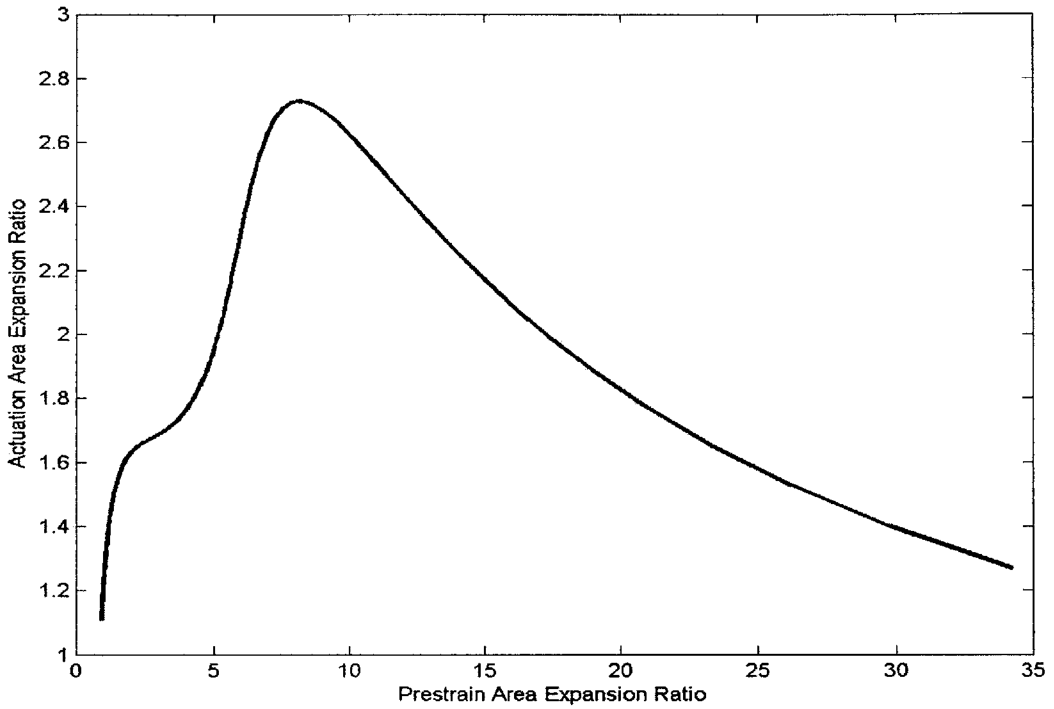

Figure 29: Maximum area expansion upon actuation as a function of pre-strain expansion [48].

In order to obtain the highest actuation area expansion rations for this material, the pre-strain area expansion ratio should be approximately between 7 and 11 [48]. Most of this area expansion should be due to pre-strain in the passive direction. Based on these experimental observations, pre-strains of 400% (in the passive direction) and 100% (in the active direction) are chosen as the assembly pre-strain values, for a total area expansion of *(4.0+1)x(1.0+1)=10.* Experimentally, these values have proven an effective combination in fabricating relatively reliable and high performance linear actuators.

In each of linear actuators fabricated, the film is first laminated (three layers of VHB 4905) to increase both reliability and actuation force. It is found that laminated films are more robust and can withstand higher tensile stresses during assembly. The thicker films can generate higher forces because they support higher tensile loads.

There is a limit to the amount of films that can be stacked. The necessary voltages (over 10 kV) become difficult to manage. Undesired arcing within the power circuitry and between the electrodes occurs. Also, as the film thickness increases, so does the tensile force. If the tensile force exceeds the adhesion force attracting the film to the frame, the film will slip. Film slippage is a difficult problem to characterize, but it has been shown to cause failure in actuators, particularly in regions close to frame pivot points.

3.2 Frame Design

3.2.1 Geometry Selection

Planar DE actuators are composed of the dielectric film and a supporting structure that constrains the film. The shape of the frame should be chosen such that the performance of the film is optimized.

The simplest planar DE is a parallel beam actuator, as shown in Figure 30.

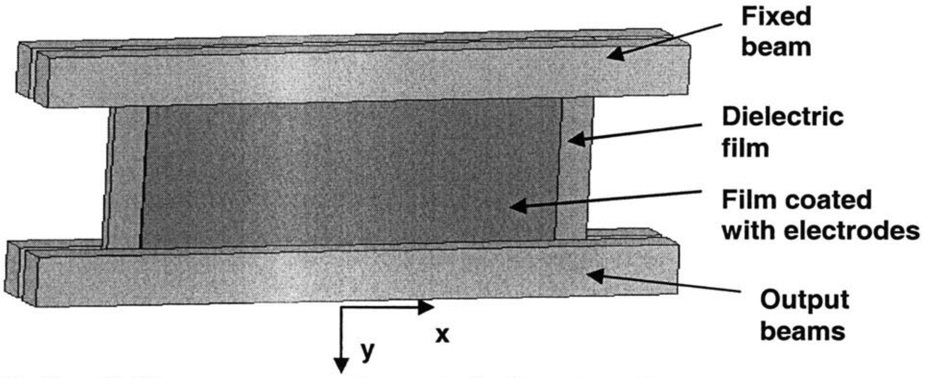

Figure 30: Parallel beam actuator, where x is the direction of maximum pre-strain and y is the output direction.

As discussed earlier, the actuation expansion of the film is greatest in the axis with the least pre-strain. In order for the actuator in Figure 30 to achieve large expansion in the output direction, the greatest pre-strain should be in the x-direction. However, achieving such a configuration is difficult because the stress in the film causes the unconstrained regions to bow in, as shown in Figure 31.

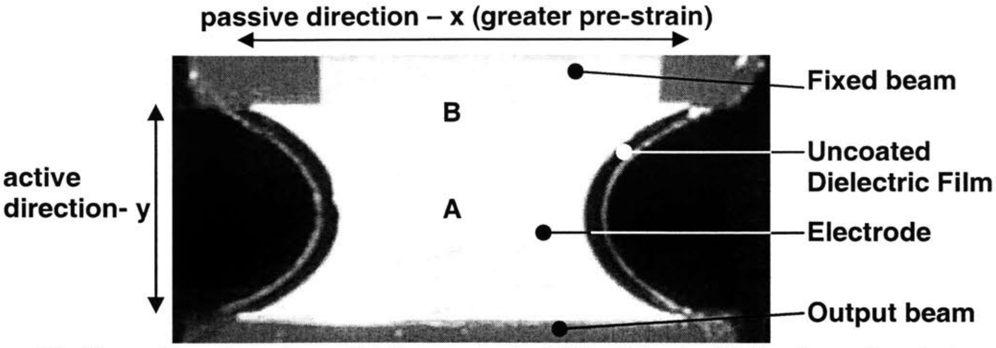

Figure 31: Bowed in effect due to high pre-strain [55]. Film is thicker in region A than in B.

Since the film is bowed in, the entire film does not have the same thickness. It is thicker in the center, region A of Figure 31, where the unconstrained film has a smaller width, and thinner at the edges, region B, where the constrained film has a larger width. Therefore, the electric field and mechanical stresses, which depend on thickness, are not uniform. When constructing a DE actuator in this configuration, care must be taken to maintain a minimal border of uncoated film at the unconstrained edges to avoid arcing around the edges. This embodiment has no torsional stiffness and can only work in tension unless a separate structure is added to maintain tension the film's *y*-axis.

In order to add stability to the actuator, reduce the possibility of arcing around the edges, and eliminate the bowing effect, the frame can be constructed to completely constrain all borders of the film. One approach for accomplishing this is to add diagonal beams connecting the parallel beams, as shown in Figure 32. This design was used for BRAID III [55]. The frame was cut from a solid sheet of Delrin™, a commonly used acetal.

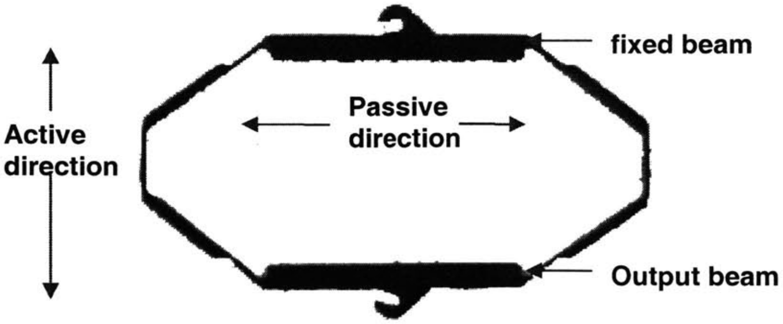

Figure 32: Monolithic frame with complete border [55].

This frame represents just one possible design. In order to determine the optimal design, the geometry shown in Figure 33 is considered. The frame can have values ranging from $b=0$ (diamond shaped) to $b \rightarrow \infty$. When an electric field is applied to the film, its area will change, and the resulting deformation of the frame can be calculated as a function of the area change. The relevant external forces and applied voltages to achieve the area change are ignored. It is assumed that DE technology is scale invariant, so the solution to this problem is independent of actual dimensions.

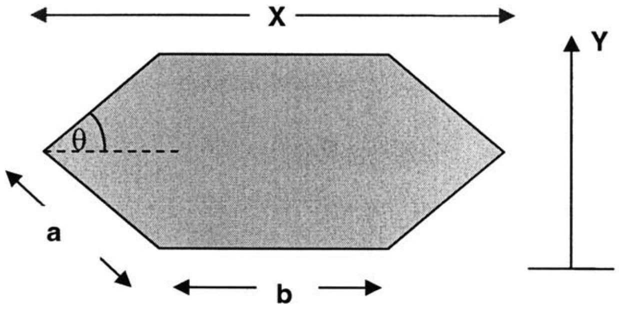

Figure 33: General dimensions for hexagonal frame.

The maximum reported area expansion, upon actuation, of this material has been reported as about 3.3 [47,48]. However, such results appear to be isolated best performances, and a maximum expansion of about 2.75 is a more conservative and practically achievable value [48]. If this area expansion is imposed on the frame shown in Figure 33, then the resulting displacement in the Y-direction can be calculated. Two significant values can be obtained from this. One is the strain in the active direction, which is defined by:

$$\varepsilon = \frac{Y - Y_0}{Y_0} = \frac{\delta Y}{Y_0} \tag{14}$$

Where Y_0 is defined as the intial vertical dimension of actuator film. The other interesting result is the deflection in the active direction relative to the passive dimension, or initial width, of the actuator. This value is given by:

$$\varepsilon_{passive} = \frac{\delta Y}{X_0} \tag{15}$$

To maximize the effectiveness of an actuator, it is desired that its dimensions (in both the active and passive directions), are minimized relative to the actuator deflection. Both of these values are plotted in Figure 34.

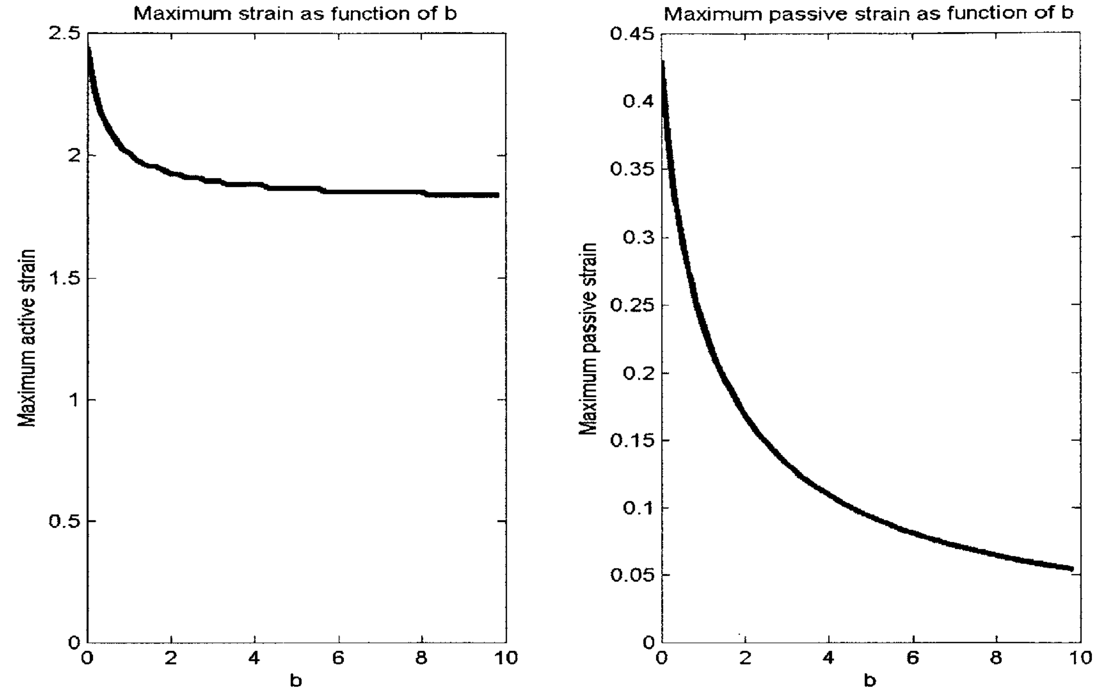

Figure 34: Maximum achievable strain values as a function of frame geometry.

The first plot indicates that frames with minimal values of *b* convert area expansion into linear deflection more effectively. The trend is valid for any area expansion: the required strain is maximized if *b* is minimized. The second plot shows that the deflection of the actuator, relative to its overall width, decreases significantly as *b* is increased.

The previous calculations indicate that frames with small values of *b* have many significant advantages. The diamond shaped frame also offers the very important property of having constant strain values both in the active, *y*, and passive, *x*, directions. When the film is under a uniform pre-strain in both the *x* and *y* directions (not necessarily equal), then all regions of film will undergo the exact same expansion in both axes if the frame deforms, so that the film has a uniform thickness over its entire area.

For non-zero values of b, the horizontal expansion (or contraction) is constrained to zero along the horizontal beam, but in the central region of the actuator, the film is free to deform. Therefore, the strain (and thickness) in the film is not uniform. Variations in thickness will cause variation in both the mechanical stresses and electrical fields throughout the film, so that failure will be significantly more likely in some regions. Furthermore, development of analytical models for describing the behavior of DE actuators can be simplified by the uniform strain assumptions of diamond shaped actuators.

Based on these geometric considerations, diamond shaped frames (which minimize *b*), are the best candidate for linear actuators with large displacements.

3.2.2 Structural Design

In order to fabricate a frame for a DE actuator, several factors must be considered. Experiments were done to iteratively determine what frame material and design was most appropriate. The final design of the frame is shown in Figure 35. Prototype devices were manufactured by cutting 1/8" thick extruded nylon 6/6 sheets using an OMAX™ water jet machine. This machine is capable of 0.005" precision with a cutting diameter of approximately 0.030" [56]. The factors leading to this design are further described.

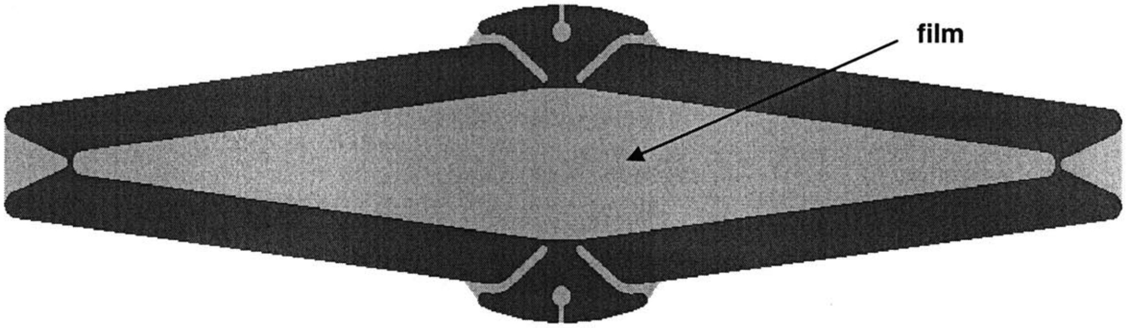

Figure 35: Current frame design.

The use of monolithic frames, rather than assembling a frame out of rigid links and hinges, reduces the complexity of the frame. Also, hinges can lead to high stress regions because of discontinuities in film strain at the joints. The choice of nylon was governed by two major issues. First, the dielectric film must be attached to the frame. For the case of VHB acrylic, this issue is simplified by the natural adhesion of the material to extruded nylon.

The second reason for choosing nylon is that the hinges of the frame can be effectively designed out of nylon. Several approaches can be used when designing the flexures in the frame. One approach investigated as part of this research, though not chosen for the final frame design, is to incorporate the required pre-load element (for maintaining tension in the film) directly into the stiffness of hinges. The stiffness of the frame can then be modified by altering the dimensions of the flexures or the frame material. The simple equations for beam bending can be used for obtaining the desired stiffness. The maximum angle of deflection in a beam is:

$$\phi = \frac{PL^2}{2EI} \tag{16}$$

Where P is the force applied, L is the length of the beam, E is the modulus of the material, and I is the inertia of the beam. The inertia of the beam is given by:

$$I = \frac{bh^3}{12} \tag{17}$$

Where h is the height of the beam and b is the width (in the axis of rotation) of the beam. Therefore, the stiffness of the flexure is proportional to the thickness^3 and inversely proportional to the length^2 of the beam. An example of a design in which substantial stiffness is incorporated into the frame hinges is shown in Figure 36.

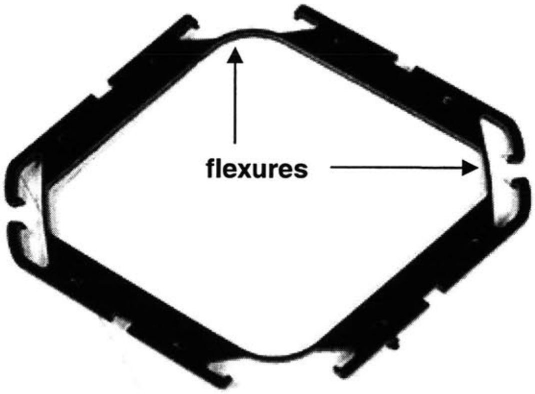

Figure 36: Diamond shaped frame using inherent stiffness of flexures for restoring force.

Experimental analyses show that the stiffness of this type of frame changes significantly with time because of the high stresses in the hinges. The graph in Figure 37 shows the blocked force of this frame as a function of time. The frame was compressed to a fixed dimension and the resulting force was measured as a function of time. After more than three days the force available from the frame had decreased over 67% and was still dropping. Such time dependent variation would make both design and performance impossible to characterize consistently.

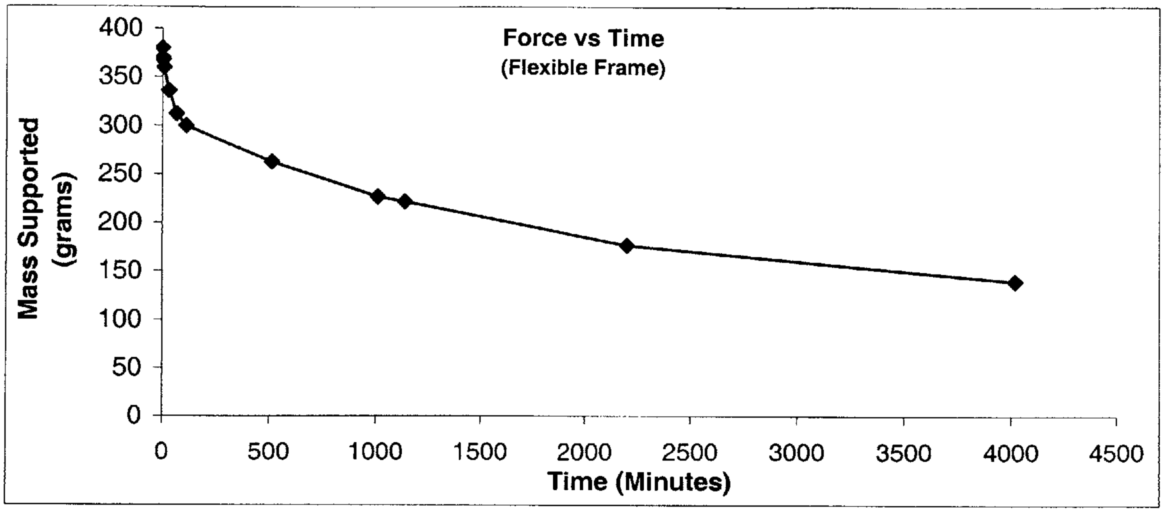

Figure 37: Decreasing blocked force due to stress relaxation.

It is difficult to design hinges for this application because of the large deformations *and* large stresses required to achieve the desired stiffness, so instead the design goal is to design a frame with minimal stiffness and minimal time dependence, and then to add the tensioning elements externally rather than incorporating them directly into the frame hinges. The hinges were therefore designed as "living hinges," which can theoretically be flexed a large number of times without failing. The objective of living hinge design is, like flexure design, to design the geometry of the hinge such that the material does not reach the yield point [57]. This problem is not as difficult because these hinges are not required to exert forces on the links, as the frame hinges shown in Figure 36 were. Therefore, they can be designed very thin, allowing large deflections without generating high stresses that would cause yielding. In general, materials with high yield strengths and low modulii, such as polyethylene and polypropylene, are optimal for this [57]. However, DEA film does not stick well to either of these materials. Fortunately, nylon 6/6 is also a reasonable candidate (*yield strength=69 MPa, modulus=3.1 GPa*), and VHB has been shown experimentally to adhere well to nylon. The resulting hinges, shown in Figure 35, are very small (so they replicate a pin joint well) and do not fail or exert large forces when subjected to large deformations.

Designing a hinge that does not yield is not the only challenge. The "soft" hinges designed here have a smaller thickness and therefore provide only a small surface area for the material to adhere to. The final design, shown in Figure 35, was designed so that the adhesion surface around the hinge was maximized in order to prevent slip.

The individual actuators can easily be stacked for increasing the stiffness and output force of the system. However, there are a few issues that should be addressed. For example, the thickness of the frame is about 40 times that of the film, this means there is unnecessary mass and volume added to the film. It would be desirable to reduce the thickness of the frame to the same magnitude as the thickness of the film. The current problem with this is that the decreased thickness of the frame make it susceptible to buckling at the hinges under the high tension in the film. Large scale production of optimized frames will enable assembling several thinner film frame modules together and then stabilizing them with an external structure that provides stability, thus enabling modular and stable assemblies capable of large forces and deformations.

3.3 Restoring force design

3.3.1 Device Selection – "Negator"

The restoring force is the component that maintains tension in the film. The potential configurations were briefly discussed in chapter 2. The design goal is to incorporate the restoring force component into the actuator in a manner that will allow maximum expansion and energy output upon actuation. The ability to specify the shape of the stiffness curve for the restoring force stiffness allows the force and displacement output of the actuator to change.

The desired shape for the restoring force is governed by the stiffness of the film in both its actuated and un-actuated states. For future development of DE actuators, determination of these stiffness profiles can be completely analytic. Currently, detailed dynamic models are being developed to fully characterize the material. However, at this point, such models are still in the primitive stage and the behavior of the film cannot be perfectly captured by analytic models.

To determine the actual stiffness profiles of the film, the frame/film assemblies are tested using a custom built testing rig. This system is capable of programmable force and displacement control. The assemblies are placed on the rig and their tensile stiffness are measured as a function of displacement at a constant strain rate between fixed displacement positions. The film/frame assembly behaves like a tension spring: it tries to close as it is pulled it open. An example of filtered data from a single stiffness profile is shown in Figure 38. Due to the high viscoelastic forces, the hysteresis loop is significant. For integration into the design model, these curves were simply averaged. This is acceptable since only low actuation speeds are necessary so viscous forces are neglected in this design method.

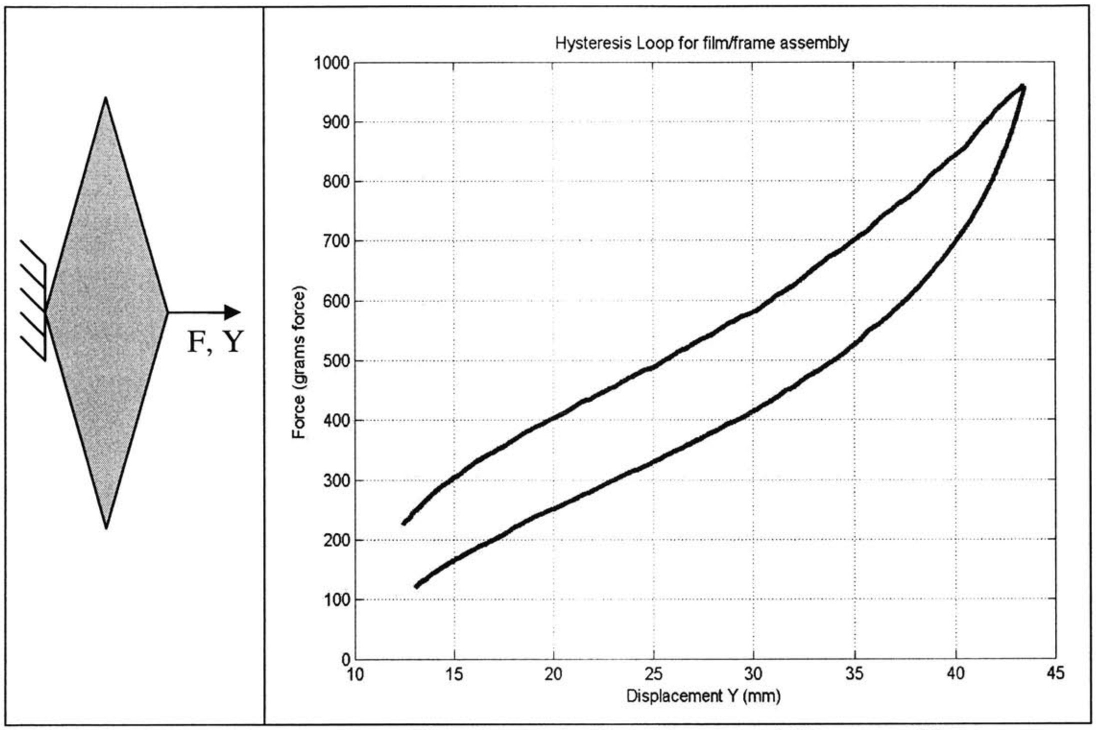

Figure 38: Experimental stiffness profile of frame and film assembly.

The test is repeated for several actuation voltages. As the voltage is increased, the entire curve shifts downwards as the planar stiffness in the film decreases. The average stiffness profiles are shown in Figure 39. The two primary curves of interest are the 0 kV (OFF) and 8 kV (ON). 8 kV is chosen as a conservative maximum voltage, though it is not uncommon to operate actuators at higher voltages if lager forces are required. Most failures occur at around 10 kV, though some actuators have been observed to survive voltages of 12-13 kV.

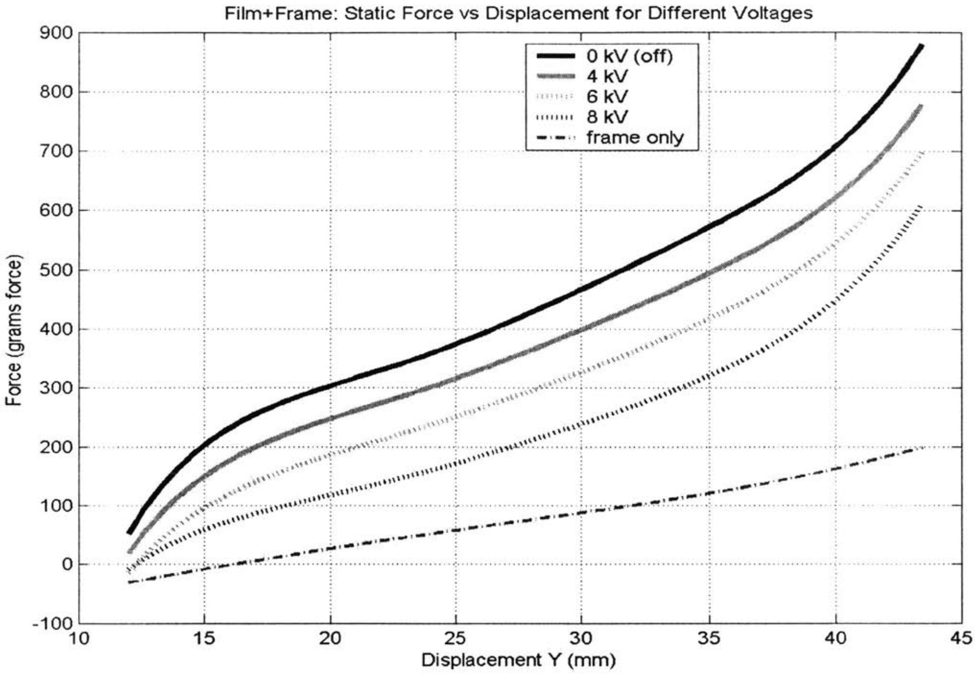

Figure 39:Experimental stiffness profiles for film/frame assembly at various voltages.

These curves represent the stiffness of the frame, film, and electrodes collectively (if only the stiffness of the film is desired, the stiffness profile of the frame can be subtracted out). In order to create an actuator capable of applying compressive forces, a preload element, equivalent to a compression spring, must be added to maintain tension, as described in the lumped sum model of Figure 4. Intuitive methods of maintaining tension would be to add a compressive force in parallel with the system or a tension spring in series. Alternatively, leaf springs could be attached about the hinges. The simplest and most common method is to fabricate the frame such that the hinges have an inherent stiffness, as in Figure 36. When the frame is in a contracted position, it tends to expand. In each of these configurations, however, the pre-load component would have a decreasing force profile. In other words, as the frame opens, the forces pushing it open would decrease (see the decreasing pre-load curve in Figure 40(a)). Elements that can provide constant force, such as a constant force spring or gravity, can allow an actuator to generate more displacement because its tendency to expand does not decrease throughout the stroke, as illustrated in Figure 40(b).

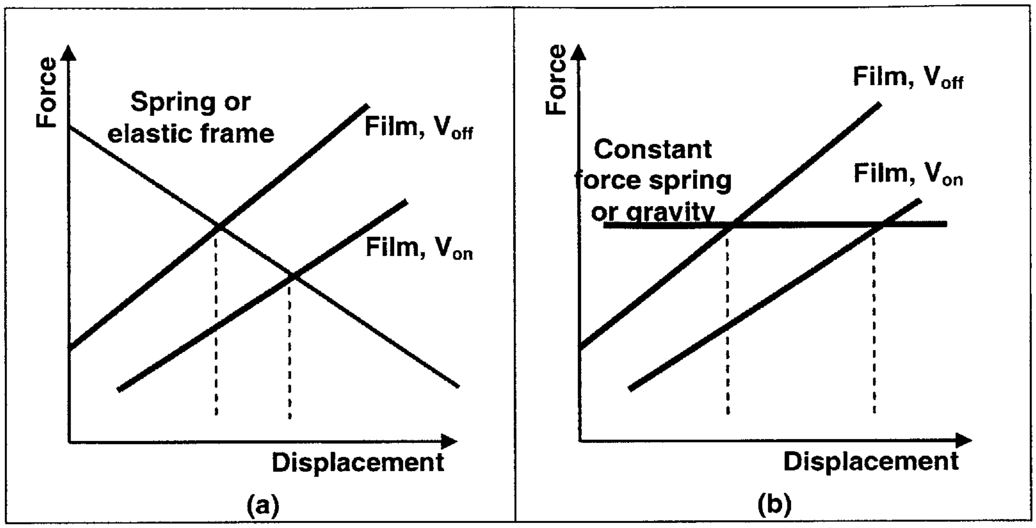

Figure 40: Stiffness profiles for two common types of pre-load elements.

In order to maximize expansion, and thus maximize the energy that can be drawn from the system, the compressive force should increase as the system expands. This is generally referred to as a negative spring constant. Adding elements with negative spring constant, such as an over the center mechanism, has been shown to increase the potential displacement of an actuator [58,55]. The behavior of a restoring force with a negative spring constant is illustrated in Figure 41. The "opening" force (pushing to right) is indicated as the difference between the negative spring constant curve and the *film ON* curve and the "closing" force (pulling to left) is indicated by the difference between the negative spring constant line and the *film OFF* curve. The displacement that can be achieved could theoretically be infinite if there is no intersection between the curves. However, this is obviously limited by both mechanical and dielectric material strength.

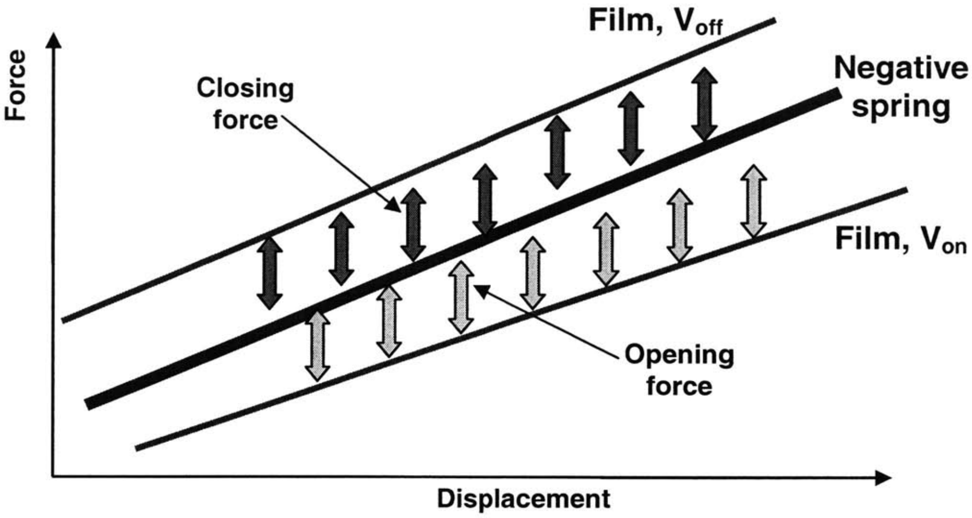

Figure 41: Stiffness profiles for pre-load element with negative spring constant. Since the slope has changed, there are no intersections between the curves and expansion is "unlimited".

One example of an element with negative spring constant is shown in Figure 42. This device is a type of snap-through mechanism developed to function in parallel with a planar actuator [55]. The device adds an external negative spring constant to enhance the strain capability of the actuator. It is relatively easy to fabricate with a water jet machine and attaches well within the system. Despite its proven effectiveness, this device has drawbacks. For example, it has a weight and size comparable to that of the actuator itself, thus it approximately doubles the weight and volume of the system. Also, the range of motion of this system is limited, and to increase it will cause the system to become significantly larger.

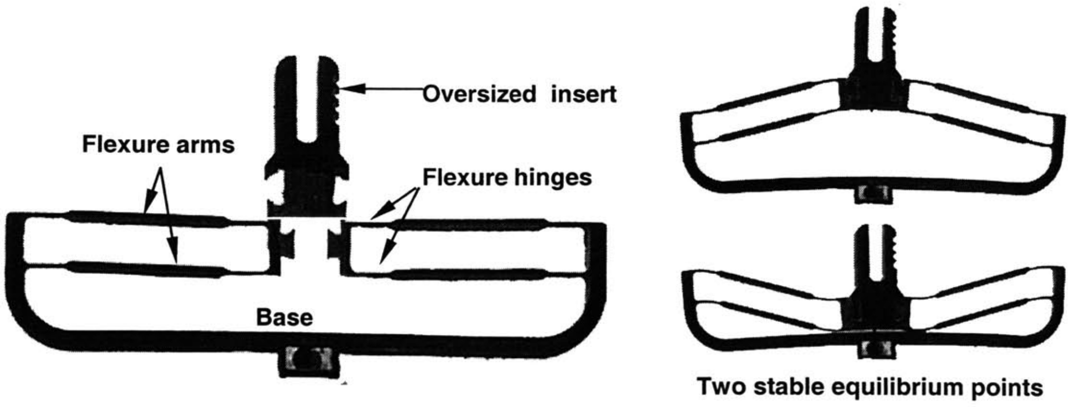

Figure 42: Previous version of device with negative spring constant [55].

Ideally, the restoring force will provide repeatable performance while adding negligible mass and volume to the system. In addition, the mechanics of the system should be easy to analyze so that it can be tuned or modified as desired. One method that has successfully met these requirements is referred to as the "negator" method. The negator provides a compressive, increasing force over a large range of motion. A schematic of the negator is shown in Figure 43.

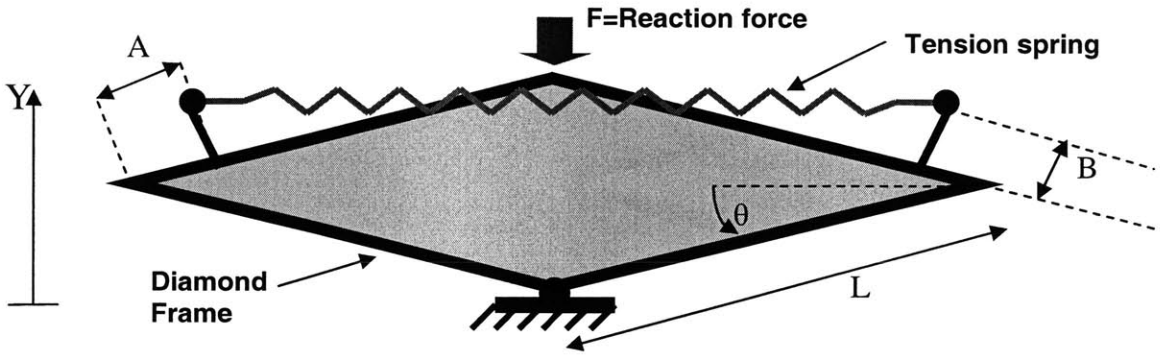

Figure 43: Schematic of negating element using elastic elements.

As the frame opens (θ, Y increases), the reaction force, F, on the frame, due to tensile forces in an elastic spring, increases through a certain range. Highly elastic elastomer bands are capable of achieving large forces with minimal hysteresis. They are nominally linear, or they can be approximated with low order polynomials. The fixture points for attaching the elements are easy to incorporate into the current frame design, and multiple fixture locations can be incorporated to allow for flexibility and experimental adjustment of the system. The system is therefore easy to model, and its stiffness profile can be adjusted to fit a desired profile. Furthermore, the mass of the elastomer band is significantly less than that of the frame/film assembly and it adds virtually no excess volume to the system.

The reaction force of the system can be determined by doing a static force analysis of the system (using the schematic in Figure 43), and is given by:

$$Force = F_s(Y) * \frac{\frac{Y}{2} - A\sin\theta + B\cos\theta}{L\cos\theta} \tag{18}$$

$$\theta = \sin^{-1}\frac{Y}{2L} \tag{19}$$

Where F_s is the tension in the spring and the geometric parameters $A, B, L,$ and Y are illustrated in Figure 43. The tension in the elastomer band can be calculated with the following set of equations:

$$F_S(y) = k*(l - l_0) \tag{20}$$

$$l = 2*\left(\left(L - A\right)\cos\theta + B\sin\theta\right) \tag{21}$$

The length of the elastomer band, l, is a function of the displacement y (and therefore θ). The spring constant, k, is a function of the dimensions of the elastomer band and its material stiffness. If the elastomer band displays a non-linear profile, which is not unusual for large strains, then k can be expressed as a strain-dependent function and can be approximated by a polynomial function.

The equation for the output force of the negator was evaluated and compared to an experimental case, as shown in Figure 44. Aside from the discrepancies at the beginning and end of the range, which is likely due to the linear approximation for the elastomer band that was used for this case, there is excellent agreement between the two curves.

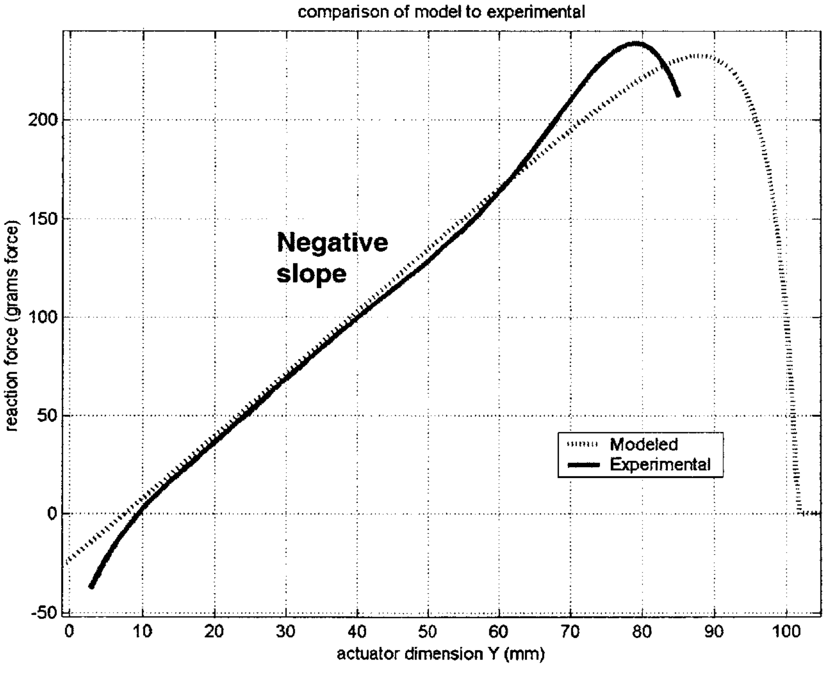

Figure 44: Model of negating element compared to experimental data.

The force profile from the negator is precisely what is desired in the restoring force. For a certain range, it has a force profile very similar to the "negative spring" line in Figure 41. The increasing force will compensate for, or "negate," the increasing tension in the film as the actuator expands, allowing for high displacements.

3.3.2 Defining Negator Parameters

Though the negator can provide the desired force profile, there is potentially an infinite number of combinations of elastomer bands and fixturing locations that can be applied to an actuator frame. Determining which combination will work best for a particular actuator design is not a trivial task.

The required force profile of the restoring component is determined based on the stiffness of the frame/film assembly. For example, if you want equal forces pushing right (upon actuation, or opening) as pulling left (turning off, or closing), then the force profile of the negating system should be the average of the OFF and ON (maximum voltage) stiffness curves, as roughly illustrated in Figure 41.

The desired profile becomes the "target" profile, and it can be expressed simply as a mathematical function in terms of the stiffness curves of the film. The only remaining task is to choose the parameters of the negator such that its output is equal to (or approximately equal to) to the target function.

Matching the output of the negator system to a target function is not trivial because of the number of parameters and non-linearity of the function. Also, if the force in the elastomer band or elastomer bands is approximated by a set of polynomials instead of a linear relationship, then substitution into the "negator" function is difficult. In order to achieve the desired restoring force, an algorithm was developed to automatically determine the necessary parameters of the system, such as the elastomer band properties (initial length, modulus, thickness) and fixturing locations (A and B as shown in Figure 44).

The method is based on a simple genetic algorithm scheme. A thorough description of genetic algorithm methods is found in [59], and it is briefly summarized here. The known parameters, such as the size of the frame (L), are substituted into the physical expression for the negator force (equation (18)). The algorithm then substitutes a set of random values into the remaining unknown quantities (such as the unknown geometry, A and B, which define the fixturing location of the elastomer band). This set of parameters make up a "parent set". Each set of parameters is coded into binary format, so that a single parent is represented by a string of ones and zeros. For example, if the design parameters are A, B, an N (number of elastomer bands), then the binary coding would look as shown in Table 3:

Table 3: Decoding of binary string into parameters values

<table>
<tr><td>1</td><td>1</td><td>1</td><td>1</td><td>0</td><td>1</td><td>0</td><td>0</td><td>1</td><td>0</td><td>0</td><td>1</td><td>1</td><td>1</td><td>0</td><td>0</td><td>0</td><td>0</td><td>1</td><td>0</td></tr>
<tr><td colspan="8">↓</td><td colspan="8">↓</td><td colspan="4">↓</td></tr>
<tr><td colspan="8">Integer = 47</td><td colspan="8">Integer = 57</td><td colspan="4">Integer = 4</td></tr>
<tr><td colspan="8">↓</td><td colspan="8">↓</td><td colspan="4">↓</td></tr>
<tr><td colspan="8">A = 9.77</td><td colspan="8">B = 2.96</td><td colspan="4">N = 4</td></tr>
</table>

Each sub-string is decoded into an integer with a range of $[0,2^n-1]$, where n is the number of bits used for coding that specific parameter. This integer is then multiplied by the appropriate scaling factor to obtain the parameters value. The value for A was constrained to be between 0 and the length, L ($L=53$ for this example), of a frame link, B was constrained to be between 0 and $L/4$, and N was the actual integer obtained form the string.

After decoding the string into the set of physical parameters, a hypothetical force-displacement curve is generated by substituting these parameters into equations (18) through (21) and evaluating it over the range of range of displacement of interest. This curve is then compared to the desired curve. The relative fitness of the potential solution is evaluated by calculating the least square difference between it and the "target" function over a given range. The "difference" and "fitness" values are given by:

$$Error = \sum_{y=\min}^{\max} \left(F_{predicted}(y) - F_{target}(y)\right)^2 \tag{22}$$

$$Fitness = \frac{1}{Error} \tag{23}$$

An example solution curve, generated from the parameters in Table 3, along with an example of a target function, is shown in Figure 45. The range over which we are interested, as well as the relative error between the curves at a series of points within this range, is indicated.

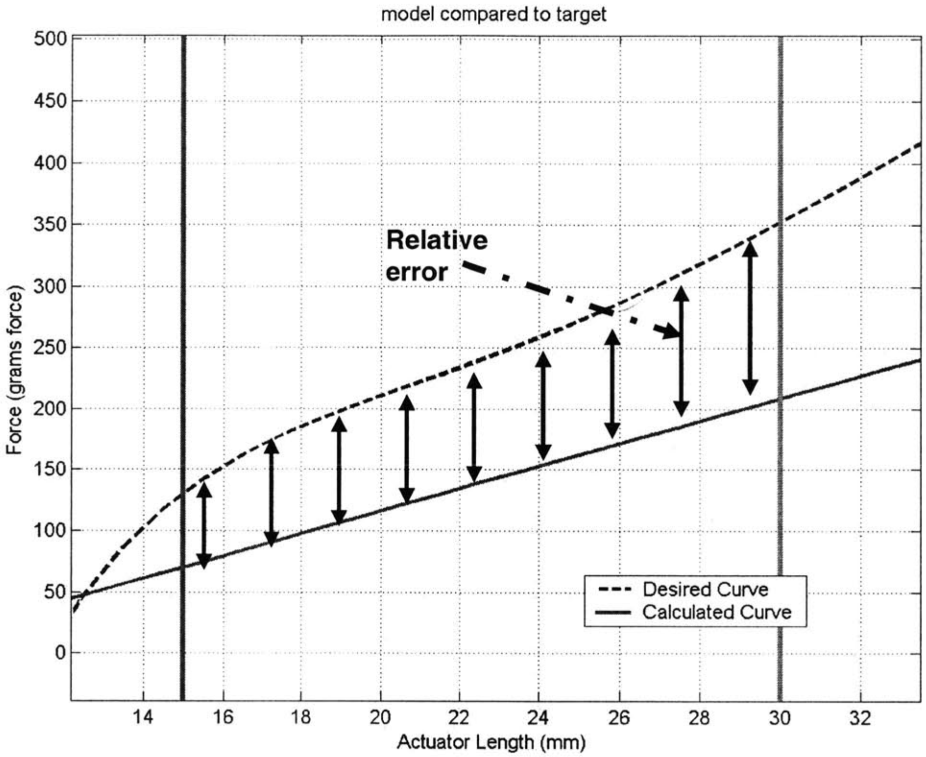

Figure 45: Example of a desired curve compared to randomly generated modeled curve. The arrows represent the relative error at a series of points.

Initially, a population of parent strings is chosen at random. After the fitness of each of these parents is determined, a population of children sets is chosen from parents sets. The children are chosen based on the relative fitness of the parents. Stronger parents will likely be carried over to the children population. After the children population is chosen, several children are chosen at random to be mated with other children so that stronger traits can be matched with other stringer traits, potentially causing better solutions to arise. During this process, called "cross-over", each string is broken into two pieces and then combined with a piece from another set. Also, certain parameters are randomly perturbed in a process called "mutation". These processes emulate actual evolutionary development in that the strongest solution are carried through and allowed to mate with other stronger solutions, i.e. "survival of the fittest." Obviously, through mutation and crossover, weaker children may be created, but it is likely that they will not be carried over to the next generation. Stronger children, on the other hand, will be formed also and these are more likely to be carried over. The percentage of children that are allowed to mate with others (as opposed to simply being copied) and the percentage of values that can be randomly mutated determines how fast or how well the solution will approach the desired solution.

Such algorithms are relatively easy to develop and can converge quickly in real time depending on the problem at hand. In this situation, fast convergence is not necessary since it is being used as a design tool, but it proves very useful for matching a given function to a desired curve that has no analytic basis (such as experimental data).

To use this algorithm for actuator design, a target function is defined in terms of the ON and OFF curves. For this example, it is desired that most of the available force be used for the opening stroke. Specifically, 75% of the force will be directed in this direction, and only 25% will be directed in the closing direction. This would represent a physical situation where the actuator has to do significant work in its opening state, such as lifting a weight, but only exert enough force in its closing state to maintain a closed position. The distribution of forces was illustrated in Figure 41. The equation for the negator force would be described by:

$$F_{negator}(Y) = \frac{1}{4}F_{film,ON}(Y) + \frac{3}{4}F_{film,OFF}(Y) \tag{24}$$

This force curve, $F_{negator}$, is shown along with the two film curves in Figure 46.

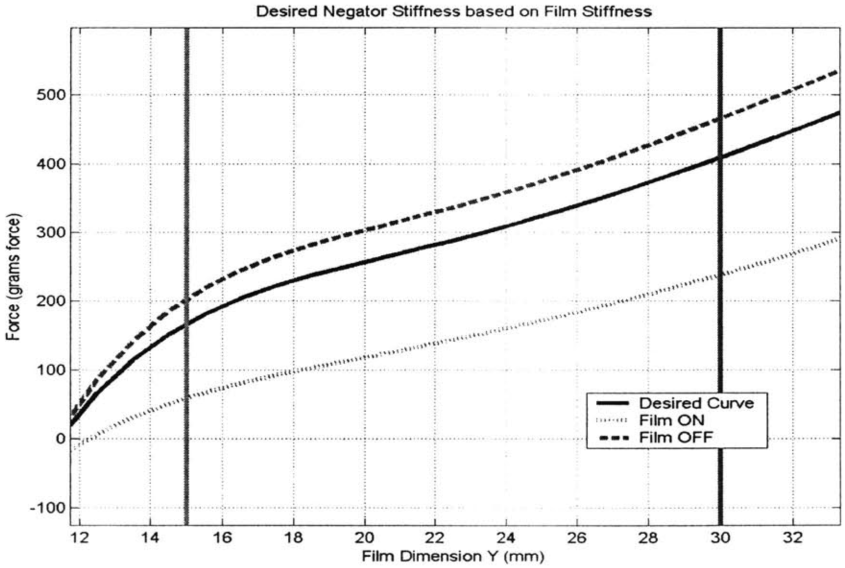

Figure 46: Experimental ON and OFF curves and their weighted average, representing the target profile for the negator.

To keep this example simple, it is assumed that only one type of elastomer band is available, with a given initial length and stiffness. The problem is therefore to determine how many of these elastomer bands should be attached to the frame, and where they should be attached, in order to obtain the correct negating force, or $F_{negator}$. The input parameters to the algorithm also include the range over which the least squares error should be minimized. For this design example, the actuator is designed to have an initial film dimension of 15 mm (OFF) and a final dimension of 30 mm (ON) (total deflection of 15 mm).

Figure 47 shows the ON and OFF curves, the target curve, and the predicted curve based on the output of the algorithm. The displacement range of interest is indicated by the vertical lines. The match is excellent over the region of interest.

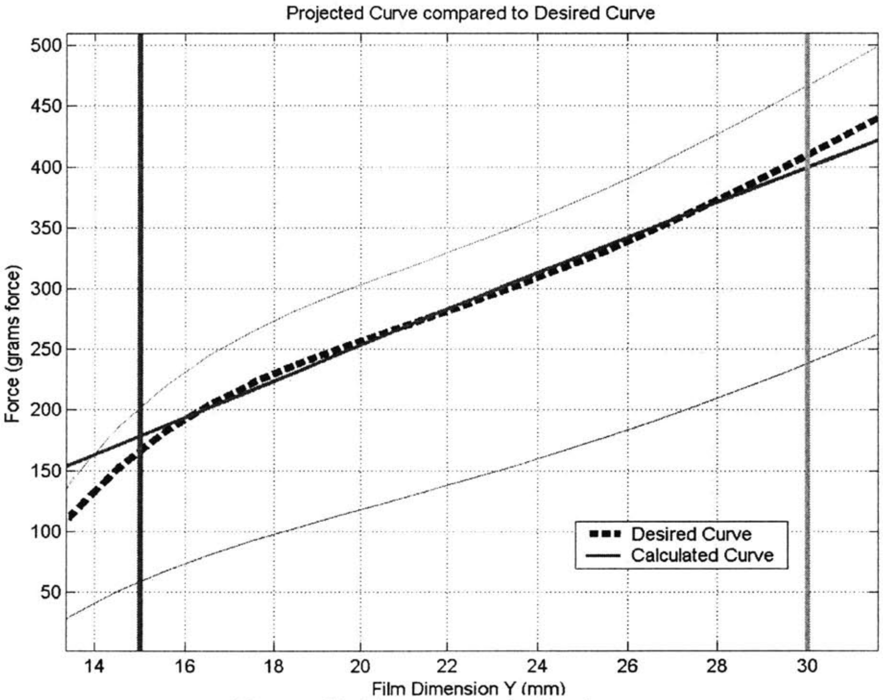

Figure 47: Target and derived curves.

Table 4 shows the parameters generated by the algorithm. If the algorithm had allowed for elastomer bands of different lengths, or more than one fixturing point, the solution set becomes larger and the solution can be formed to match the target even closer.

Table 4: Parameters generated by algorithm for designing negator element.

a (mm)	b (mm)	Number of elastic elements
7.2	3.1	6

The resulting frame design is shown in Figure 48. The position in the hole of the frame, used for fixturing the elastic element to structure, is defined by the parameters *A* and *B*. In practice, other fixturing holes may be added to the frame to allow for manually tuning the performance of the actuator after assembly. This is often necessary if the stiffness profile of the film changes over time or if a modified output force is desired after initial fabrication.

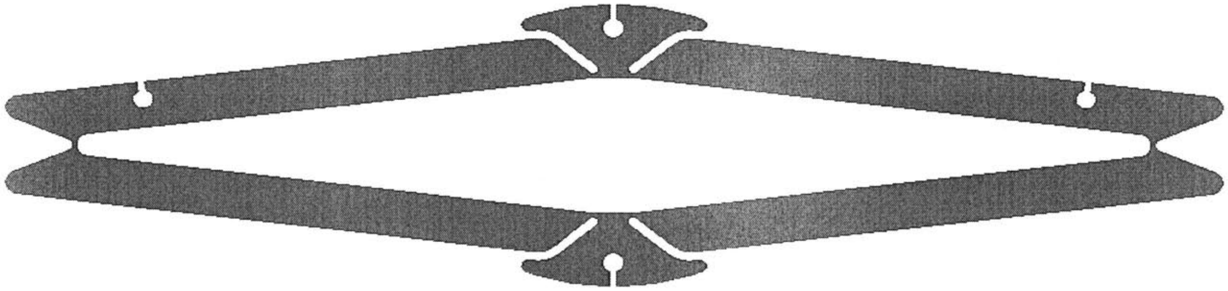

Figure 48: Frame design with fixturing holes incorporated into it.

3.4 Linear Actuator Performance

The performance of the actuator is shown in Figure 49. The actuator has an initial dimension of *Y=15 mm* and a final dimension of *Y=30 mm*, as designed using the algorithm above. The resulting material strain is therefore 100%. By modifying the negator, the actuator can be tuned to open for even larger displacements. Actuators strains of over 200% are not unreasonable.

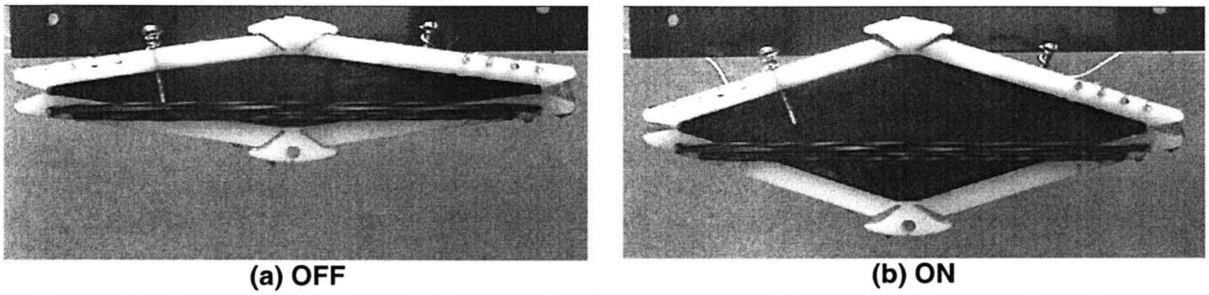

(a) OFF **(b) ON**

Figure 49: Actuator in ON and OFF state, the film has expanded from Y=15 mm to Y=30 mm.

The force-displacement of a linear actuator over 15 mm is in Figure 50. The curves shown here are curve fits of the average data points. With the addition of the negator element, the actuator can now exert negative, or compressive, forces. The upper curve is the OFF curve, when the actuator is in this state the net force within the system is positive (in tension) and the actuator will tend to close. The lower curve is the ON curve. In this state, the net forces within the system are negative and the actuator will try to open. This actuator, like the example of the preceding section, is designed to exert large forces in the opening direction and only small forces in the closing direction. The compressive force is approximately -150 grams(force) and the tensile force is approximately 50 grams(force), so the design goals are approximately met. This selection of forces would be ideal for a system where work is only done in one direction, such as flipping a switch in one direction. By changing the fixturing position and number of elastic bands, the force profile curves could have been shifted so the opening and closing forces are equal. This would be useful for an application where a payload has to be pushed or pulled with equal force.

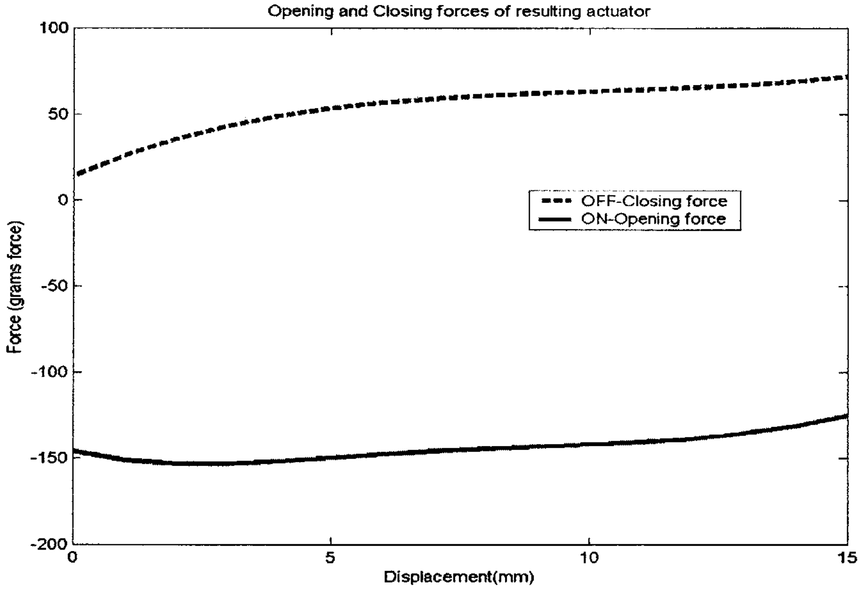

Figure 50: Force, current, and voltage profiles for actuator.

The force lines have a slight upward slope. Therefore, the negation force of the elastomer bands did not perfectly negate the stiffness of the film. In practice, this is difficult to do if there is stress relaxation in any of the major elements of the actuator (film, elastomer bands, frame hinges), but the concept is still well illustrated. A major focus of future developments of DE actuators should focus on identifying or developing materials that exhibit less creep and viscoelastic effects.

Some key characteristics of the actuator are listed in Table 5. The maximum force that it can generate, at 8 kV, is approximately 2 N. For this actuator, the available force is distributed such that it has more force on the opening stroke than on closing.

Table 5: Actuator performance characteristics

Maximum Force	~2 N
Film Strain	100%
Film Mass	0.4 g
Frame Mass	8.4 g
Negator Mass	0.8 g
Lead/electrode weight	1.0 g
Total Mass	10.6
Force:weight (total actuator)	~19
Force:weight (film only)	~500
Energy/cycle	~0.3 J

The mass of the actuator is broken down in terms of its components. 80% of its mass is due to the actuator frame. If this percentage can be decreased, perhaps by reducing the thickness of the frame, then the performance of the actuator will increase significantly, potentially approaching the force to weight ratio for the film only, which represents the ideal case. Actuators with very thin frames can be stacked in parallel to add stability and increase the output force potential.

4 MRI Applications

This chapter presents development of devices for operation within MRI systems. In chapter one, the motivation for such devices was outlined in detail. The compatibility and design guidelines were also briefly introduced.

This study is intended to show that devices constructed using binary polymer based actuators are able to function effectively within the MRI and do not degrade its imaging performance. DE actuators eliminate the need for conventional electromagnetic actuators and their associated electronics. The binary nature of the actuators eliminates the need for feedback sensors for motion control. Their construction is fundamentally inexpensive and simple. They can be constructed essentially from plastic, making their cost low enough to be disposable

The DE actuators developed in this study are fundamentally MRI compatible. The major components are polymers (nylon and acrylic). The electrodes are carbon based. The only metallic components are the brass screws used as the terminals for the electrical connections and the copper wires leading to the terminals. Both of these metals are MRI compatible, and these components need not necessarily be any certain material.

4.1 Reconfigurable Surface Coil

In order to prove compatibility and feasibility of the concept of DE actuated devices for MRI treatment, a reconfigurable imaging coil was designed. This is a relatively simple illustration, but it is a potentially useful device that effectively demonstrates the underlying concept. In MRI, individual coils are placed directly on the patient to enhance the image quality and resolution in a local region of interest. The MRI coil is a tuned resonating circuit that behaves like a radio frequency antenna to pick up the weak magnetic field emitted from Hydrogen atoms. The magnetic field induces a current in the coil. A simple illustration of the principle is shown in Figure 51(a). The physics behind the formation of the weak magnetic is related to the intense magnetic fields, and a complete explanation can be found in [1,2]. A series of such signals are collected and used to reconstruct the MR image. The conductive path of the coil is typically copper tubing, tape, wire, or an etched trace. A commercially available RF coil is shown in Figure 51(b).

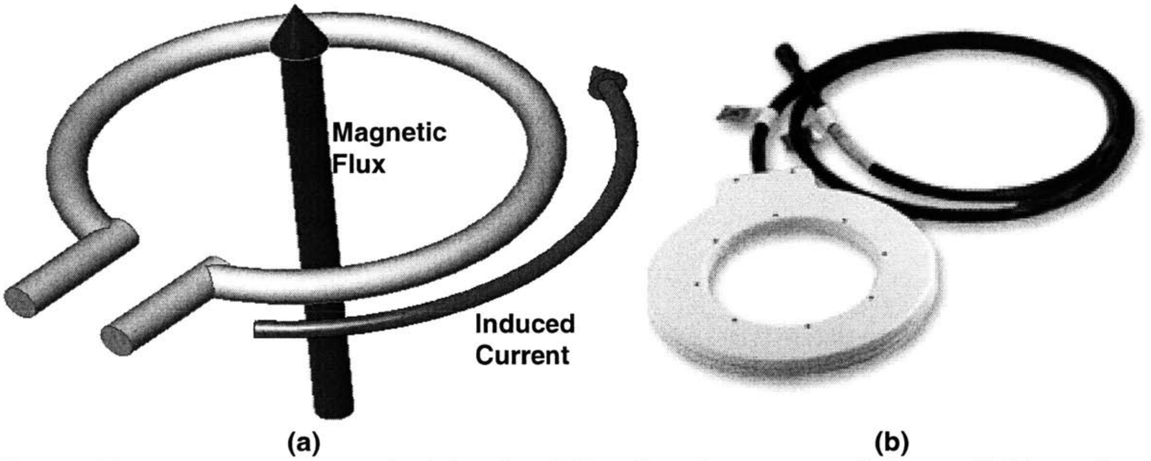

Figure 51: Basic operating principle of an RF coil and a commercially available surface coil (GE® Medical Systems).

A trade-off in image quality exists between depth of penetration of a surface imaging coil and peak signal to noise ratio (SNR) as a function of coil dimensions. To optimize image quality at a given distance from the coil, the appropriate coil dimensions should be selected. Smaller coils offer higher SNR for regions of interest close to the skin, essentially because the pick up less noise from other regions; where as larger coils are better suited for imaging of deeper regions of interest [60,61]. Changing the geometry of the coil changes the Field of View (FOV), which is the region that can be imaged with a given coil shape and location.

To improve image quality with a conventional surface coil, the coil may be moved or replaced with a coil of different dimensions, which requires that the patient be removed from the bore of the MRI scanner [62]. This is time consuming, costly, and leads to patient discomfort. Development of methods for electronically altering the FOV have shown success with phased array coil technology have shown success [61,63,64]. This process requires complex electronic design and signal processing. The simple alternative presented here is to mechanically change the shape of the coil by remote control.

4.1.1 Coil Design

Two coil design concepts were considered in this study. The first design, referred to as the Single Actuator Integrated Coil, provides a simple method for resizing an imaging coil with a minimum of moving parts. This method uses fundamental DE concepts to provide simple shape changes, as shown in Figure 52. A second design, called the Multi-Actuator Modular Coil, was also developed, which yielded more interesting results. This design employs linear DE actuators to actuate a movable frame.

The first concept involves printing a conducting trace onto a polymer film and then radially deforming the film (Figure 52). The conducting trace, which is comprised of silver grease, forms a ring that acts as an imaging coil. Carbon grease electrodes are patterned in the interior of the circular trace. Referring to Figure 52, when a voltage is applied to the carbon grease (black area), it expands, and the diameter of the Radio Frequency (RF) signal carrying coil (grey area) also changes. Note that the DE electrode is separated from the RF signal trace. The diametric change causes the field of view (FOV) of the surface coil to change.

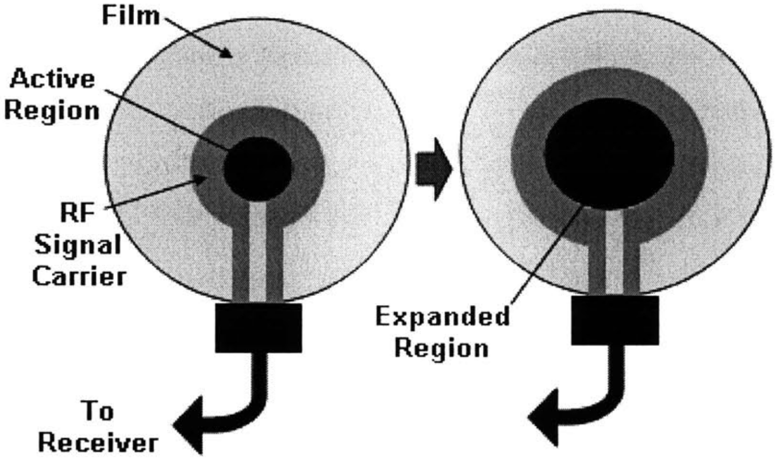

Figure 52: Single actuator, concentric coil design concept.

In the second design, an external DE actuator is used to manipulate a rectangular frame made of telescoping copper tubes (Figure 53). The copper frame forms a loop for carrying the RF signal. The construction of the frame can be designed such that several actuators can be used to modify its shape. Each linear actuator can translate, causing the frame to change size.

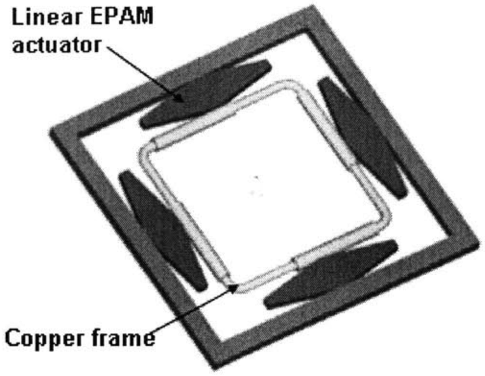

Figure 53: Multiple linear actuator design concept.

While the first design only allows for resizing of the circle about its central axis, this design allows for the coil's size, shape, and position to be changed. All four actuators can act independently. Each has two states, ON or OFF (corresponding to contracted or expanded), yielding 2^4, or 16, possible configurations for the coil, as shown in Figure 54.

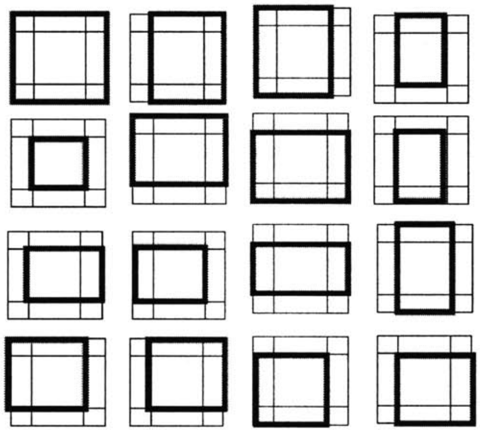

Figure 54: Possible configurations the multiple actuator concept.

For the Multi-Actuator Modular Coil Design, the FOV can be coarsely selected to provide the best imaging capability based on the depth and location of the target. In the normal configuration, when all actuators are off, the coil is at its largest and the potential imaging volume is at its maximum. If focusing on a smaller region within this volume is desired, then the appropriate configuration can be selected.

4.1.2 Results

For all MRI experiments, images were acquired of a homogeneous doped water phantom using a gradient echo imaging sequence on a 1.5T CV/i scanner (General

Electric Medical Systems, Milwaukee, WI). The custom-made power supply for the DE actuators was placed inside the MRI room.

4.1.2.1 Compatibility

The key to this application is proof of compatibility, and this was the first experiment required. Imaging was first performed with a commercially available 3" diameter surface coil (General Electric Medical Systems, Milwaukee, WI). The test was then repeated with a functional DE actuator place directly beside the imaging coil. The results show an image of a region of the phantom. Since the phantom is made of a homogenous material, the signal intensity should be uniform across the entire image. The signal drops off in intensity because signals deep within the phantom are too weak to produce large magnetic fluxes through the loop from that large a distance. Figure 55(a) shows the results for the commercial coil alone, and Figure 55(b) shows the results for the coil with an actuated DE actuator directly beside. With the DE under actuation, there was absolutely no alteration to the image results.

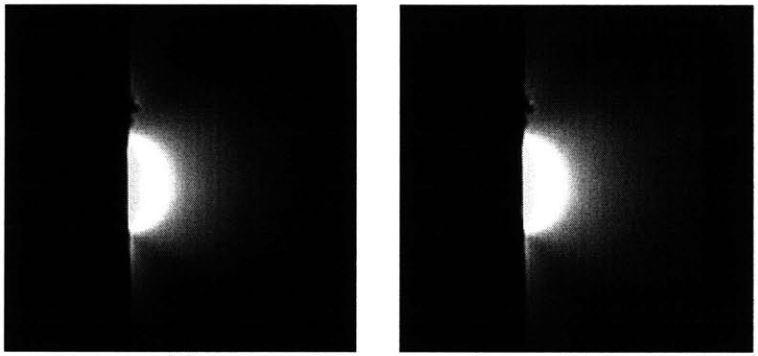
(a) (b)

Figure 55: Imaging results for conventional imaging coil alone and imaging coil with actuated DE actuator directly beside it.

These results lay the groundwork for this chapter. A device that does not degrade the MR image even when placed directly beside an imaging coil has passed the strictest of requirements. Any further development of devices employing DE actuators should also have no compatibility issues.

4.1.2.2 The Single Actuator Integrated Coil Design

Given the compatibility, the capabilities of the first design were evaluated experimentally from two points of view: the abilty to resize a coil and the available image quality. The image quality was evaluated using an imaging coil fabricated from DE materials. The silver grease was patterned onto the polymer film in a ring, simulating the design concept, but *without* resizing capability. The grease was used as the RF conductor as opposed to copper for conventional coils. The appropriate tuning circuit was attached, and images were acquired. These images were compared to those from a two turn copper wire coil of similar dimensions (see Figure 56 (c) and (d)).

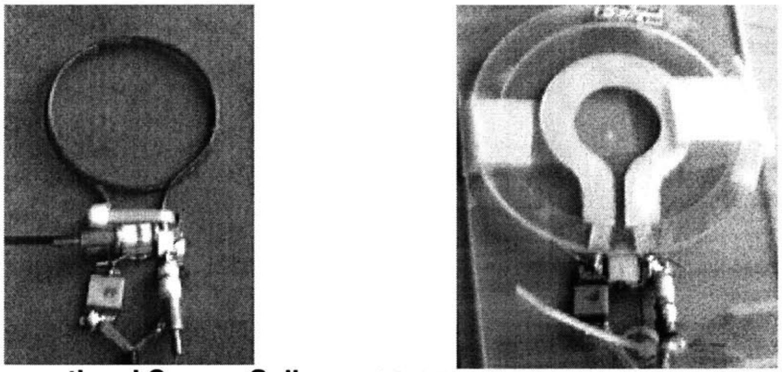

(a) Conventional Copper Coil

(b) DE coil consisting of silver grease patterned onto a deformable polymer film

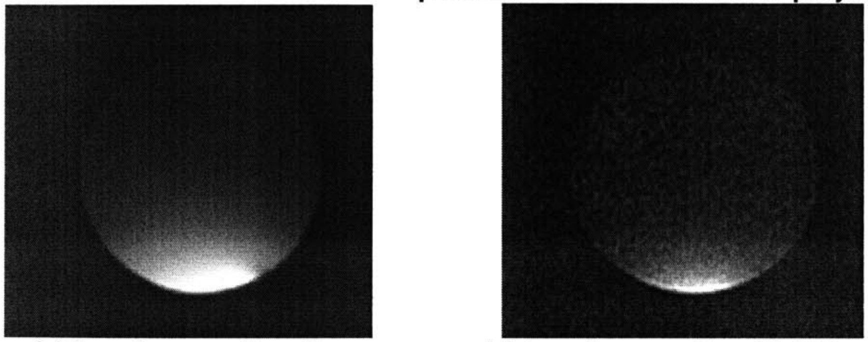

(c) Imaging results with conventional coil

(d) Imaging results with DE coil

Figure 56: Conventional copper coil and a DE based coil of similar dimensions with their acquired images.

The comparably lower SNR, which can be seen in the DE coil image (shown by the darker image) is due to the high resistance in the silver grease. The grease deposition was thickened to decrease the resistance around the loop. However, the best quality factor, which is the ratio of inductive energy to dissipated energy, was on the order of 20, as compared to 250 for the copper coil. It is suspected that the contact resistance between the silver particles, which are immersed in silicone oil, is the source of overall resistance.

Another empirically evaluated aspect of the initial design concept is its ability to change size. It is necessary to radically resize the imaging coil in order to significantly alter the FOV. The initial goal was to change the diameter of the imaging coil by a factor of 2. This requires an area expansion of 4x for a circle. However, the peak expansion for the dielectric film that can currently be achieved is approximately 2.6 times the initial area [48]. This area expansion corresponds to a maximum diameter expansion of about 1.61.

Due to these limitations in conductivity and resizability, tests for this design were not performed in which the geometry was changed. The compatibility and proof of principle tests are enough to show the fundamental feasibility of the design. Due to the limited image quality and resizability, the visible change in imaging capability would be negligible.

4.1.2.3 Multi-Actuator Modular Coil Design Concept

To test the Multi-Actuator Modular Coil, a one-dimensional version was constructed, as shown in Figure 57. The resizable frame was constructed out of telescoping copper tubes (1/8" and 5/32" outer diameter) with soldered corner joints. A linear DE actuator was attached to one side. The experimental prototype is shown in Fig. 12. The actuator used here is capable of 1.25" of displacement (approximately 200% of the active area). Two actuators were cascaded together in the final design to increase the size change.

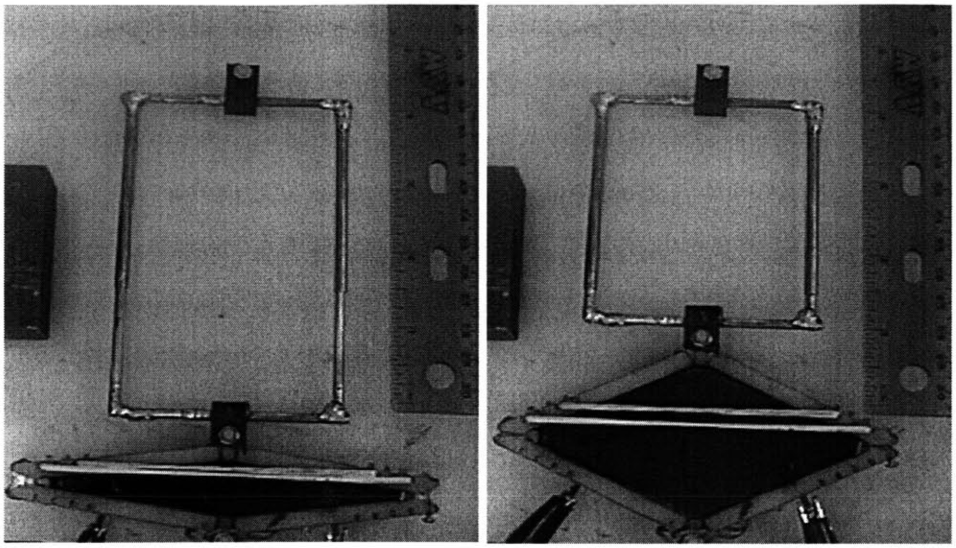

Figure 57: Resizable copper frame with the DE in both the OFF and ON position.

Next, the DE coil shown in Figure 57 was used to acquire an image in the actuator OFF (Figure 58(a)) and ON (Figure 58(b)) states. The coil was manually retuned between acquisitions to compensate for the shift in resonant frequency. Image quality was comparable to that achieved with commercial coils (Figure 58(c)). Analysis of the signal distribution for both the ON and OFF configurations confirms the expected difference in imaging capability, and the images of Figure 58 illustrate these results. Depth of penetration was, as expected, greater with the coil in the larger configuration (Figure 58(a)). This is indicated by a greater SNR deeper in the sample (bright portion covers larger area). Conversely, peak SNR was greater with the smaller diameter coil (Figure 58(b)). This region is smaller but the signal is more intense (brighter) than for the larger diameter coil. The intensity for this region is about 20% greater than for the highest intensity from the copper coil.

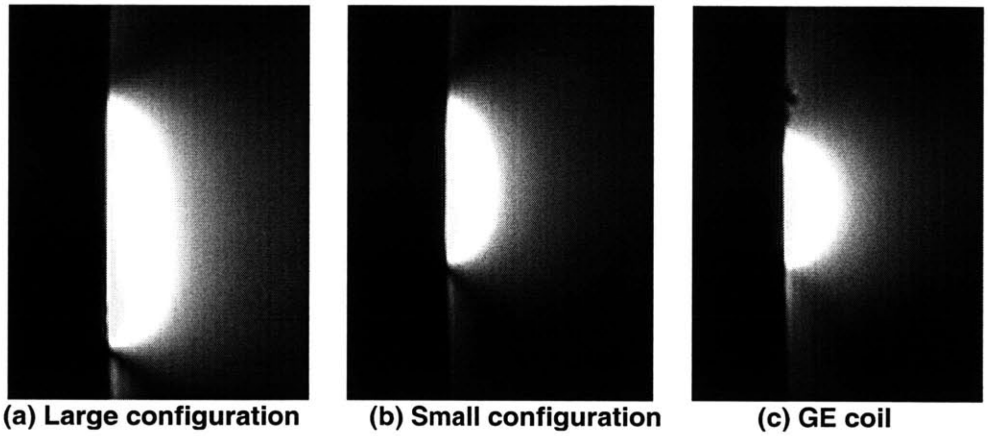
(a) Large configuration (b) Small configuration (c) GE coil

Figure 58. Imaging results for multiple actuator design. Peak intensity for small configuration is about 20% higher than that for large configuration.

4.1.3 Discussion

The results of this experiment clearly demonstrate the compatibility of DE actuators and MRI technology. DE actuators can not only function directly within imaging zones, but they can also be used to enhance the imaging capabilities. These actuators have the potential to provide robust and simple methods for adaptable imaging without complex electronic hardware.

The initial concept provides an elegant method for manipulating imaging capabilities. The limitations are due of properties of the materials available for these experiments. The development of materials with more suitable properties (lower stiffness, higher dielectric strength, higher dielectric constant) could lead to greater strain capabilities.

The second design also shows room for improvement and for future implementation. For example, only a one-dimensional version of the design was used for experimentation in this study. The two dimensional case, with multiple configurations, would provide a much more illustrative example of the concept.

Since the DE actuators used here have only two states, the resonant frequency shifts are predictable. The retuning of the coil can easily be automated. Varactor diodes in the tuning circuit can be biased to change capacitance to the appropriate level [65,66]. The same switching circuit to activate the DE actuators can be used to bias the diodes.

Besides demonstrating a specific application for DE actuator technology to MRI imaging, this study suggests a broader class of DE actuated MRI devices can be developed. The fundamental demonstration of compatibility lays the groundwork for future work. The actual demonstration of enhancing imaging capabilities shows that DE actuation can perform functional tasks within an MRI environment.

4.2 Manipulation Applications

The reconfigurable surface coil was an important device in both proving compatibility and showing actual improvement in current imaging techniques. Due to the inherent compatibility of MR technology and DE actuation, DE actuated robots have the potential of further advancing the state of the art of MR compatible surgical assist robots. In this section, simple design concepts for devices that could potentially be implemented to perform useful tasks within an MRI machine are presented.

4.2.1 Linear Positioning

One potential application for manipulation is a treatment known as Focused Ultrasound Surgery (FUS). FUS is a technique for destroying tumors by focusing ultrasound waves on it. This treatment method is a highly effective and non-invasive procedure [39]. A schematic of the technique is shown in Figure 59.

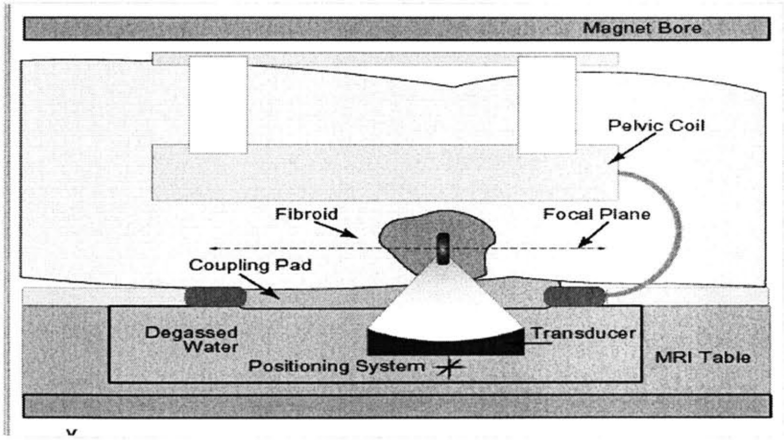

Figure 59: Schematic of Focused Ultrasound Surgery [39].

The Ultrasound Transducer is either a rigid dish with a fixed focal point or a phased array device which can electronically reposition the focal point. In either case, it is necessary to reposition the transducer itself so that it can effectively focus on a desired location. Movement of the transducer into a position where it can effectively focus on a tumor is coordinated using MRI. After initial treatment, MRI is used to reassess the position of the target and also the effectiveness of the first treatment. The patient must remain in the same position while the dish is being moved, so the transducer must be automatically and precisely moved to the required position.

4.2.1.1 Specifications

Currently, the transducer is actuated by piezo-electric motors through a transmission of brass lead screws and belt drives. The system, shown in Figure 60, is complex and expensive. The minimum requirements on the mechanical positioning system is that it can move the transducer in two axes with a resolution of 5 mm, an accuracy of 0.5 mm, and a range of 100 mm in each axis.

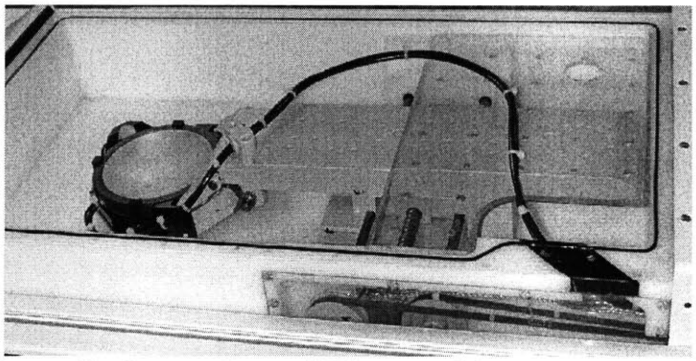

Figure 60: Current Focused Ultrasound Surgery system [39].

DE actuators present an alternative actuation method that can fulfill these requirements. Furthermore, these actuators would present a significantly less expensive and simpler substitute. With the large actuation displacement of DE actuators, the stage can be moved in large discrete steps without feedback control, making the system well suited for the MRI environment.

In order to illustrate that DE actuators could fulfill the actuation requirements of a practical MRI treatment device, a simple device that could carry out linear positioning in one axis for the required range and resolution was designed and fabricated. Further development of a complete prototype, including controlling circuitry and multiple axes, is beyond the scope of this study.

4.2.1.2 Design and Prototype

Several design concepts were considered for achieving linear positioning, from ratcheting mechanisms to digital stacks of binary actuators with geometrically increasing displacements. Ultimately, an inchworm concept was chosen as a simple and interesting method of DE powered linear motion. This method is commonly used with piezoelectric actuators for precise, microscopic positioning [67]. The concept presented here is not simply a replacement of piezoelectric actuators that requires thousands of steps, it instead uses the DE actuators for "large strain" displacements which can cover large distances with only a few cycles. The system is comprised of a guide rail, two "clutch" actuators, and one "spine" actuator. Locomotion is achieved by a coordinated set of command signals. The sequence for achieving motion to the right, as well as the basic kinematic design of the prototype built for this study, is shown in Figure 61. This approach has several advantages: the number of actuators is relatively small, no engaging motion is required for the actuator that imparts the force, and the fundamental constraint that actuators function best when only actuated for short intervals, is fulfilled.

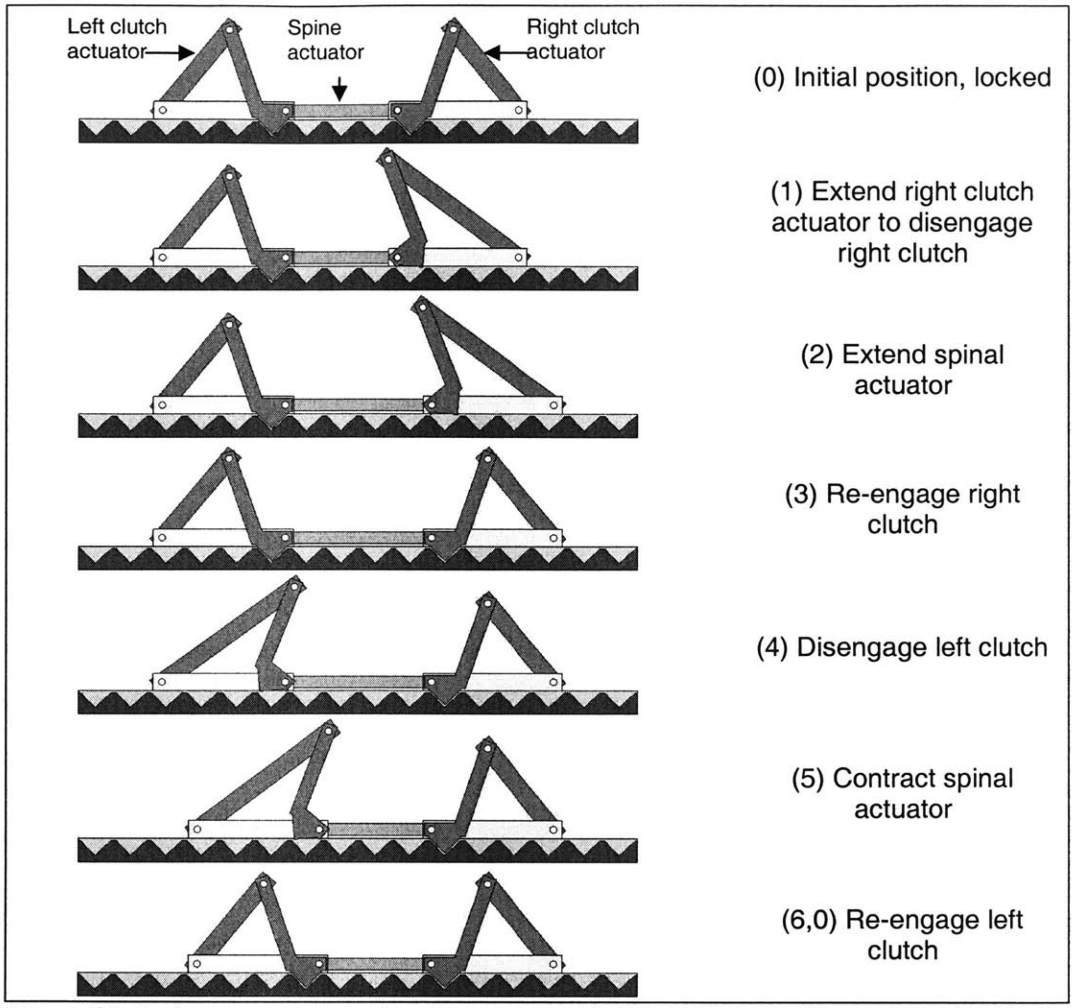

Figure 61: Inchworm concept, showing motions of clamping assembly used for this device.

An interesting approach would be to include two "spinal" actuators, in series, for faster positioning. The smaller actuator would have a displacement equal to the minimum step size as required for the application. The larger actuator would have a displacement equal to some multiple of the minimum step size, so that for large travel, the larger actuator could be used to "skip" intermediate steps and to minimize the number of cycles.

For the prototype developed here, shown in Figure 62, a single spinal actuator was used for simplicity. Whereas traditional inchworm mechanisms require sensor feedback for accurate positioning, the rail was fitted with a rack that would be engaged by the clutching actuators to ensure accurate, discrete, stepping. The actuators are those characterized in chapter 3. The device was designed so that actuators could be interchanged easily. The prototype is built entirely out of MR compatible materials

(Nylon, Delrin, Aluminum, and Brass). Using manual control of the mechanical switches for actuating each actuator, the system was moved at about 1 step per five seconds (equivalent to one mm/s).

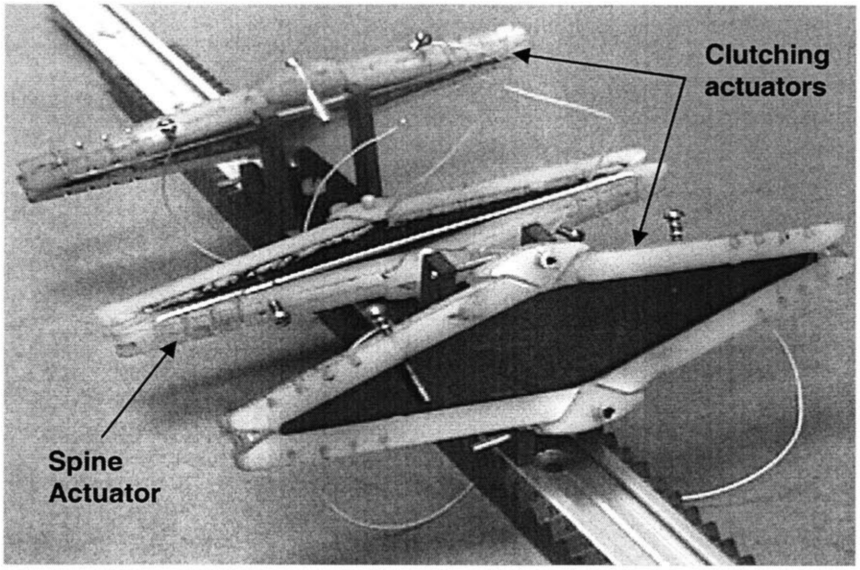

Figure 62: Illustrative prototype of inchworm concept.

Since no external payload was included in testing, the only forces present were the internal forces of the system. The rotational friction in the pivots of the clamping arms is negligible. Large forces in the clamping actuators ensure the slider is in the correct position. For example, if the spinal actuator leaves the slider a small distance (less than 1 mm) off the desired position, the downward force of the clamping actuator (when closing) can correct this offset. The clamping forces act at the center of mass of the slider, and frictional forces resulting from induced moments in the structure are minimized.

The overall mass of the sliding assembly is 51 g. The frictional coefficient of sliding mechanism is about 0.3. The spinal actuator therefore must exert a force of at least 15.3 grams(force) in both its pushing and pulling motions, easily within its performance potential (as shown in chapter 3). For this mechanism, the actuator should be designed such that its force output is equal in either opening or closing, since it must both push and pull the sliders.

This device was hand assembled from primarily two-dimensional parts manufactured on an OMAX™ water-jet machine. For practical implementation of this device, multi-layered actuators would be required to achieve forces large enough to move significant payloads. Higher precision manufacturing methods would be also be necessary improve the performance capabilities of this device, but as an illustration, this device is sufficient to show proof of concept.

4.2.2 Bi-Stable Manipulator Design

It would be useful to perform other manipulation tasks within an MRI machine. The concept for linear translation presented in the last section is interesting for specific applications that require large displacement linear positioning, but it would not be applicable for spatial manipulation within an MRI machine. There are several potential tasks that a spatial manipulator might perform, such as positioning biopsy needles, catheters, or laser pointers. The surgical assist robot designed by Chinzei et. al can perform these functions in conjunction with open MRI systems [6]. A schematic of this device is shown in Figure 63.

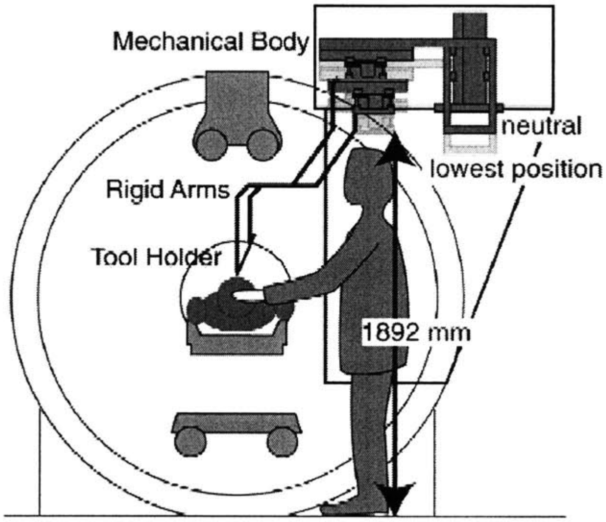

Figure 63: Surgical assist robotic system [6].

This system, like the focused ultrasound surgery device, allows for successful MRI guided procedures. However, these systems are also very specialized and complex. It would be advantageous to develop systems that are completely compatible and that could function within closed MRI machines as well, since they are more common. DE actuators can potentially be employed to replace these types of devices.

Binary robotic systems present an approach that might be especially well suited for manipulation within an MRI environment. Binary Robotics, or *Digital Mechatronics*, is a design and control paradigm that proposes the use of numerous binary actuators embedded within a mechanical structure [68,69]. The concept of binary robotics was introduced in the 1960's and 70's [70,69]. In such systems, each actuator has only two discrete states and therefore does not require feedback control. The use of sensors and complex control circuitry, which may present compatibility problems within an MRI machine, is avoided. As the number of actuators increases, the performance of the system approaches that of a continuous system, and extensive work has been done in improving and optimizing the control of such binary systems [71,72]. Despite the progress made in the fundamental analyses of these structures, practical implementation of the concept has been limited because conventional actuators, such as the DC motors, are too heavy, bulky, and expensive.

The limitations of conventional actuators led to the development of a BRAID using dielectric elastomer actuators [19,20]. The BRAID is a serial chain of stages, each actuated by three independent binary modules, that is capable of large, relatively uniform workspaces with small amounts of actuators. This work was important for providing the link between binary robotics and polymer based actuation and for establishing the foundation of dielectric elastomer actuation on which this thesis is based. Dielectric elastomer actuators have shown potential as actuators for binary robotic because they overcome most of the inherent limitations of current actuators like DC motors and pneumatic cylinders [19,20].

BRAID III, the DE actuated binary manipulator developed at MIT, represented the first step in realizing DE actuated devices for spatial manipulation [55,19,20]. This device is shown in Figure 64. Based on the compatibility of DE actuators, spatial manipulation could be achieved with such a device directly within the MRI machine. The tasks could range from simple manipulation of imaging coils to more complex positioning of needles.

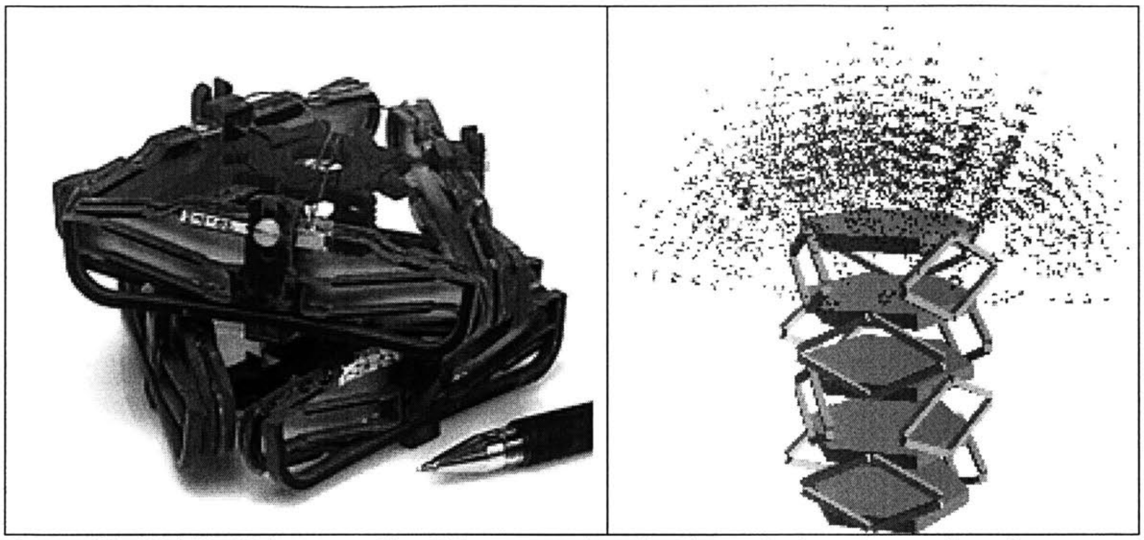

Figure 64: BRAID III (actuated by DE actuators) and a theoretical workspace based on several stages [55].

Since the development of BRAID III, there has since been significant development of DE actuators, as described in chapter 3. Using the actuators developed in this study, the same design concept could potentially be used and an enlarged workspace could be obtained. A 3-dimensional model of such a concept, in multiple configurations, is shown in Figure 65.

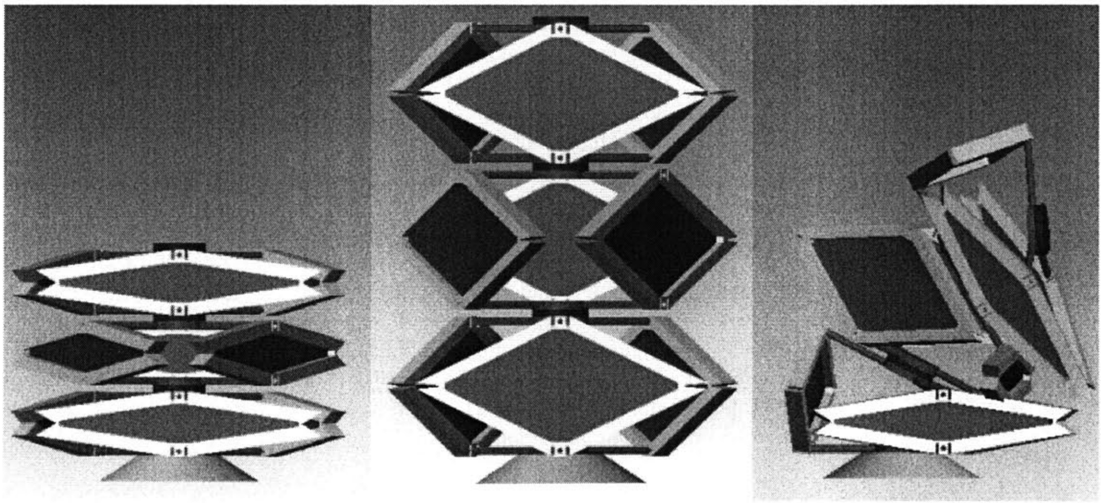

Figure 65: Theoretical design of BRAID with current actuator performance.

However, there are several features that can potentially be integrated into such a device to improve its performance. In order to maintain a specific position, constant power must be supplied to the actuator. Furthermore, the overall stiffness of the system is only stiff as any single actuator, so the external forces can easily perturb the system.

Incorporating bi-stable elements into the structure can potentially improve these characteristics. In such a concept, the actuators can be used to move the system into a new configuration, and then turned off, leaving the system in a new, stable configuration.

4.2.2.1 Bi-stable Module

For a multi-element device that requires no power to maintain a stable position, the ideal element would be very stiff in a static position and resistant to external loading, but can be re-positioned by actuators internal to the system. A bi-stable structure that can potentially fulfill these requirements is shown in Figure 66. The structure is manufactured in a horizontal configuration, and then constrained to a structure that holds it in one of two stable positions.

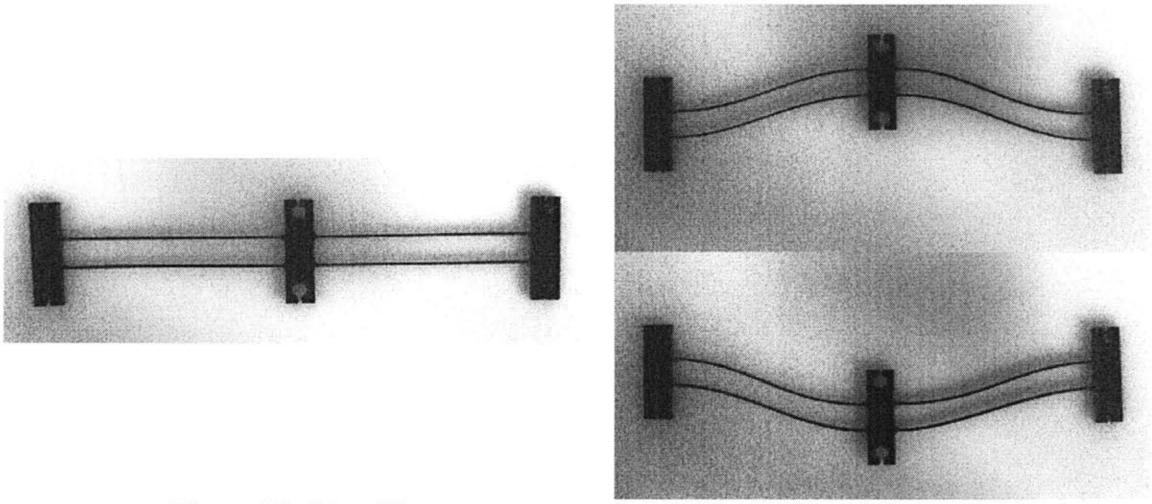

Figure 66: Bi-stable structure, water jet cut out of 1/8" thick Delrin.

This structure has several interesting characteristics. The compliance of the structure is distributed throughout the horizontal beams, so that the stress in any region is not greater than the yield strength of the material. This is an important characteristic for the structure so that it does not tend to relax in one specific position. The stress distribution is calculated with a simple FEA model, and is shown in Figure 67. No specific region has significantly higher stresses than the rest of the structure. Symmetric bi-stability is preserved.

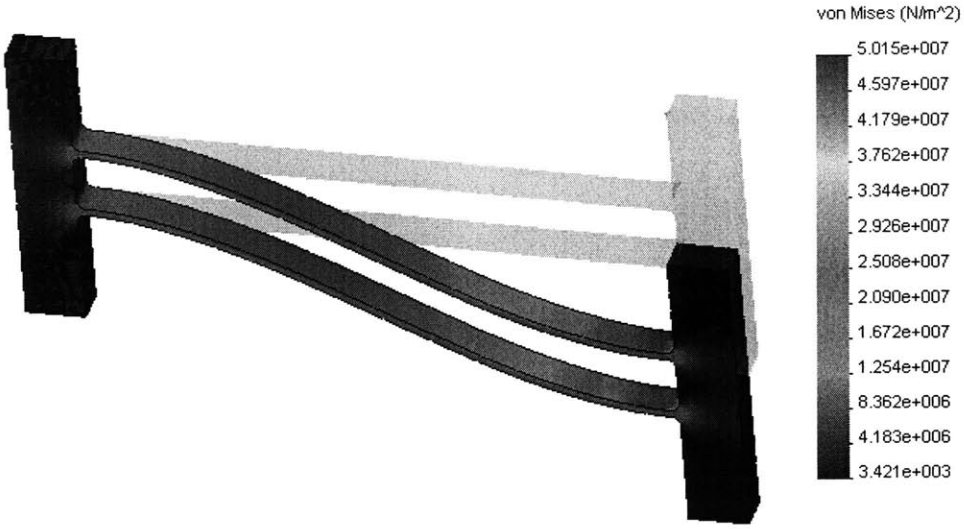

Figure 67: FEA model of one horizontal bar of bi-stable structure, showing stress distribution.

The system in moved from one stable position to the other by "snapping" it through its central location, during which the thin beams buckle. If the force is applied directly through the center of the structure, it takes a relatively large force to buckle the beams and push the structure through. Symmetry provides stability to the system. However, if the force is applied off center, the beams bend and the structure can snap through with a smaller applied force. The two different loading conditions are shown in Figure 68.

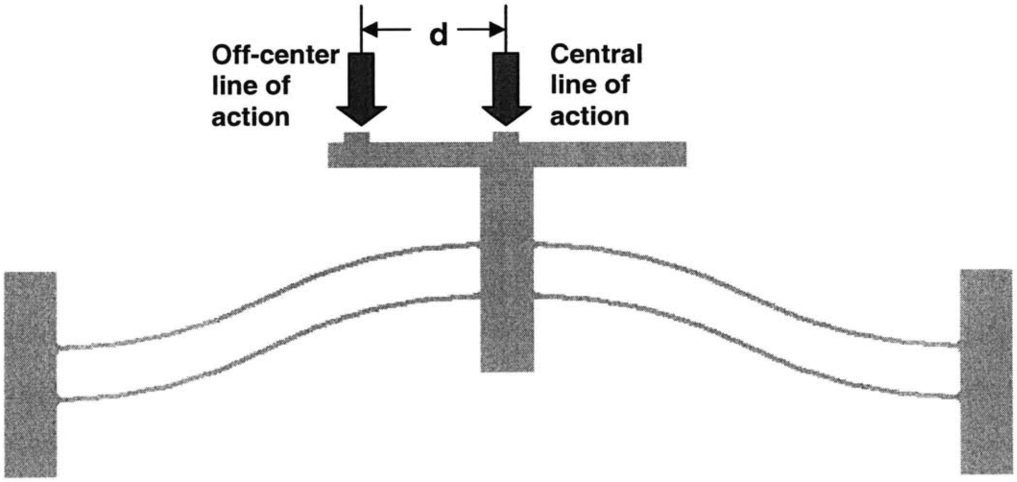

Figure 68: Alternative loading positions for bi-stable structure.

Experimental tests were done to measure the minimum force necessary to snap the structure through its central position at a series of locations. An FEA model was set up to calculate the buckling force for the same set of positions. The properties of the material (Delrin) were obtained by calibrating a simple beam bending experiment with a similar FEA model. A comparison of experimental and analytical results is shown in Table 6.

Table 6: Comparison of analytical and experimental buckling forces for various locations.

Offset distance (mm)	$d = 0$	$d = 8.9$	$d = 17.8$	$d = 20.3$
Experimental (N)	1.666	1.04	0.73	0.66
FEA (N)	1.708	1.169	0.844	0.781
% difference	2.5	12.4	15.6	18.3

The results for the central loading condition have a discrepancy of less than 3%, whereas the off-center conditions have a discrepancies ranging from 10-20%. Possible causes of the discrepancy could be inaccurate geometric modeling of the actual structure or non-linear behavior during loading (the FEA package uses linear analysis). However, the relative agreement confirms the trend.

Such a structure can effectively be utilized in a system by applying the internal (actuator) force through an off-center line of action and constructing the system so that external (loading) forces are applied through the center of the output bar. If external loads are applied directly through the center of mass of this bar, then they will exert zero torque on the beam, and it will not rotate. Thus the system can theoretically be stiffer than the actuators that power it.

In order to reposition the bi-stable structure between its two states, two antagonistic actuators are required. A simple implementation of such a configuration is shown in Figure 69. This structure constitutes a bi-stable "module." The module is capable of switching between two stable states and maintaining either stable state without constant power input. The actuators are designed such that they exert large forces while opening, but only minimal forces when closing (since they need not do any work on the closing stroke). Any point on the outer frame can be attached to a fixed location and the central bar can be attached to some type of output, so that module can function as an actuated element within a binary structure.

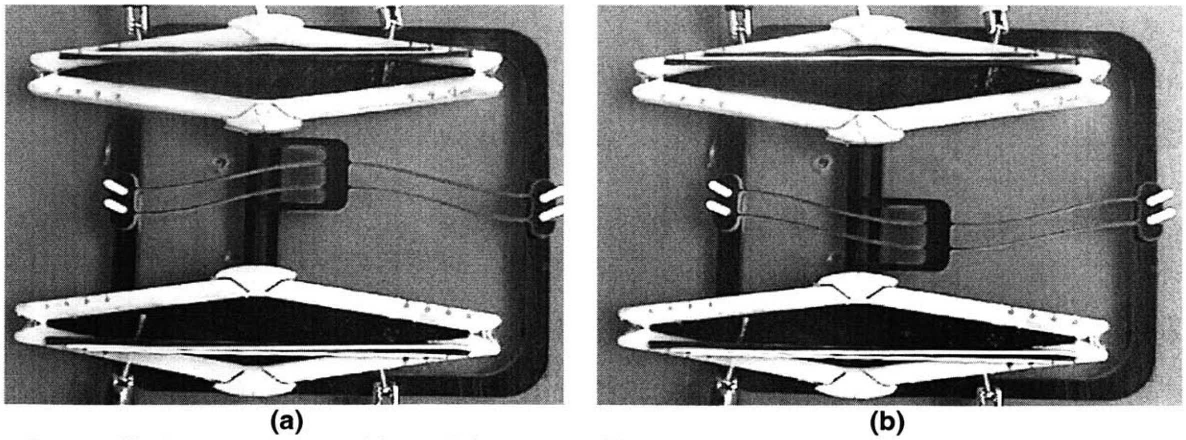
(a) (b)

Figure 69: Symmetric bi-stable module, actuated by antagonistic DE actuators. In position (a), actuate top actuator to push output down to position (b).

4.2.2.2 Binary Stage

Following the simplicity of the structure shown in Figure 69 , a simple multiple degree of freedom bi-stable stage was set-up, as shown in Figure 70. The stage is kinematically similar to the single stages of BRAIDS I,II, and III [73,19,20,74]. Three binary modules are arranged in a triangular pattern, so that if any single element changes configuration, the entire structure changes shape but no other binary element is deformed.

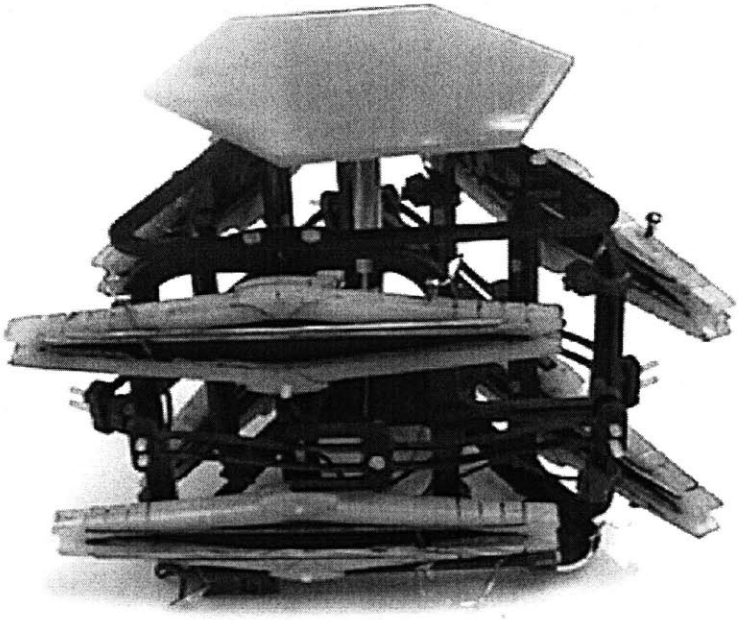

Figure 70: Bi-stable, multiple degree of freedom stage.

Since there are three binary elements, there are $2^3=8$ discrete positions. These positions are shown in Figure 71. Each of these states can be reached by actuation of a pre-defined set of actuators and then turning them off.

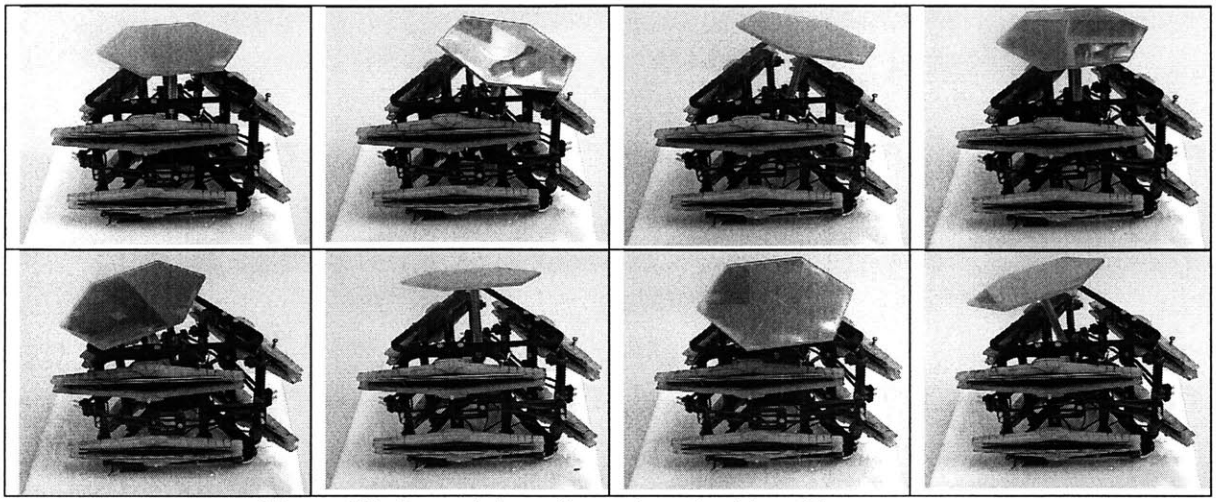

Figure 71: Potential configurations for bi-stable structure.

The design is very simple and illustrates the principle effectively. The structure is completely non-metallic and MRI compatible. Such a device could effectively be used for simple positioning functions, such as needle or laser placement, where static stability is important to functionality.

The system shown in Figure 70 has *not* been optimized for size or weight nor is it intended for any specific applicartion. For actual implementation of such a device into MRI environments, it would be important to make the structure more compact. An effective BRAID manipulator would require several stages to achieve range and resolution useful for accomplishing important tasks. The device presented here would not be conducive to such designs. However, the concept allows for alternate arrangements. For example, the actuators and bi-stable element could be layered in more than one plane to minimize the length of the structure. One such design, in its two configurations, is shown in Figure 72. The overall length of this device is 59 mm and the stroke of the element is 23 mm. The overall length of the structure in Figure 68 is 106 mm. Therefore, the strain of the second design is 39% while the strain of the first design is only 22%. Further design refinements could further reduce the weight and volume of the module, so that a manipulator structure could be designed to achieve specific performance criteria.

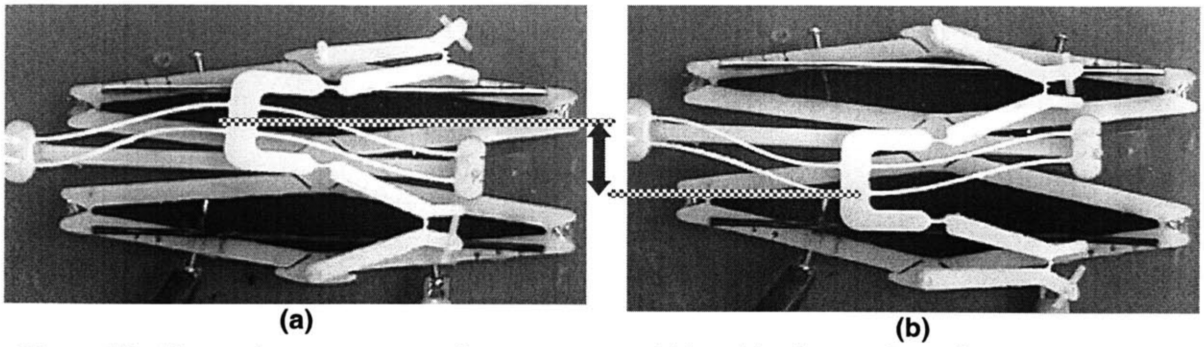

Figure 72: Alternative arrangement for actuators and bi-stable element for reduction of volume. In position (a), actuate bottom actuator to pull output down to position (b), and vise-versa.

There are several issues and performance considerations that must be considered when obtaining the ideal design, however, the purpose of this study is illustrate that systems composed of bi-stable structures and powered by DE actuators would be useful for manipulation within MRI environments. The actual development of such a device for clinical application can be undertaken when specific design criteria are established and DE actuators with the appropriate performance are available.

5 Conclusion

5.1 Summary of Results

This thesis presented the development of dielectric elastomer actuators, with an emphasis on development of MRI compatible devices and actuators. The work focused on actual construction of DE actuators for practical use. The actuators were used to manipulate devices that can potentially be used to enhance MRI treatment. This was achieved by fully characterizing the behavior of a DE actuator based on its components. The dielectric film was coupled with a plastic frame that effectively constrained it and channeled its actuation motion to the active direction. The actuator can be tuned to push and pull at desired levels.

The fundamental limits and breakdown characteristics of DE technology were explored, and key design guidelines were developed for optimizing the performance of the actuators. Several issues, such as the stress concentrations at electrode edges, have been introduced and open the door for further investigation.

The actuator module was optimized to minimize weight and volume while maximizing displacement and energy output. The displacement of the final actuators can easily exceed 100%, reaching values over 200% if desired, far greater than displacements previously attained for DE in an actuator configuration. The actuator was designed in a manner that will allow easy stacking with other actuators and integration into external devices, such as those designed for medical applications in this study.

The design and testing of the imaging coil proved both MRI-DE compatibility and the potential for enhancing imaging capabilities. The simple devices that were fabricated illustrate the potential for developing devices that go further and enhance treatment.

5.2 Future Work

A major focus of future work in this field will focus on improvements both assembly methods. Currently, actuators are being built by hand. Inconsistencies in performance can be attributed to deviations in assembly methods. Initial experimental data indicates that almost 30% of actuators failed immediately (infant mortality). These actuators failed upon initial actuation at low voltages. This ratio has dropped significantly without any fundamental changes in design or materials. Known causes are film slippage (due to "dirty frames") and accidentally punctured film. Improved tools and methods (possibly automated processes) should drastically improve actuator reliability.

A thorough investigation of the failure types is currently underway. Several potential, but not fully characterized, failure modes have been introduced in this study. For example, the electric field concentration will at least have an effect on the dielectric strength of the actuator near the edge of electrodes. However, it is not yet fully and quantitatively understood how these increased electric fields may affect mechanical stress fields. Detailed models coupling the mechanical and electrical effects can be developed now that the electrical phenomenon has been characterized. Several of the failure modes presented in this study, especially those that relate to electrical fatigue, are time dependent. The rate at which these mechanisms cause deterioration in the material is dependent on several factors, such as environmental and chemical effects, that could not be fully studies as a part of this research. Thorough experimentation and analysis is necessary to further quantify these effects. As the distinct failure modes become understood, then they can be prevented and actuator performance can improve significantly.

When reliability and consistency are increased, steps can be taken to increase the performance of the actuators. For example, current limitations in available force are not fundamental limitations to the technology. It has been established that stacking the actuators is a simple method for increasing the available force of an actuator with relatively low cost to actuator weight. The simplest method for stacking films is to build separate actuator modules and then stack them up, and then pin them together. The external restoring force (negator) can then be applied to the entire system. Currently, actuator reliability is not conducive to fabricating stacks of several DE actuators. A single failure would disable the entire system. Increasing the reliability would make this fundamentally simple procedure of stacking individual actuators very effective. Therefore, increasing the reliability of actuator reliability could make a significant effect not only in consistency, but also in other important performance characteristics, such as force

In addition to developing improved assembly techniques, material development will play a key role. The properties of the ideal film have been described. For example, to achieve large actuation pressures, an ideal film would have a high dielectric constant and a high dielectric strength. The development of thin films would reduce the required actuation voltage. Large strains are made possible by materials that can undergo large deformations and have a low elastic modulus. High efficiency is made possible by materials that have low viscous losses. Finding materials that fulfill all of these requirements is not a trivial task because many of the key parameters are fundamentally incompatible, such as dielectric strength and dielectric constant. Dedicated attempts by the material science community are required for developing improved materials.

A key development that must be achieved for practical implementation of these actuators is the development of appropriate electronic controlling devices. As envisioned, *digital mechatronic* devices implementing DE actuators would contain a large number of these actuators. Currently, there is no effective way of performing the control of many such actuators, even at a binary (ON/OFF) level. The high voltages (> 1kV) require bulky reed switches, each of which would likely have a mass greater than the actuator itself. Development of such circuitry, while not fundamentally impossible, is outside the scope of this research.

5.3 Outlook

Dielectric elastomer actuators have the potential to be implemented in a large variety of applications, not just as a mechanical actuator. The performance properties of DE actuators make them very well suited for smart material applications. For example, fabrics with variable porosity or thickness could be developed. The light weight and deployable nature of these structures make them well suited for space travel.

The likeness of DE behavior to that of natural muscles has been explored, and these material could potentially be incorporated in prosthetic devices or control architectures that directly mimic biological control schemes [75].

The success of the actuators in this research and the development of sound design guidelines, combined with the growing interest and development of DE throughout the world, justifies the belief that DEA may soon be implemented into practical applications ranging from medicine to space.

References

[1] Young, S.W., "Nuclear Magnetic Resonance Imaging: Basic Principles," Raven Press, New York, 1984.

[2] Thomas, S.R., Dixon, R.L., "NMR in Medicine: The Instrumentation and Clinical Applications," American Institute of Physics, New York, 1986.

[3] Chinzei, K.,Hata, N., Jolesz, F., Kikinis, R., "MR Compatible Surgical Assist Robot: System Integration and Preliminary Feasibility Study," Proc. MICCAI 2000, Lecture Notes in Computer Science, Vol. 1935, pp. 921-30, 2000.

[4] Pfleiderer, S., et al., "A manipulator system for 14-gauge large core breast biopsies inside a high-field whole-body MR scanner." Journal of Magnetic Resonance Imaging, vol. 17, pp. 493-8, April, 2003.

[5] Koseki, Washio, Chinzei, Iseki, "Endoscope Manipulator for Trans-nasal Neurosurgery, Optimized for and Compatible to Vertical Field Open MRI," Proc. MICCAI 2002, Lecture Notes on Computer Science, Vol. 2488, 2002.

[6] Chinzei, K., Kikinis, R., Jolesz, F.A., "MR Compatibility of Mechatronic Devices: Design Criteria," Proc. MICCAI '99, Lecture Notes in Computer Science, Vol. 1679, Springer-Verlag, pp. 1020-31, 1999.

[7] Bar-Cohen, Y., "Electroactive Polymer (EAP) Actuators as Artificial Muscles: Reality, Potential, and Challenges," SPIE Press, Washington, D.C., 2001.

[8] Egawa, S., Higuchi, T., "Multi-Layered Electrostatic Film Actuator," Proceedings of IEEE Micro Electro Mechanical Systems, California, 1990.

[9] Pelrine R., Kornbluh R., Joseph J., Chiba S., "Electrostriction of Polymer Films for Microactuators," Proc. IEEE Tenth Annual International Workshop on Micro Electro mechanical Systems, Nagoya, Japan, pp. 238-243, 1997.

[10] Kofod G., Kornbluh R., Pelrine R., Sommer-Larsen P., "Actuation response of polyacrylate dielectric elastomers," Proceedings of SPIE, Vol. 4329, 2001.

[11] Sommer-Larsen P., Hooker J., Kofod G., West K., Benslimane M., Gravesen P., "Response of dielectric elastomer actuators," Proceedings of SPIE Vol. 4329, 2001.

[12] Cho S., Ryew S., Jeon J., Kim H., Nam J., Choi H., Tanie K., "Electrostrictive Polymer Actuator Using Elastic Restoring Force," Proceedings of 1st Intelligent Microsystem Symposium, pp. 1963-1968, 2001

[13] Jeon J., Park K. C., An S. Y., Nam J. D., Choi H., Kim H., "Electrostrictive polymer actuators and their control systems," Proceedings of SPIE Vol. 4329, 2001.

[14] Lacour, S.P., Pelrine, R., Wagner, S., Prahlad, H., "Photoconductive high-voltage switches of thin-film amorphous silicone for EAP actuators," Proceedings of SPIE, Vol. 5051, 2003.

[15] Goulborne, N., Frecker, M., Mockensturm, E., Snyder, A., "Modeling of a Dielectric Diaphragm for a Prosthetic Blood Pump," Proceedings of SPIE, Vol. 5051, 2003.

[16] Szabo, J.P., et al, "Elastomeric Composites with high dielectric constant for use in Maxwell Stress Actuators," Proceedings of SPIE, Vol. 5051, 2003.

[17] Anderson V., Horn R., "Tensor Arm Manipulator Design," ASME, 67-DE-57, 1967.

[18] Roth B., Rastegar J., Scheinman V., "On the Design of Computer Controlled Manipulators," First CISM-IFTMM Symposium on Theory and Practice of Robots and Manipulators, pp. 93-113, 1973.

[19] Wingert, A., Lichter, M., Dubowsky, S., Hafez, M. "Hyper-Redundant Robot Manipulators Actuated by Optimized Binary Dielectric Polymers." Proceedings of SPIE, Vol. 4695, 2002

[20] Wingert, A., Lichter, M.D., and Dubowsky, S. "On the Kinematics of Parallel Mechanisms with Bi-Stable Polymer Actuators." Proceedings of the 8th International Symposium on Advances in Robot Kinematics, Barcelona, Spain, June 2002.

[21] Kornbluh R ., Pelrine R., Eckerle, J., Joseph J, "Electrostrictive Polymer Artificial Muscle Actuators," Proceedings of the 1998 IEEE International Conference on Robotics and Automation, Leuven, Belgium, May, 1998.

[22] Waram T., "Actuator Design Using Shape Memory Alloys," 2nd Edition, T. C. Waram Publisher, Hamilton Ontario, Canada, 1993.

[23] Pelrine R., Sommer-Larsen P., Kornbluh R., Heydt R., Kofod G., Pei Q., Gravesen P., "Applications of Dielectric Elastomer Actuators," Proceedings of SPIE, Vol. 4329, March 2001.

[24] Kota S., Hetrick J., Li Z., Saggere L., "Tailoring Unconventional Actuators with Compliant Transmissions: Design Methods and Applications," IEEE/ASME Transactions on Mechatronics, Vol. 4, No. 4, pp. 396-408, December 1999.

[25] Baughman R. H., "Conducing polymer artificial muscles," Synthetic Metals, 78, pp. 339-353, 1995.

[26] Heydt R., Kornbluh R., Pelrine R., Mason V., "Design and Performance of an Electrostrictive-Polymer-Film Acoustic Actuator," J. Sound and Vibration, Vol. 215, No. 2, pp. 297-311, 1998.

[27] Eckerle J., Stanford S., Marlow J., Marlow J., Schmidt R., Oh S., Low T., Shastri S., "A Biologically Inspired Hexapedal Robot Using Field-Effect Electroactive Elastomer Artificial Muscles," Proceedings of SPIE, Vol. 4329, 2001.

[28] Tews, A. M., Pope, K. L., Snyder, A.J., "Pressure-Volume Characteristics of Dielectric Elastomer Diaphragms," Proceedings of SPIE, Vol. 5051, 2003.

[29] Kornbluh, R.D. et al, "Shape Control of large lightweight mirrors with dielectric elastomer actuation", Proceedings of SPIE, Vol. 5051, 2003.

[30] Bolzmacher, C., Hafez, M., Khouda, M. B., Bernardoni, P., Dubowsky, S., "Polymer Based Actuators for Virtual reality Devices," Proceedings of SPIE, San Diego, 2004.

[31] Choi, H. R., et al, "Multiple Degree-of-Freedom Digital Soft Actuator for Robotic Applications," Proceedings of SPIE, Vol. 5051, 2003.

[32] Youn, J.W., Jeon, J.W., Choi, H., Kim, H., Nam, J.D., "Control of an electrostrictive polymer actuator with no sensor," Proceedings of SPIE, Vol. 5051, 2003.

[33] Shellock, F.G., "Pocket Guide to MR Procedures and Metallic Objects: Update 1998," Lippincott-Raven Publishers, Philadelpia, 1998.

[34] Schenk, J.F., "The role of magnetic susceptibility in magnetic resonance imaging: Magnetic field compatibility of the first and second kinds," Medical Physics, Vol. 23, 1996.

[35] A Primer on Medical Device Interactions with Magnetic Resonance Imaging Systems. U. S. Department of Health and Human Services, Food and Drug Administration,Center for Devices and Radiologicial Health. Magnetic ResonanceWorking Group Draftreleased for comment on: February 7, 1997. http://www.fda.gov/cdrh/ode/primerf6.html.

[36] K. Chinzei, R. Kikinis, F. Jolesz, "MR Compatibility of Mechatronic Devices: Design Criteria," Proc. MICCAI'99, Lecture Notes in Comp. Sci., vol. 1679, pp. 1020-31, 1999.

[37] Chinzei, K., Hata, N., Jolesz, F.A., Kikinis, R., "Surgical Assist Robot for the Active Navigation in the Intraoperative MRI: Hardware Design Issues," Intelligent Robots and Systems, 2000, Volume: 1, pp. 727 -732, 2000.

[38] Masamune, K., et al, "Development of an MRI compatible Needle insertion manipulator for stereotactic Neurosurgery," Journal of Image Guided Surgery, Vol. 1, 1995.

[39] Hynynen, K., et al, "MR Imaging-guided Focused Ultrasound Surgery of Fibroadenomas in the Breast, a Feasibility Study," Radiology, Vol. 219, 2001.

[40] Meijer K., Rosenthal M., Full R., "Muscle-like actuators? A comparison between three electroactive polymers," Proceedings of SPIE, Vol. 4329, 2001

[41] Kornbluh R ., Pelrine R., Joseph J, "Elastomeric Dielectric Artificial Muscle Actuators for Small Robots," Proceedings of the Materials Research Society Symposium, vol. 600, pp. 119-130, 2000.

[42] Pelrine R., Kornbluh R., Joseph J., "Electrostriction of Polymer Dielectrics with Compliant Electrodes as a Means of Actuations," Sensor and Actuators A: Physical, 64, pp. 77-85, 1998.

[43] Kofod G., "Dielectric elastomer actuators," Ph.D. Thesis, Department of Chemistry, Technical University of Denmark, September 2001.

[44] Bicerano, J., "Prediction of Ploymer Properties: Third Edition, Revised and Expanded," Marcel Dekker, New York, 2002.

[45] Seanor, D.A., "Electrical Properties of Polymers," Polymer Science, American Elsevier Publishing Co, New York, 1972.

[46] Mason, J.H., "Dielectric Breakdown in Solid Insulation," Progress in Dielectrics I, Heywood and Company Ltd., 1959.

[47] Pelrine R., Kornbluh R., Pei Q., Joseph J., "High Speed Electrically Actuated Elastomers with Strain Greater Than 100%," Science, Vol. 287, pp. 836-839, 2000.

[48] Plante, J.S., Vogan, J.D., Sujan, V., Dubowsky, S., Mangalgiri, V., Korb, S, "Investigation of the maximum strain and failure modes of dielectric elastomer actuators," In preparation..

[49] Wolfe, S.V., "Polymers in telecommunications and power transmission," Engineering Polymers, Chapman and Hall, New York, 1990.

[50] Griffiths, D.J., "Introduction to Electrodynamics," Prentice Hall, Upper Saddler River, NJ, 1999.

[51] Castro, M.A., Sosa, H.A., "Electro-elastic effects induced by surface electrodes attached to anisotropic dielectrics," Mechanics and Materials for Electronic Packaging, Vol.3, 1994.

[52] Fishbane, P., Gasiorowicz, S., Thornton, S., "Physics: For Scientists and Engineers" Volume 2, Prentice Hall, New Jersey, 1996.

[53] Juvinall, R.C., Marshek, K.M., "Fundamentals of Machine Component Design," John Wiley & Sons, New York, 1991.

[54] Whitehead, S., "Dielectric Breakdown of Solids," Oxford University Press, London, 1951.

[55] Wingert A., "Development of a Polymer-Actuated Binary Manipulator", M.S. Thesis, Department of Mechanical Engineering, Massachusetts Institute of Technology, Cambridge, MA, 2002.

[56] OMAX™ Product Information, www.omax.com.

[57] Tres, P.J., "Designing Plastic Parts for Assembly," Hanser Gardner Publications, 4th edition, April, 2000.

[58] Pelrine R., Kornbluh R., Joseph J., Heydt R., Pei Q., Chiba S., "High-field deformation of elastomeric dielectrics for actuators," Materials Science and Engineering, Vol. 11, 2000.

[59] Goldberg, D., "Genetic Algorithms in Search, Optimization, and Machine Learning," Addison-Wesley, Reading, MA, 1989.

[60] Axel, L., Hayes, C., "Surface coil magnetic resonance imaging," Arch. Int. Physiol. Biochem., vol. 93, pp. 11-18, December 1985.

[61] Roemer P., Edelstein, W., Hayes, C., Souza, S., Mueller, O., "The NMR phased array," Magnetic Resonance in Medicine, vol 16, pp. 192–225, 1990.

[62] White, C., Konyer, N., Kucharczyk, W.,Bernstein, M., Bronskill, M., "Improved coil designs for neurosurgical guidance with open-concept MR systems," Proceedings of the International Society of Magnetic Resonance in Medicine, Denver, CO, 2000.

[63] Leussler, C., Mazurkewitz, P., Bornert, P., "Intrinsic Hybrid Surface Coil Array for Improved SNR in Cardiac MRI," Proceedings of the International Society of Magnetic Resonance in Medicine, Vol. 10, 2002.

[64] Artemov, D., et al, "Switchable Multicoil Array for MR Micro-Imaging of Breast Lesions," Magnetic Resonance in Medicine, Vol. 41, 1999.

[65] E. Boskamp, "Improved surface coil imaging in MR: decoupling of the excitation and receiver coils," Radiology, Vol. 157, pp.449-452, Nov. 1985.

[66] R. Venook, G. Gold, B. Hu, G Scott, "Autotuning Electronics for Varactor Tuned, Flexible Interventional RF Coils," Proceedigns of the International Socitey of Magnetic Resononance Imagin iin Medicine, Vol. 10, 2002.

[67] Slocum, A.H., "Precision Machine Design," Prentice-Hall, Dearborn, MI, 1992.

[68] Anderson V., Horn R., "Tensor Arm Manipulator Design," ASME, 67-DE-57, 1967.

[69] Roth B., Rastegar J., Scheinman V., "On the Design of Computer Controlled Manipulators," First CISM-IFTMM Symposium on Theory and Practice of Robots and Manipulators, pp. 93-113, 1973.

[70] Anderson V., Horn R., "Tensor Arm Manipulator Design," ASME, 67-DE-57, 1967.

[71] Chirikjian G., Ebert-Upoff I., "Discretely Actuated Manipulator Workspace Generation Using Numerical Convolution on The Euclidean Group," Proceedings of the IEEE International Conference on Robotics and Automation, pp. 3063-3069, 1994.

[72] Lees D., Chirikjian G., "A Combinatorial Approach to Trajectory Planning for Binary Manipulators," Proc. of the IEEE International Conference on Robotics and Automation, Minneapolis, MN, 1996.

[73] Lichter, M.D., Sujan, V.A., and Dubowsky, S. "Computational Issues in the Planning and Kinematics of Binary Robots." Proceedings of the 2002 IEEE International Conference on Robotics and Automation (ICRA 02), Washington, DC, May 2002.

[74] Hafez, M., Lichter, M., and Dubowsky, S. "Optimized Binary Modular Reconfigurable Robotic Devices." Proceedings of the 2002 IEEE International Conference on Robotics and Automation (ICRA 02), Washington, DC, May 2002.

[75] Lorussi, F., "Recruited dielectric elastomer motor units as pseudomuscolar actuator," Proceedings of SPIE, Vol. 5051 2003.